



universität
wien

DIPLOMARBEIT

Titel der Diplomarbeit

„Abundance analysis of the Gamma Doradus –
Delta Scuti hybrid HD 8801“

Verfasser

Richard NEUTEUFEL

angestrebter akademischer Grad

Magister der Naturwissenschaften (Mag. rer.nat.)

Wien, 2009

Studienkennzahl lt. Studienblatt: A 413

Studienrichtung lt. Studienblatt: Astronomie

Betreuerin / Betreuer: Univ. Prof. Dr. Dipl.-Ing. Werner Wolfgang Weiss

1.	Introduction	1
1.1.	HD 8801.....	1
1.2.	Gamma Doradus stars.....	4
1.2.1.	Background.....	4
1.2.2.	Theory.....	6
1.3.	Delta Scuti stars.....	7
1.3.1.	Background.....	7
1.3.2.	Theory.....	7
1.4.	Am stars.....	8
1.4.1.	Background.....	8
1.4.2.	Theory.....	9
2.	The Analysis	10
2.1.	Tools	10
2.1.1.	TempLogG.....	10
2.1.2.	ATC.....	10
2.1.3.	The Vienna Atomic Line (VALD) database	11
2.1.4.	LLmodels	11
2.1.5.	Synth3.....	11
2.1.6.	Synth_mag.....	11
2.1.7.	Rotate_OLEG	11
2.2.	Synthetic solar spectrum	12
2.3.	Data reduction	15
2.3.1.	General description of the obtained spectra	15
2.3.2.	Continuum normalization	15
2.3.3.	Correction of hydrogen line orders.....	21
2.3.4.	S/N determination	23
2.4.	Radial and projected rotational velocities	23
2.4.1.	Radial velocity.....	23
	Cross correlation method.....	24
	Line fitting method.....	28
2.5.	Projected rotational velocity.....	30
3.	The iterative approach.....	31
3.1.	Principles	31
3.2.	The fundamental parameter iteration scheme	35
3.2.1.	Element selection.....	36
3.2.2.	Line selection	36
3.2.3.	The line fitting process.....	36
	Selecting the fitting width	37
3.2.4.	Step 1 - First microturbulence determination	38
3.2.5.	Step 2 - First gravity determination	40
3.2.6.	Step 3 - First effective temperature determination.....	42
3.2.7.	Step 4 - Refining the gravity.....	45
3.2.8.	Step 5 - Refining the microturbulence.....	45
3.2.9.	Step 6 - Refining the gravity.....	46
3.2.10.	Step 7 - Refining the effective temperature	47
3.2.11.	Step 8 - Refining the gravity.....	47
3.3.	Element abundances	48
3.3.1.	Line selection for abundance determination	48
3.3.2.	Results	53
3.4.	Refining the parameters	56
3.4.1.	Refining the microturbulence	57
	Iron.....	57
	Chromium	59

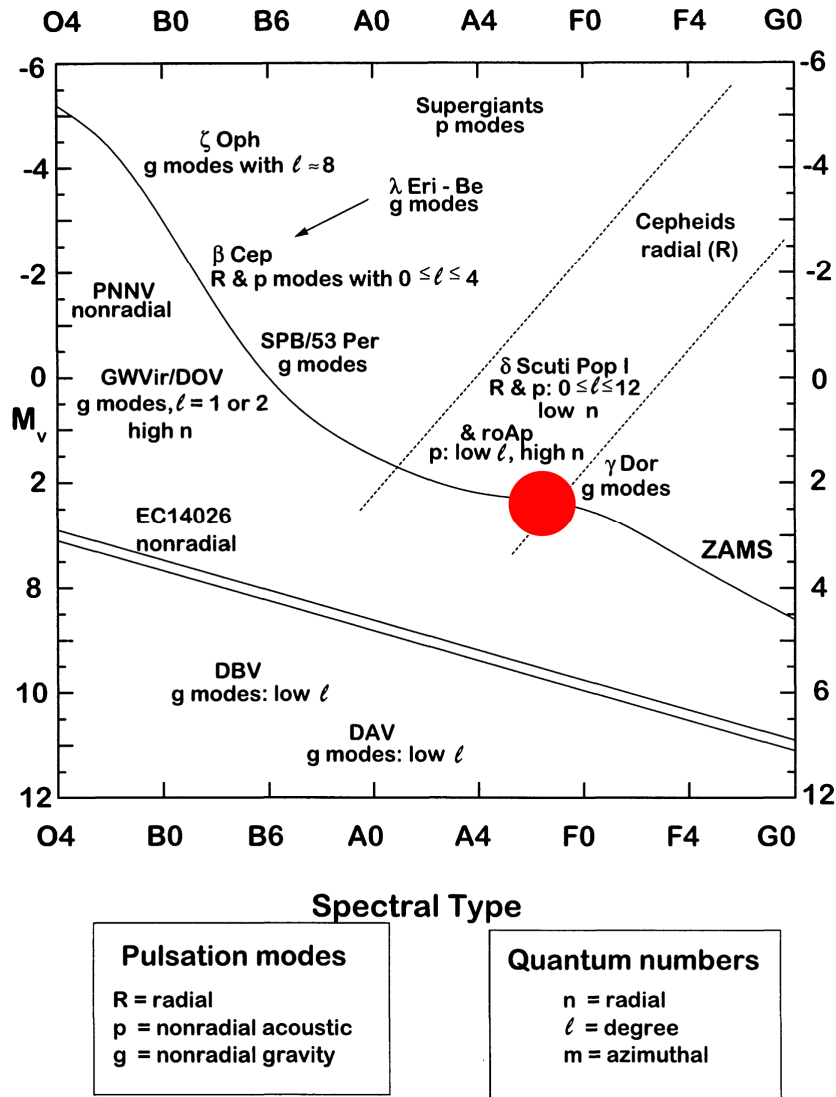
Titanium	60
Nickel	61
Summary.....	61
3.4.2. Refining the gravity	63
Iron.....	63
Chromium	64
Titanium	65
Summary.....	66
3.4.3. Refining the effective temperature	66
Iron.....	66
Chromium	67
Titanium	68
Nickel	69
Summary.....	69
3.5. Final abundances	70
3.5.1. Individual elements	74
C, Sc, Ti, Zr and Ca	74
N	75
K.....	75
Cl.....	76
Eu.....	76
Comparison between observation and synthesis	77
4. Discussion of errors	78
4.1. Continuum errors	78
4.2. Influence of the S/N ratio	80
4.3. Influence of the radial velocity accuracy	81
4.4. Influence of the projected rotational velocity accuracy	81
4.5. Errors of the fundamental parameters	82
4.5.1. Microturbulence	83
Iron.....	83
Chromium	83
Titanium	84
Nickel	84
Summary.....	85
4.5.2. Gravity	85
Iron.....	86
Chromium	86
Titanium	87
Summary.....	87
4.5.3. Temperature	87
Iron.....	87
Titanium	88
Nickel	88
Summary.....	89
4.6. Error estimations for abundances	89
4.7. Check of the fundamental parameters	91
4.7.1. Hydrogen lines	93
5. Magnetic field.....	95
5.1. Line splitting.....	95
5.2. Abundance versus Landé factor dependency	96
5.3. Polarimetry.....	97
5.4. Summary	98
6. Conclusion	98

7. References	100
Zusammenfassung	102
Lebenslauf	103

1. Introduction

1.1. HD 8801

HD 8801 is a main sequence star that lies in the overlapping region of the γ Doradus and δ Scuti instability strips (see Figure 1). Figure 2 shows an H-R diagram taken from Henry & Fekel (2005) with the position of HD 8801 among other γ Doradus stars. Figure 3 shows the power spectra for HD 8801 taken from the same publication.



The position of the δ Scuti variables in relation to other types of variables of Pop. I in the hot part of the HRD. Some positions of the variables are tentative and some mode identifications and other recent information may be speculative. The position of the EC14026 = sdB stars was taken from Koen et al. (1998).

Figure 1: H-R diagram with the positions of different pulsating stars. The red dot marks the region, where HD 8801 is located, Breger & Montgomery (2000).

“Location of 54 confirmed γ Doradus stars in the H-R diagram, including the 11 stars discussed in the paper by Henry & Fekel (2005). Solid lines indicate the observed average locations of normal main-sequence (V), subgiant (IV), and giant (III) stars in the diagram. Both components of two of the double-lined spectroscopic binaries are plotted for a total of 56 individual stars. Stars with well-determined locations in the diagram are plotted with filled symbols, while those with somewhat greater uncertainty (most of the double-lined binary components) are plotted with open symbols. One star, HD 209295, is plotted with a cross, since its γ Doradus pulsation is likely tidally excited. HD 8801, the only star known to pulsate intrinsically at both γ Doradus and δ Scuti frequencies, is plotted as a circled point. The dotted lines indicate the boundaries of the δ Scuti instability strip, converted from those of Breger (2000). The dashed lines show the observed domain of the γ Doradus pulsators, adopted from Fekel et al. (2003). The triple-dot-dashed lines show the outer edges of the theoretical boundaries of the γ Doradus instability strip, converted from those of Warner et al. (2003).” (Henry and Fekel, 2003)

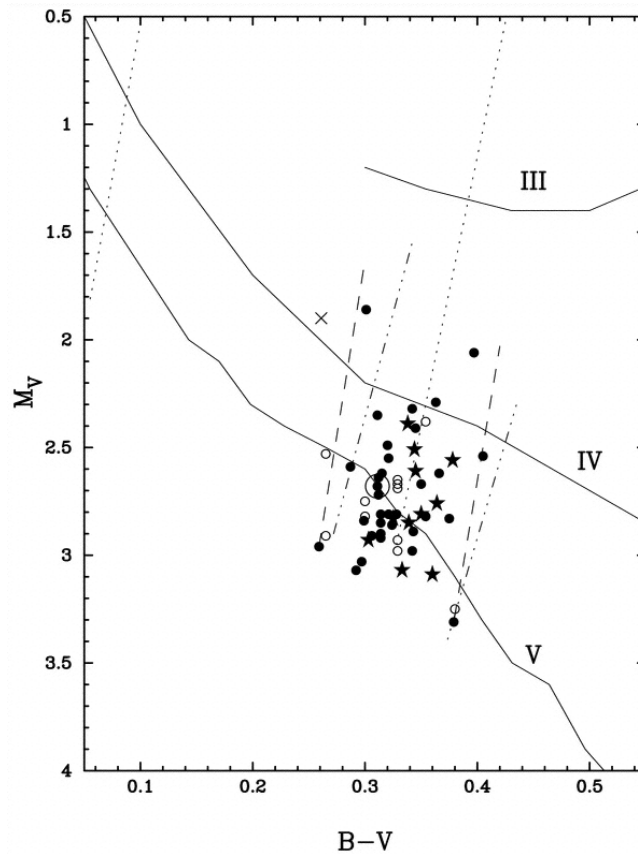


Figure 2: H-R diagram with the position of HD 8801 among other γ Doradus stars, Henry & Fekel (2003).

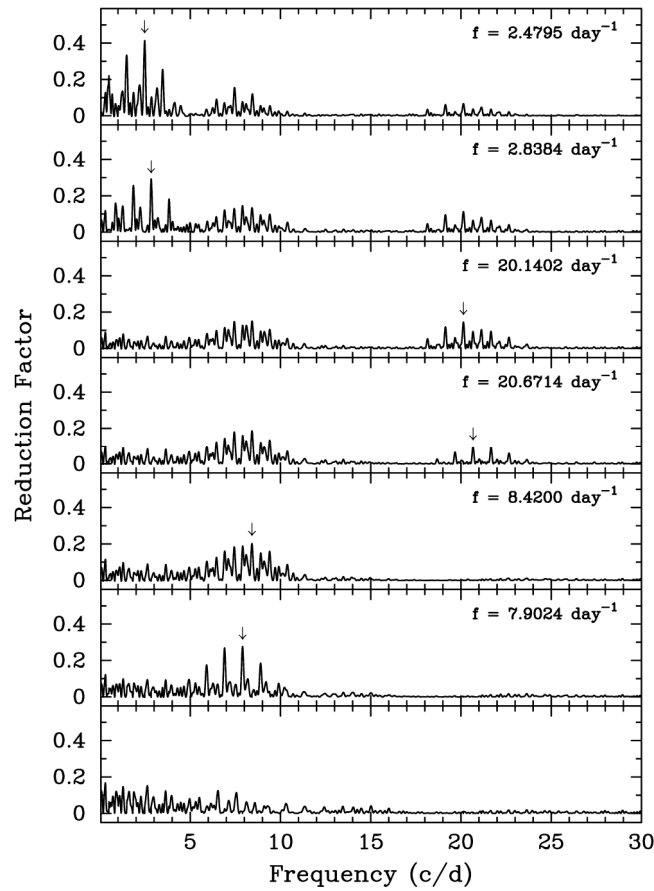


Figure 3: Power spectra of six nights of HD 8801 Δb photometry. Frequencies are marked and fixed for the analyses in the subsequent panels (values given in corner). The first two frequencies are in the range of γ Doradus pulsations, the last four frequencies are typical of δ Scuti stars, Henry & Fekel (2005).

Ra	01h 27m 26.6729s	<i>Astron. Astrophys.</i> , 323, L49-L52 (1997)
Dec	+41° 06' 04.168"	<i>Astron. Astrophys.</i> , 323, L49-L52 (1997)
Parallax	17.91 mas	<i>Astron. Astrophys.</i> , 323, L49-L52 (1997)
V	6.46 mag	<i>Astron. J.</i> , 83, 606-614 (1978)
B-V	0.27 mag	<i>Astron. J.</i> , 83, 606-614 (1978)
U-B	0.03 mag	<i>Astron. J.</i> , 83, 606-614 (1978)
Hbeta	2.748	<i>Astron. Astrophys., Suppl. Ser.</i> , 129, 431-433 (1998)
b-y	0.187	<i>Astron. Astrophys., Suppl. Ser.</i> , 129, 431-433 (1998)
m1	0.196	<i>Astron. Astrophys., Suppl. Ser.</i> , 129, 431-433 (1998)
c1	0.684	<i>Astron. Astrophys., Suppl. Ser.</i> , 129, 431-433 (1998)
vsini	(78 km/s)	<i>Astron. Astrophys.</i> , 393, 897-911 (2002)
	(68 km/s)	<i>Astrophys. J., Suppl. Ser.</i> , 99, 135-172 (1995)
	55 km/s	<i>Astron. J.</i> , 129, 2026-2033 (2005)
Spectral type	Am A7-F0	<i>Astron. Astrophys., Suppl. Ser.</i> , 21, 25-32 (1975)
	A7m	<i>Publ. Astron. Soc. Pac.</i> , 80, 746-749 (1968)
	A7m	<i>Astron. J.</i> , 74, 375-406 (1969)

Table 1: Information extracted from SIMBAD database.

Table 2 and Table 3 show the results for different calibrations using the data from Table 1 above and the software *TempLogG* (see chapter 2.1.1 for a description).

Calibration	M_v [mag]	T_{eff} [K]	$\log g$ [cm/s ²]	$\log(N_{\text{Fe}}/N_{\text{H}})_{\text{HD8801}} - \log(N_{\text{Fe}}/N_{\text{H}})_{\text{sun}}$
Moon (1985)	2.73	7254	4.13	0.149
Napiwotzki (1993)	2.73	6899	3.90	0.149
Balona (1994)	2.73	7373	4.09	0.149
Ribas (1997)	2.73	7269	4.16	0.149
Castelli (1997)	2.73	6698	3.46	0.149

Table 2: Atmospheric parameters derived from Strömgren photometry based on different calibrations.

T_{eff} [K]	$\log g$ [cm/s ²]	Radius [R_{sun}]	Sp. type
7087	4.21	1.497	F1

Table 3: Results derived from Johnson photometry, Gray (1992).

In this analysis, the calibration by Moon (1985) was used to calculate the starting values, as its values lie in between the others.

1.2. Gamma Doradus stars

1.2.1. Background

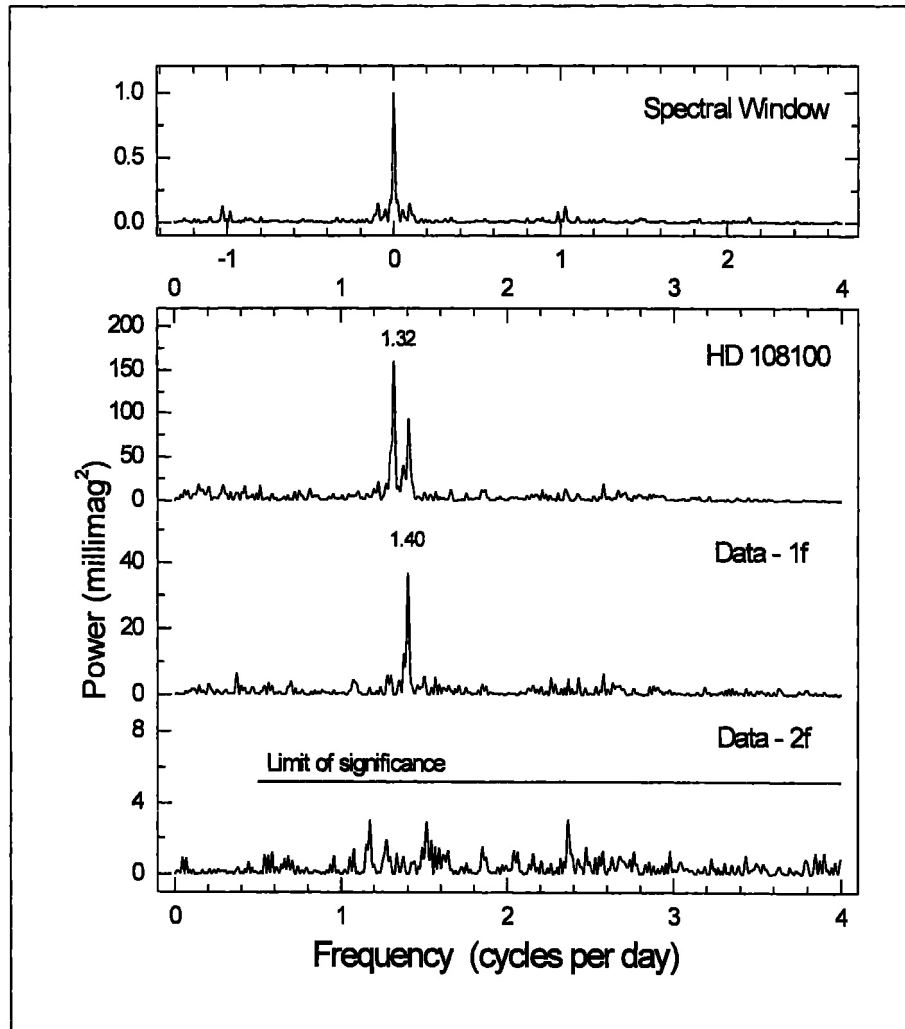
Beginning in the late 70s, main-sequence stars with periods longer than those of δ Scuti stars were observed. Abt et al. (1983) observed the F2 IV star HD 164615, today identified as a γ Doradus star, which showed varying light variations by 0.05 mag in a period of 0.815 days. They explained their observations with a spotted star model as any other explanations were ruled out at that time.

In 1990, Krisciunas and Guinan photometrically analysed 9 Aurigae (F0 V). A DFT analysis of the light curves showed frequencies of 34.3, 35.8 and 36.5 days for U-, B- and V-data which are too long for δ Scuti stars. Further observations were proposed to check the existence of short-term δ Scuti variations. Three years later, due to additional data, Krisciunas was able to rule out such short-term light variations and for the first time grouped stars with similar observational findings: HD 96008, γ Doradus and HD 164615. He called them “variables without a cause” and suggested nonradial gravity-modes as an explanation. As these stars are on the transition between stars with strongly radiative envelopes and stars with convective envelopes, and models for these stars didn’t exist at that time, he stated that “it should not be surprising that there are discoveries to be made”.

In 1999, Kaye, Handler, Krisciunas together with Poretti and Zerbi (Kaye et al. 1999) defined a new class of pulsating stars with the prototype γ Doradus.

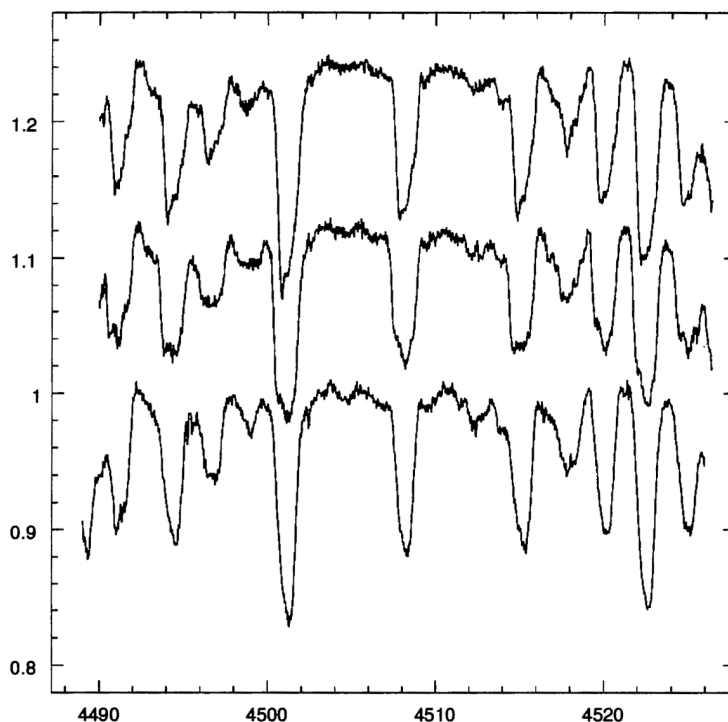
- Spectral type A7 – F5, luminosity class IV, IV-V or V
- Periodicity between 0.4 and 3 days (Figure 4 shows an example)
- Peak-to-peak amplitudes ≤ 0.1 mag in Johnson V
- Star must not vary exclusively by other mechanisms

Additionally, multiple periods, amplitude modulation, spectroscopic variations such as low-amplitude radial velocity variations and photospheric line profile variations are common among these stars (see Figure 5).



Power spectrum of HD 108100 in the 0 to 4 c/d range using all the V data obtained during 1996 judged by us to be "good". Note the excellent spectral window. The power spectra are shown before and after applying multiple-frequency solutions.

Figure 4: Power spectrum of the γ Doradus star HD 108100, Breger et al. (1996).



Three high-resolution spectra of HR 2740 (Bottom: JD 2448955.84; middle: JD 2449651.83; top: 2449654.84). The star was originally observed as a standard for rotational velocity measurements, but it exhibits line profile variations indicative of pulsation.

Figure 5: Line profile variations in the γ Dor. star HD 2740, Poretti & Mategazza (1998).

1.2.2. Theory

The variations of these stars are consistent with a model of high-order(n), low-degree(l), nonradial, gravity-mode oscillations. As a driving mechanism for this group of stars, Guzik, Kaye et al. (2000) presented calculations based on the modulation of the radiative flux by convection. The pulsation driving occurs at the base of an envelope convection zone. During a pulsation cycle, the luminosity is blocked at the convection zone base and therefore drives the pulsation. This mechanism was first introduced by Pesnell (1987) as “convective blocking” and further developed by Li (1992). It is independent of the κ - γ mechanism, which is responsible for the pulsation in δ Scuti stars. The convective blocking mechanism was first suggested to explain pulsations in white dwarfs but was not viable due to the fact that the convective timescale in these objects is much shorter than the pulsation period. Therefore the frozen-in convection approximation is not valid. For γ Doradus stars the local convective timescale at the convection zone base can be comparable to or longer than the pulsation period. In such a case, the convection is unable to adapt completely to the changing physical conditions during a pulsation cycle and the frozen-in approximation becomes reasonable. The blue edge of the γ Doradus instability strip can be described by the fact that the convection zone becomes shallower with increasing temperature and therefore can adapt to carry the pulsationally modulated flux at its base. The red edge is explained by the increasing depth of the convection zone with decreasing temperature. In these deeper envelope regions, the radiative fluctuations are smaller and hence can be overwhelmed by damping.

1.3. Delta Scuti stars

1.3.1. Background

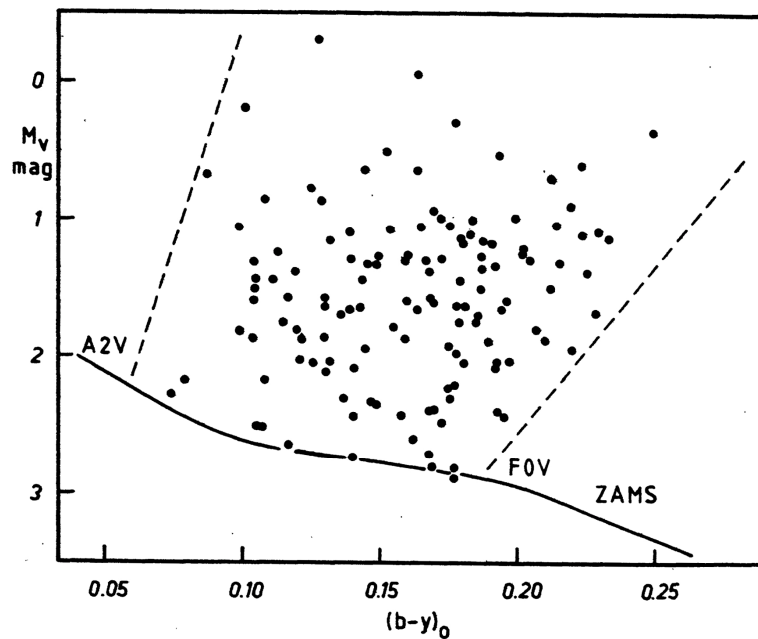
The radial velocity of δ Scuti, the prototype for the whole group, was first announced to be variable in 1899 by W.H. Wright from observations made with the 3-prism spectrograph at the Lick observatory. In 1935, E. Fath and A. Colacevich revisited the study of δ Scuti and Colacevich claimed that it couldn't be a spectroscopic binary due to its combination of radial velocity amplitude and period (Fath 1935). Two years later, Fath detected multiple periods. By 1956, four δ Scuti stars were known (Eggen 1956). With the emergence of the first computers in the 60s, theoretical modelling of pulsating variables commenced. Up to date, several hundreds of stars belonging to this type of pulsators are known and the number is increasing rapidly with the photometric monitoring projects currently under progress.

One of the leading science groups in the study of this type of pulsating stars is the TOPS (Theory and Observation of Pulsating Stars) group around M. Breger at the University of Vienna who also founded the Delta Scuti network (DSN), which is a collaboration of astronomers from all around the globe who observe and study short period variable stars. News are frequently communicated in CoAst (Communications in Asteroseismology) and workshops (see <http://www.univie.ac.at/tops/> for further information).

1.3.2. Theory

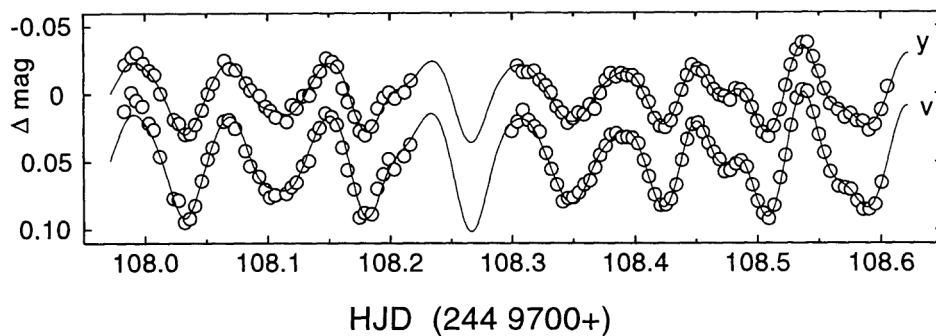
δ Scuti stars are located at the interception of the Cepheid instability strip with the main sequence and are of spectral type A – F (see Figure 6). Their pulsational periods lie between 0.5 and 6 hours and correspond to low order p- and g-modes (see Figure 7). Responsible for the driving of these pulsations is the κ - γ mechanism in the He II partial ionization zone.

The blue edge of the δ Scuti instability strip has been determined by many authors for radial and for non-radial modes (e.g. Pamyatnykh 2000). The red edge is more difficult as it requires a non-adiabatic treatment of the interaction between convection and pulsation (Baker & Kippenhahn 1965). One approach is the time-dependent convection treatment which was also successfully used to determine the theoretical γ Doradus instability strip (Dupret et al. 2004).



Position of Delta Scuti stars in the H-R Diagram.

Figure 6: δ Scuti stars in the HRD, Breger & Stockenhuber (1983).



Sample light curves in the Stromgren y and v filters of a typical δ Scuti variable (FG Vir). The data were taken from a multisite campaign of FG Vir (Breger et al. 1998). The predicted variability is shown by a solid curve. Notice that the seemingly irregular light curves and bumps are caused by multiperiodicity.

Figure 7: Typical δ Scuti lightcurve, Breger & Montgomery (2000).

1.4. Am stars

1.4.1. Background

Titus & Morgan (1940) first recognized the metallic line A stars (Am stars) as a distinct class of peculiar stars. Wolff (1983) gives a detailed overview about the status of the research on A stars.

Am stars are A stars that show stronger heavy-element lines than normal A stars. Typically, Ca II and Sc II lines are too weak and correspond to early type A stars whereas the heavy-element lines correspond to late A or even early F type stars.

Due to the enhanced metal lines, the B-V index of Am stars is usually redder than their temperature derived from hydrogen lines would suggest. This is because the effect of the enhanced absorption is stronger in the blue than in the red part of the spectrum (Lane & Lester 1984). This is also the case for HD 8801 where the spectroscopically determined temperature is about 300 K higher than the photometrically determined.

According to Greenstein (1949), elements with ionization potentials close to hydrogen (e.g. C and O) can be underabundant. Böhm-Vitense (1976) noted that elements with ionization energies comparable to those of helium (C, Sc, Zr and Ca) can have lower abundances than most of the heavy elements. This is also the case for HD 8801.

1.4.2. Theory

Several processes have been suggested to explain the abnormal abundances in Am stars in the past. A detailed discussion can be found in Böhm-Vitense (2006).

1. Nuclear reactions can be ruled out because Am stars do not have a core temperature high enough to produce elements heavier than He. Additionally, the abundance patterns of Am stars do not agree with the expectations for nuclear reactions. A and Am stars do not show emission lines, so that nuclear reactions in hot coronae are also excluded.
2. Mass accretion from supernova explosions is improbable because of the short lifetime of A stars and the high number of Am stars among them. In addition, the heavy element abundances do not reflect the pattern in supernovae ejecta.
3. Diffusion processes due to gravitational settling and radiative levitation would cause Ca II and Mg II resonance lines to behave similar (Watson 1970) but they do not as shown by Böhm-Vitense (1980).
4. Non-LTE effects were studied by Conti (1970) and were found to be unimportant.
5. Abt (1961, 1965) showed that nearly all Am stars are binaries and rotate more slowly than normal A stars due to the rotational braking effect caused by the companion. The slower rotation should cause differences in the convection zones which can in turn cause different line strengths for the heavy elements. New studies have shown, that neither A nor Am stars have convection zones strong enough to show such effects.

The Am star phenomenon stops, as convection starts to become efficient in the stellar atmosphere. This happens at an effective temperature of approximately 7500 K when mixing extends down to the bottom of the convection zone. HD 8801 has a temperature of 7560 K and shows both, strong Am star characteristics and γ Doradus pulsations which are directly connected to convection.

There is still discussion about the mechanism responsible for the Am phenomenon. One up-to-date explanation is the accretion of material from surrounding interstellar gas and interstellar grains. This process is similar to the mechanism which explains the λ Bootis phenomenon with the exception that a weak stellar magnetic field in the Am stars is responsible for a depletion of hydrogen in the accreted material (Havnes & Conti 1971). The element pattern of the accreted material is then modulated by so called "charge-exchange reactions" which explain the normal or even underabundances of some elements (this is shown in chapter 0 and 6). This theory is also supported by the rather high rotational velocity of the λ Bootis stars which were not braked by the interaction of a magnetic field with the ISM (Böhm-Vitense 2006).

2. The Analysis

The whole process can be seen as a sequence of analysis steps in which the knowledge increases from step to step and the result from one step is used as an input for the next analysis step. This scheme is shown in Figure 8.

The workflow

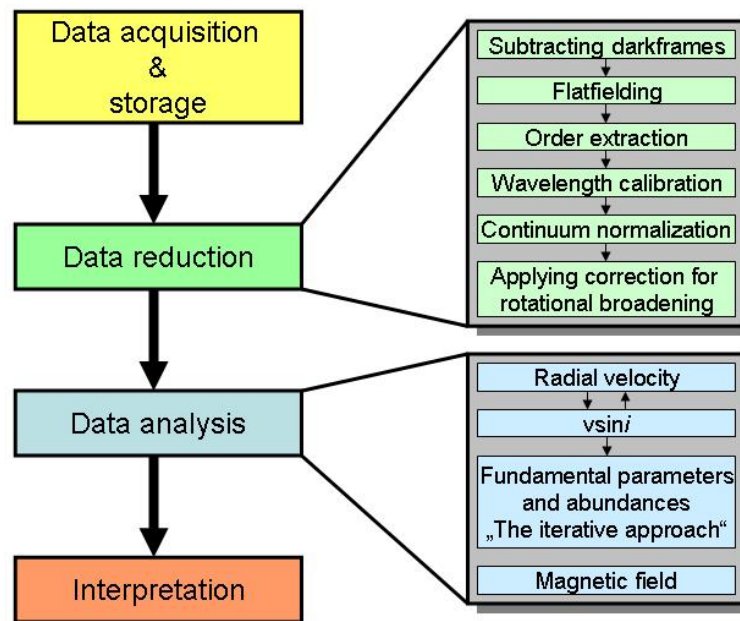


Figure 8: The workflow in abundance analysis.

2.1. Tools

2.1.1. TempLogG

The *TempLogG* software is a black box for the calculation of the fundamental parameters using well known calibrations. The basic code was written in 1995 by N.Y. Rogers following the masters theses of E.M. Fresno (1994), extended in 2002 by Ch. Stütz and J. Nendwich and further developed by A. Kaiser to *TempLogG TNG* Version 1.4 (Kaiser 2006) which was used in this analysis.

For a detailed description see <http://www.univie.ac.at/asap/templogg/Manual.php>.

2.1.2. ATC

The *ATC* (atmospheric tools compilation) are several model and synthesis codes (*LLmodels*, *Synth3*, *Synth_mag*,...) combined under a user interface. The interface

additionally contains several editors for files typically used when calculating models or syntheses with these codes, as well as a line-core-fitting (*linfit*) routine for abundance analysis.

2.1.3. The Vienna Atomic Line (VALD) database

One of the most important prerequisites for stellar analysis is the exact knowledge of atomic parameters for as many spectral lines as possible. For this analysis, the Vienna Atomic Line Database was used. It currently contains information of several million transitions compiled from dozens of individual catalogs (Heiter et al. 2008). Additionally, several tools to extract spectral lines are provided (*Preselect*, *Select*).

2.1.4. LLmodels

The stellar models used in this analysis were mainly calculated with the code *LLmodels* (Shulyak et al. 2004) in ODF (**o**pcacity **d**istribution **f**unction)-mode which means, that for the opacity calculations, the Kurucz ODF-tables were used. This increased the calculation speed by a factor of 100 compared to the line-by-line (LL) approach (Stütz 2005). For the determination of the final abundances, an LL-model was calculated in order to include the influence of the non solar abundance pattern on the stellar atmosphere. The abundance differences due to the changes in the atmospheric structure are shown in Figure 73.

The local full spectrum turbulence convection model of Canuto & Mazzitelli (1991) was used in the code and throughout this analysis.

2.1.5. Synth3

Synth3 is a fast synthesis code based on the code *SYNTH* written by N. Piskunov and was used in this analysis. It calculates spectra based on a stellar model as produced by the LL-model code for static, plane parallel atmospheres in LTE (Nesvacil, Stütz, Weiss 2003). The user interface *ATC* written by Ch. Stütz uses this code to find the best fitting abundance for a spectral line or feature. This increased the speed dramatically compared to a purely manual approach.

2.1.6. Synth_mag

Synth_mag is a synthesis code, written by O. Kochukov to synthesize spectra for a stellar atmosphere including a magnetic field. The field is configured by three magnetic field strengths (radial, meridional and tangential field component). The Zeeman pattern is preprocessed on the basis of the *VALD* line selection and used in the calculation. The output is a spectrum for each stokes parameter.

2.1.7. Rotate_OLEG

This spectrum viewer software developed by O. Kochukov allows to view the observed and synthesized spectra together. The synthesis can be shifted in wavelength and be folded with a rotational broadening function until the optimal value is found using a χ^2 -fitting algorithm. This software was used to obtain the radial velocity and the projected rotational velocity.

2.2. Synthetic solar spectrum

In order to check the quality and completeness of the spectral line database, the capabilities of the used atmospheric model calculation and synthesis codes, a comparison between a synthetic and observed solar spectrum is helpful and instructive.

Using values from literature (Stix 2004) for the atmospheric parameters of the sun (see Table 4), calculating an ODF-model with the atmospheric model calculation code *LLmodels* and using the synthesis code *Synth3* (see chapter 2.1.4 and 2.1.5 for a description of the tools), creates the synthetic solar spectrum.

T_{eff}	5778 K
$\log g$	4.44 cm/s ²
v_{mic}	1 km/s
$v \sin i$	2 km/s

Table 4: Atmospheric parameters for the sun.

For comparison, a solar spectrum taken with the FEROS spectrograph mounted at the ESO 1.52m telescope at La Silla, Chile during an observation run in 2004 is used. The spectrograph has a resolution of 48000 which is sufficient for abundance analyses. The plots in Figure 9 and Figure 10 show two results.

Whereas the synthesis can fit the observation quite well in the spectral range shown in Figure 9, the comparability for the part shown in Figure 10 is rather disappointing. Nearly none of the observed spectral lines can be synthesized well. Some features (4518 - 4519 Å) are completely different; some line strengths are totally off (Co I at 4517.090 Å). There are several reasons for these discrepancies:

- Missing, wrong or sometimes even guessed atomic parameters.
- The temperature of only 5780 K is at the lower limit of the atmospheric model calculation code *LLmodels*.
- The simplified convection treatment used in *LLmodels* and the synthesis code *Synth3* (see chapter 0 for a description of the tools).
- Opacities were taken from precalculated ODF-tables only.
- Model simplifications (plane parallel geometry, no magnetic fields etc.).

Doing abundance analysis, one has to keep in mind these difficulties and limitations and should not be too concerned, if some features of the stellar spectrum cannot be synthesized. Additionally, this comparison shows the need of carefully selecting lines used for an analysis. Taking “all” lines regardless of their quality, would increase the scatter in the abundance determination to such an extent, that the sometimes very weak dependencies used to determine the atmospheric parameters, would become invisible. Which lines to use is unfortunately more or less based on experience. Comparing a synthetic solar with an observed solar spectrum and then selecting well fitted lines can only be a solution for stars, comparable to the sun as the quality of the fit is a function of the atmospheric parameters.

The Analysis

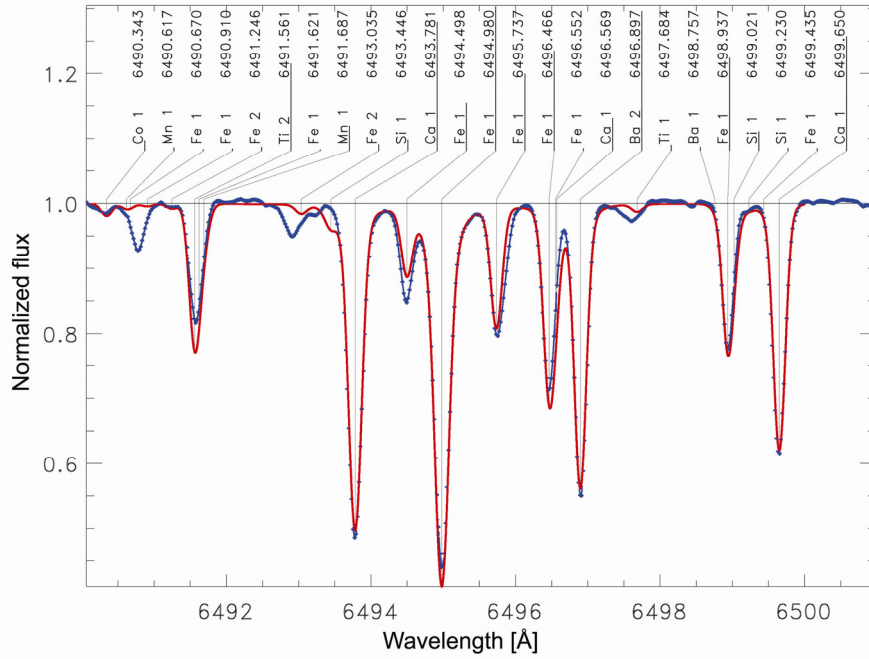


Figure 9: Comparison between synthetic (red) and observed (blue) solar spectrum.

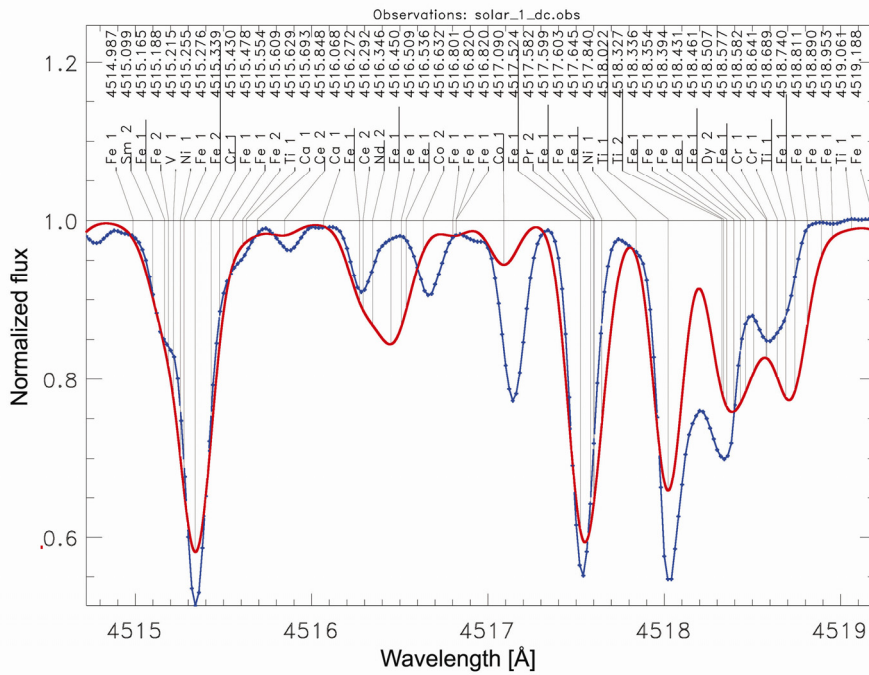


Figure 10: Comparison between synthetic (red) and observed (blue) solar spectrum.

In order to check whether or not such a line selection based on well fitted solar lines is suitable for the case of HD 8801, the following experiment was made.

1. Fitting the iron abundance of the sun using the same line selection as for HD 8801 (a line sample consisting of 112 mostly unblended Fe I/II lines).
2. Among them, selecting the lines with the lowest RMS error (< 1) and smallest deviation (< 0.1 dex) from the known solar abundance (-4.59 dex).
3. Using only these “best” lines for the calculation of HD 8801’s iron abundance.

The result is shown in Figure 11. The black squares mark the individual iron abundances for the 17 best fitted lines in the solar spectrum. The red circles show the iron abundances of HD 8801 for the same 17 lines. As the outlier at -4.1 dex demonstrates, one can not be sure that a line, fitted well in the solar spectrum can also be fitted well in the spectrum of HD 8801 although only unblended lines were selected. Additionally, the number of useable lines is decreased by a large amount (only 17 out of 112 lines were used) which makes it impossible to apply this selection method to elements with a priori few measurable lines.

Due to the high rotational velocity of HD 8801, the amount of useable lines is already very limited and such a solar based line selection was not applied for this analysis.

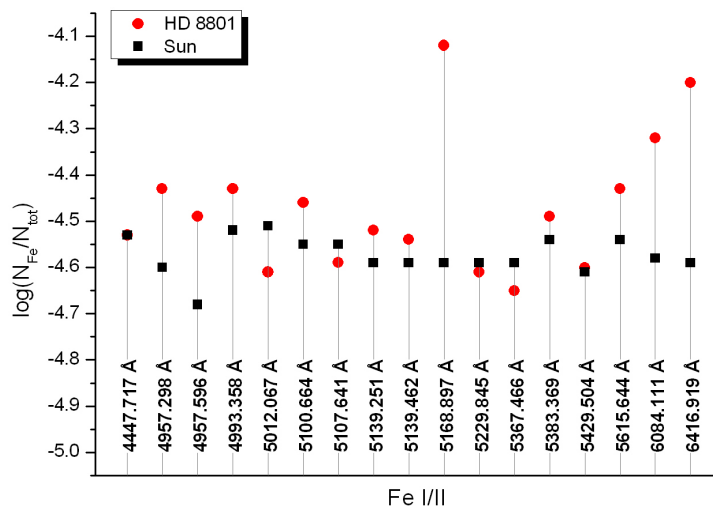


Figure 11: Individual line abundances using same line sample for the sun and HD 8801.

2.3. Data reduction

2.3.1. General description of the obtained spectra

The spectrum of HD 8801 was taken by G. Handler at the 2.7m telescope at the McDonald observatory on 10th July 2004. He used the cross-dispersed Echelle spectrometer at the Coudé focus ($f/32.5$) with a resolution of 60 000. Two spectra were obtained, each with an integration time of 600 seconds.

Each of the two data files containing the observations consists of 62 Echelle orders covering the wavelength range from 3630 Å to 10275 Å. The orders close to the red and blue limits could not be used, as the continuum normalization failed due to a very low S/N ratio and the large amount of overlapping spectral lines that made it impossible to find adequate continuum points. A range from 4143 Å to 9193 Å was left. A large handicap of this spectrograph is the fact, that gaps of several Ångströms between the individual Echelle orders are present. This reduces the useable spectral area and causes enormous troubles during the continuum normalization.

2.3.2. Continuum normalization

The subtraction of the dark frames, the flatfielding, the order extraction and the wavelength calibration were done by G. Handler, using standard IRAF routines.

For a spectral analysis, one is not interested in absolute fluxes but in fluxes relative to the continuum. The necessary semi-automatic reduction steps are described in the following section.

First, the two spectra were added with the task *scombine*, in order to increase the signal to noise level.

In the second step, an envelope was fitted to the observed spectrum. This envelope consists of a convolution of the dispersion function of the spectrograph, the response function of the detector and the continuum flux of the star itself. The dispersion and response function of the instrument could be measured, but the continuum flux of the star is unknown at the beginning of an analysis. So the result of this convolution has to be determined by fitting an envelope to the observation. Dividing the spectrum by the envelope fit results in normalized fluxes which are necessary for the further analysis.

In order to do this envelope fitting, the task *splot* with its inbuilt fitting routines was used with the parameters shown in Table 5 which were determined empirically in the middle of the observed spectrum (Echelle order 27) where the S/N ratio was best (see Figure 12).

A very difficult task is to fit orders contaminated with hydrogen lines (see Figure 13). These orders cannot be normalized in the typical way, as the spectrum never reaches the continuum. The normalization procedure for these orders is described in 2.3.3.

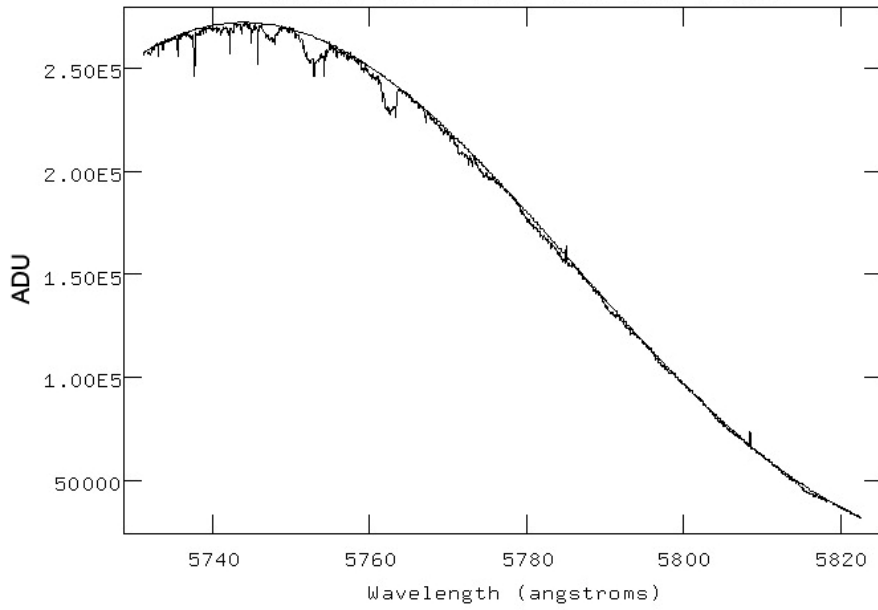


Figure 12: Observed spectrum with envelope fit for Echelle order 27.

Function	Legendre
Order	6
Low_reject	1
High_reject	4
Niterate	6
Grow	1

Table 5: Fitting parameters for IRAF task *splot*.

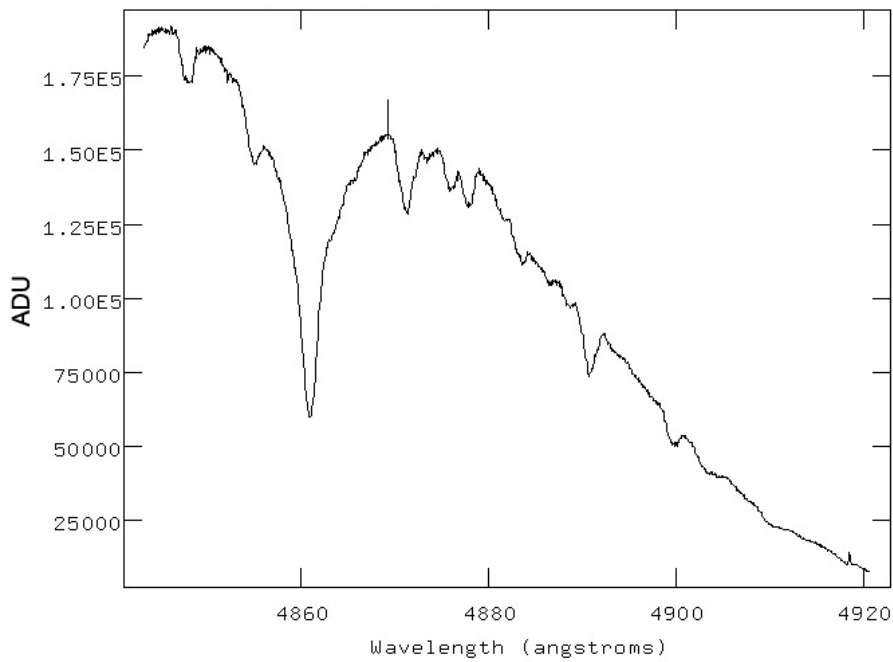


Figure 13: Echelle order 38 showing the H β line.

Especially in the blue part of the spectrum, the results produced by the semi-automatic reduction are unsatisfying. Due to the high line density, the spectral lines overlap and blend each other so that there are no parts, where only continuum radiation is visible. Additionally, the high rotational velocity causes the spectral lines to be very broad. This enhances the overlapping effect. Therefore, the upper points of the unnormalized spectrum, usually regarded to as continuum points, do no longer represent the continuum.

This is shown in Figure 14, where a synthetic spectrum is compared to the corresponding normalized observation. The upper points, which were identified as continuum points and were therefore set to 1 by the semi-automatic reduction, should in truth lie about 7% below the continuum.

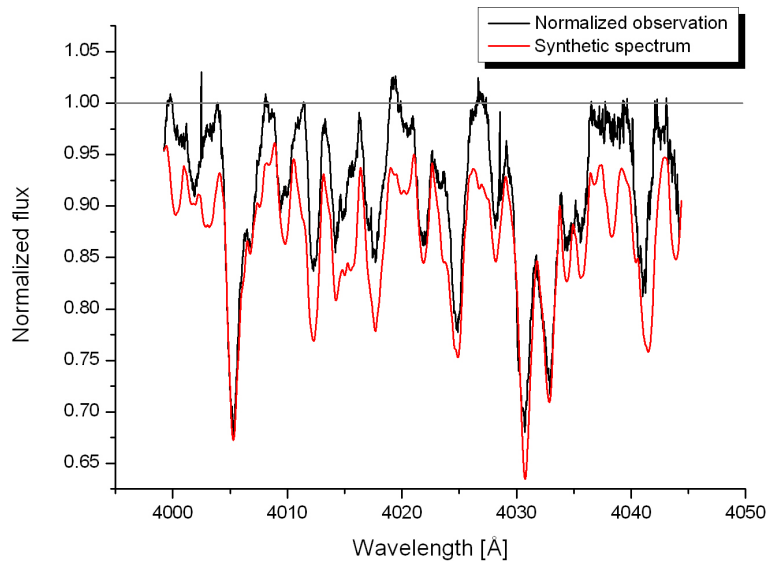


Figure 14: Comparison between normalized observation and synthetic spectrum.

In order to correct the semi-automatically normalized observation, a procedure was developed and tested on an artificial observation.

A simulated spectrum was created by multiplying a synthetic spectrum for one Echelle order with an artificial response function (order 53 from 4000 to 4045 Å as seen in Figure 15, black line). This spectrum was used as an input for the IRAF routines described above and the resulting continuum fit is shown in Figure 15 as the blue line.

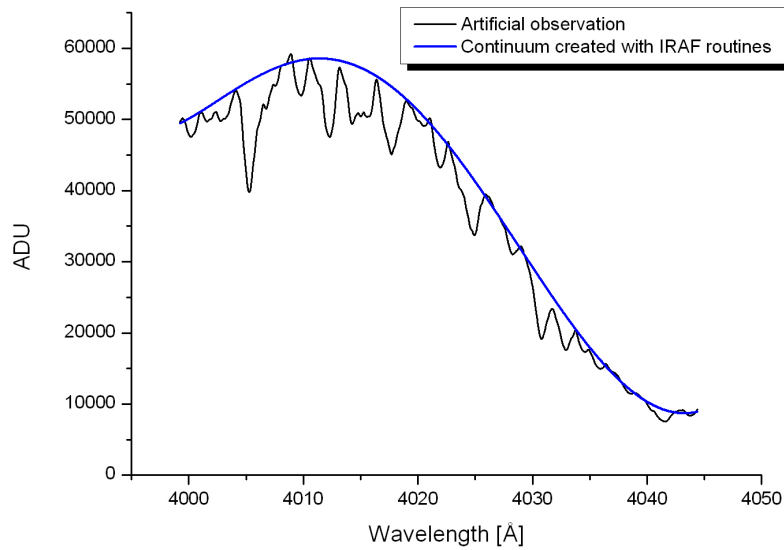


Figure 15: Artificial observation with continuum fit.

The spectrum was then divided by this continuum to get a normalized artificial observation. A comparison of the result with the real observation is shown in Figure 16. It shows that it is possible to reproduce the wrongly normalized observation well.

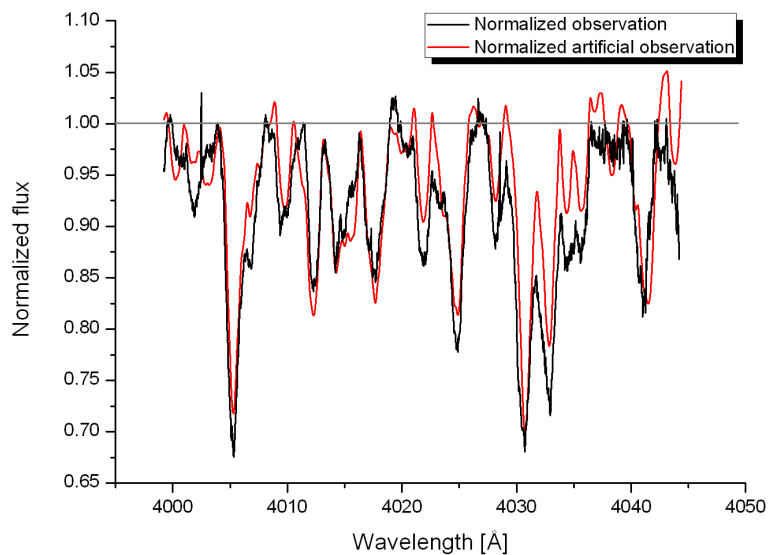


Figure 16: Comparison of normalized artificial spectrum and observed spectrum.

In a next step, the “wrong” continuum points were identified in the artificial observation. All data points between 0.99 and 1.01 of relative intensity were regarded as wrong continuum points and are marked in Figure 17.

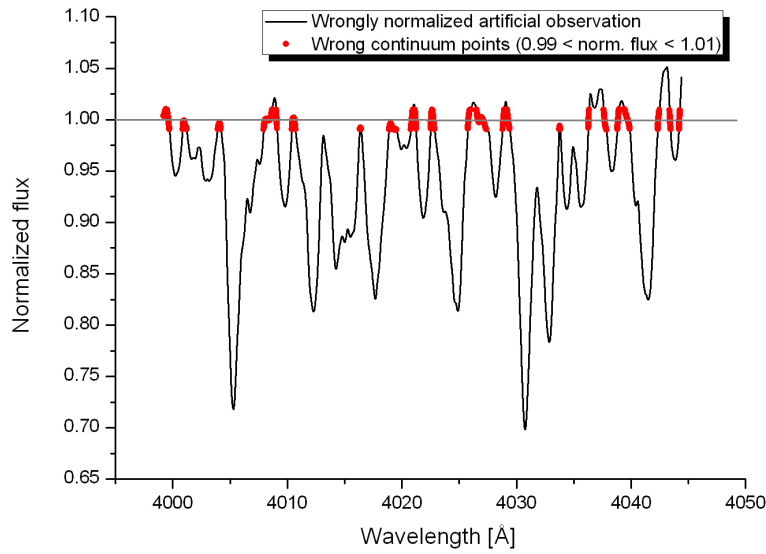


Figure 17: Identification of wrong continuum points.

In a further step, the intensities at the wavelengths of the wrong continuum points were compared to the corresponding intensities in the synthesis. Subtracting these intensities from each other and applying a polynomial fit results in Figure 18.

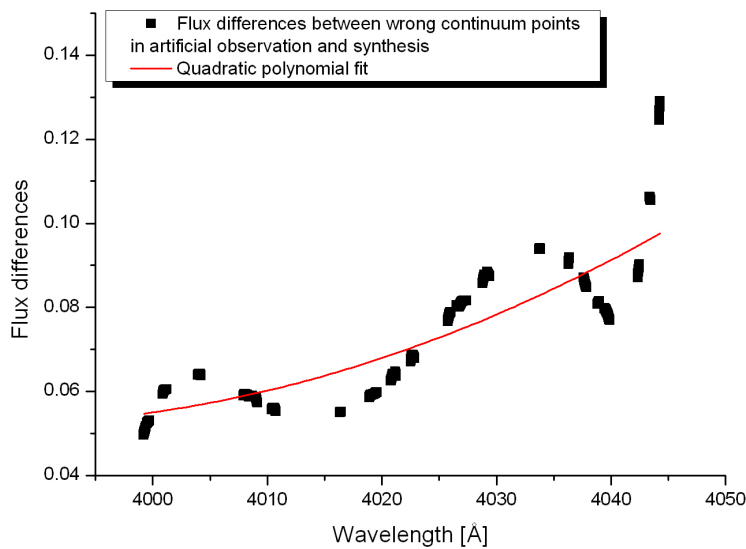


Figure 18: Flux differences and applied fit.

Finally, these differences were subtracted from unity to give the so called “continuum correction function” which was then multiplied with the artificial observation. This results in the normalized artificial observation as shown in Figure 19 together with the input synthesis and demonstrates the success of this method. Only small differences can be seen throughout the spectrum. Figure 20 shows the result after application to the original observation.

The Analysis

This procedure was then applied to all Echelle orders. The degree of the polynomial fit to the differences was applied individually but never exceeded three. In most cases, a linear fit was sufficient in order to avoid removing spectral features.

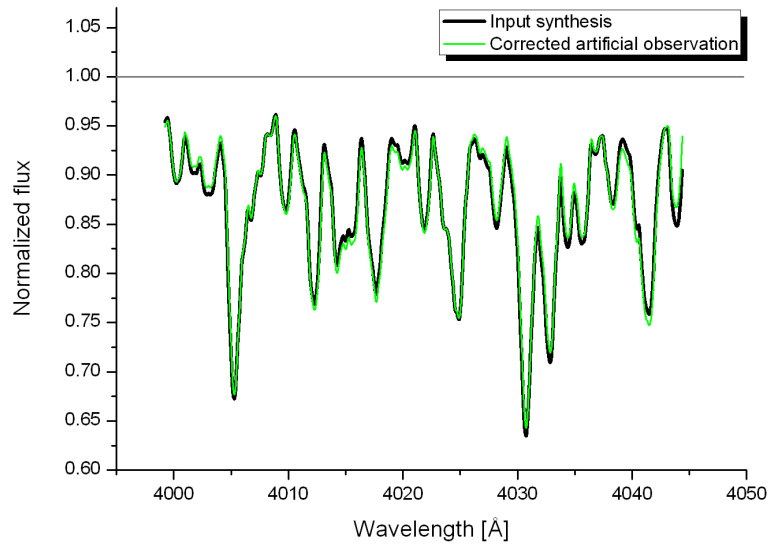


Figure 19: Result of the correction procedure applied to the artificial observation compared to the input synthesis.

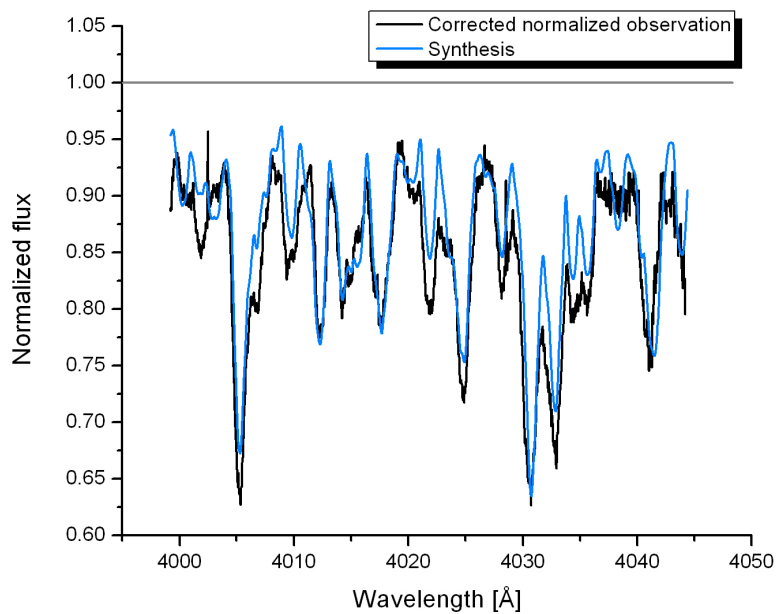


Figure 20: Result of the correction procedure applied to the original observation compared to the synthesis.

2.3.3. Correction of hydrogen line orders

H α and H β are the most interesting lines in the observed spectral region, because they show a strong dependency on the effective temperature of the star. The following procedure was applied to both of them but is explained in detail for H β only.

1. The continua for the neighbouring orders were plotted and bad fitted orders were rejected. In the case of H β , which lies in Echelle order 38, the orders 33 – 36, 41 and 42 were used. All others (order 37 and 39) were affected by the hydrogen line or showed instrumental artefacts (order 40).
2. 20 interpolation points were calculated for order 38 using B-splines. This is shown in Figure 21.

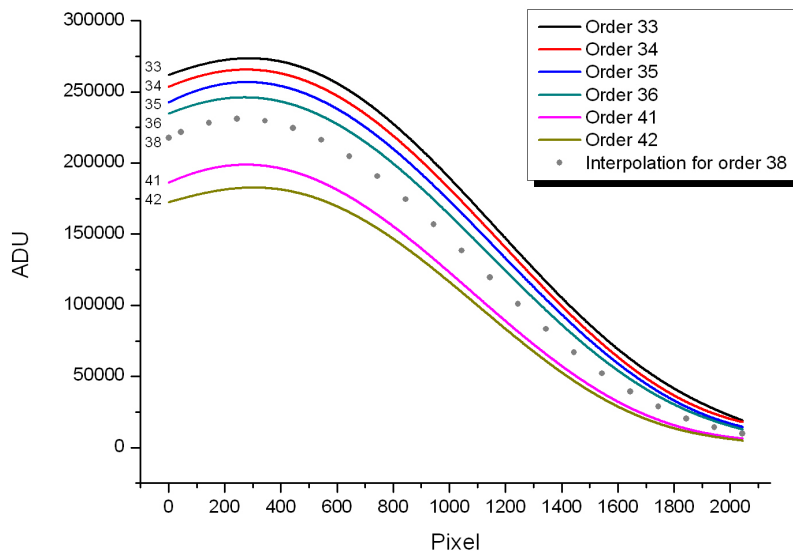


Figure 21: Echelle orders around H β including interpolation for order 38.

3. The interpolated data points were then fitted by an 8th order polynomial. This fit was used as continuum for Echelle order 38. Figure 22 shows the constructed continuum together with the observation.

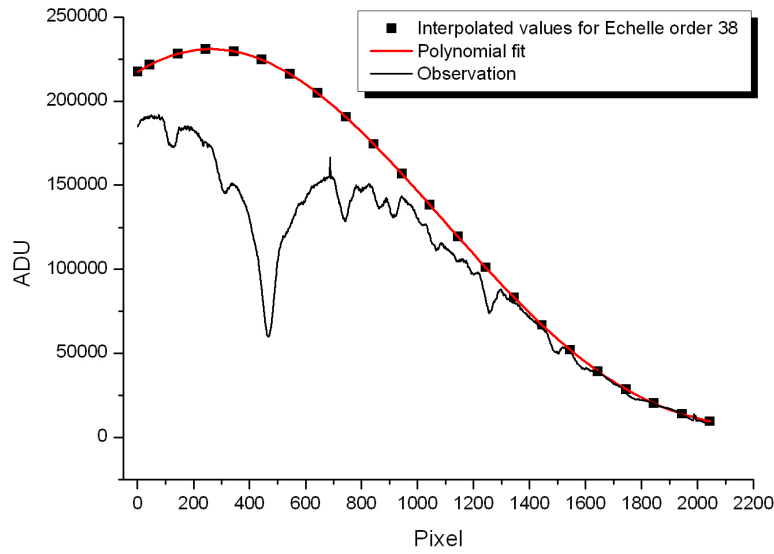


Figure 22: Constructed continuum and observation.

4. The observation was divided by the constructed continuum.
5. During the correction procedure described at the end of chapter 2.3.2, the semi-automatically normalized spectra were multiplied by a continuum correction function. The average values of these correction functions were now taken to correct the hydrogen order as the functions themselves could not be reproduced. These average continuum correction factors for the orders next to H β are shown in Figure 23. A linear fit was applied to calculate the factor for Echelle order 38.

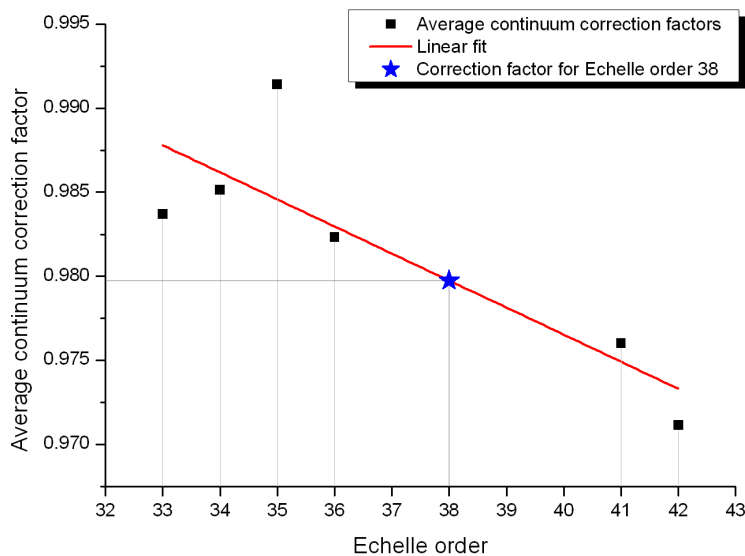


Figure 23: Continuum correction factors for Echelle orders next to H β line. The star marks the value for Echelle order 38 (0.97975).

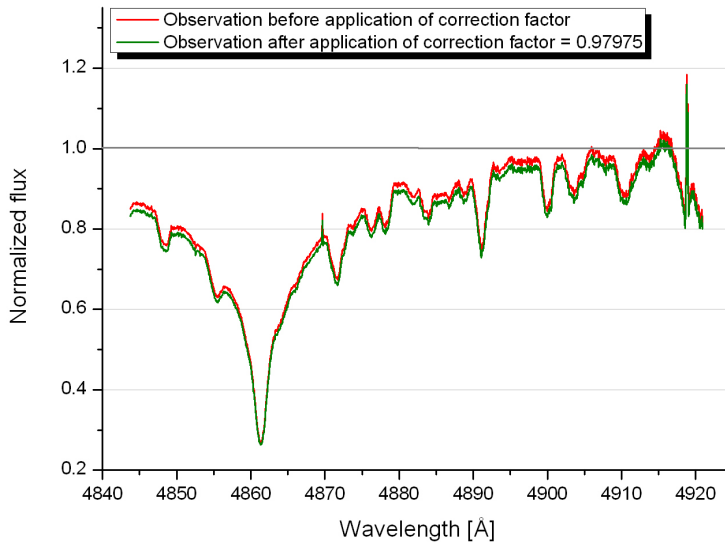


Figure 24: Observation before and after application of continuum correction factor.

For H α , four neighbouring Echelle orders on each side of the hydrogen line could be used to reconstruct the continuum. The contamination with metallic lines is less than for H β and the continuum correction factors were close to 1. Therefore the result is qualitatively better.

The successful correction allowed to use the hydrogen lines as a temperature indicator.

2.3.4. S/N determination

The signal to noise ratio is usually calculated as 1 divided by the standard deviation in the normalized flux at parts, where the spectrum shows no spectral lines and therefore reaches the continuum. Due to the high rotational velocity of HD 8801, there are only few parts in the red, where this could be done. As an Echelle spectrograph was used to acquire the spectrum, each spectral order shows a low S/N ratio at its limits and a high S/N ratio at its center. Due to order overlapping, the signal to noise ratio changes rapidly and more or less randomly throughout the observed spectral region. So, a single value cannot be given.

2.4. Radial and projected rotational velocities

2.4.1. Radial velocity

Although the radial velocity is not a crucial parameter in the abundance determination process, it is necessary to shift the spectrum from space- to laboratory wavelengths. This simplifies the identification of the individual spectral lines and allows the usage of automated fitting routines.

Several different methods can be applied. The simplest one is to compare the known laboratory wavelength of a spectral line with its observed wavelength. This can be done easily for slow rotating and therefore narrow lined stars. In the case of HD 8801 the rotational velocity is about 55 km/s, so that only few unblended and well defined symmetrical lines are present for which a central wavelength can be measured. In such cases, the cross correlation method can be useful and provides more accurate results.

Cross correlation method

This method allows to measure the similarity of two curves. The mathematical definition of the correlation coefficient, which is a measure of the similarity, is given by

$$R(d) = \frac{\sum_{wl=1}^n \{ [O(wl) - \bar{O}] [S(wl-d) - \bar{S}] \}}{\sqrt{\sum_{wl=1}^n [O(wl) - \bar{O}]^2} \sqrt{\sum_{wl=1}^n [S(wl-d) - \bar{S}]^2}}$$

Formula 1: Cross correlation coefficient.

Here, $O(wl)$ is the observation, $S(wl)$ the synthesis. The averages are denoted with horizontal lines. d is the wavelength shift according to the radial velocity for which the correlation coefficient should be calculated. Values between data points can be interpolated. Doing this for different radial velocities results in a curve like Figure 26. If both series (observation = synthesis) are the same, R would reach 1 and the profile would be a perfect Gaussian bell function (this is called auto correlation). If a second spectrum is hidden in the observation, which is the case if the observed star is a binary or even a multiple system, the cross correlation profile would deviate from a bell function and, depending on the difference in the radial velocities of the components, show two or more peaks. This is shown in Figure 25 for the star HD 10167.

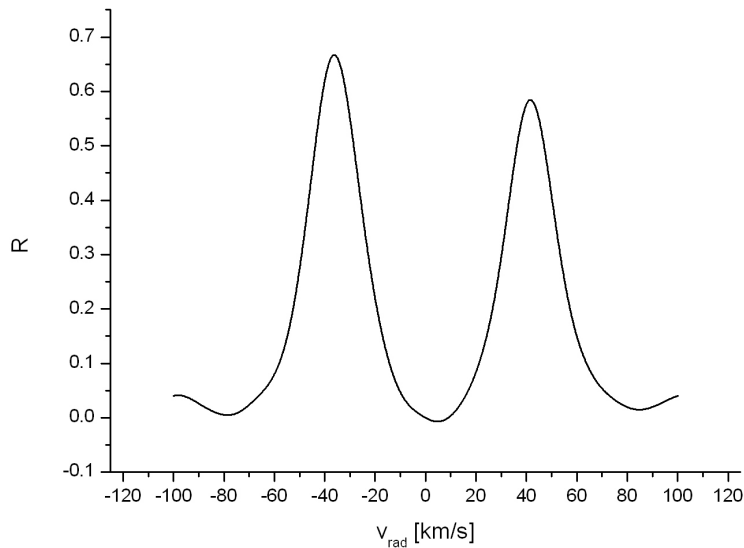


Figure 25: Cross correlation profile for the binary HD 10167.

In order to use this technique, synthetic spectra with an initial guess for the rotational velocity and atmospheric parameters have to be calculated.

Photometrically derived parameters can diverge from spectroscopically determined by a significant amount. Nevertheless, they are sufficient for a starting point for spectral analysis. The starting values for HD 8801 are given in Table 6.

The microturbulence was set to 2 km/s as this is a typical value for stars at this position of the H-R diagram.

T_{eff}	7254 K
$\log g$	4.13 cm/s^2
v_{mic}	2 km/s
Z	0.2

Table 6: Starting values for the first stellar model of HD 8801.

In a next step, an ODF-model was calculated similar to the solar spectrum described in chapter 0. Then, a small part with good continuum normalization and high S/N ratio in the center of the spectrum at 5500 Å was synthesized and plotted together with the observation. The spectrum viewer software *rotate_oleg* allows to fold the synthesis with a rotational broadening profile. A value of 55 km/s gives the best fit and is therefore the initial guess for the rotational velocity.

Now, the whole observed spectral range was synthesized using the initial parameters. For HD 8801, 25 spectral segments were usable where the S/N and the quality of the continuum normalization were sufficient. In order to determine the bandwidth of the radial velocity values, an initial cross correlation was calculated for the segment 5046 – 5199 Å. The result is shown in Figure 26. The radial velocity of the star is the centre of the fitted Gaussian (here -22.3 km/s).

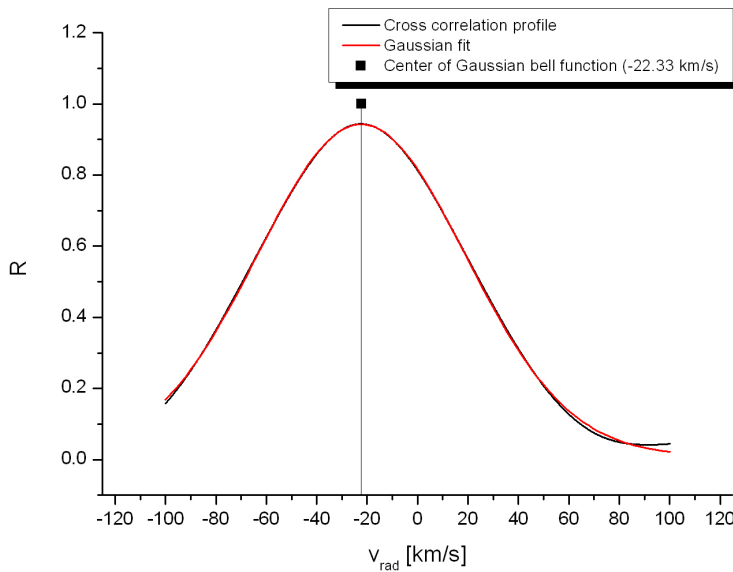


Figure 26: Initial cross correlation profile with fitted Gaussian bell function.

The adjusted R^2 (adjusted coefficient of determination) value for the Gaussian fit is 0.99966 which indicates, that the observation consists of only one spectrum.

The cross correlations for all segments were calculated around this initial radial velocity from -32.3 to -12.3 km/s with a step-width of 0.1 km/s. A Gaussian bell function was fitted to the centers. The results are shown in column v_{rad} in Table 7.

The mathematical errors for the center of the fits (the resulting radial velocity) are at maximum 0.01 km/s and can therefore be neglected.

Spectral segment		v_{rad} [km/s]	R_{max}	#lines(Tab. 9)
from [Å]	to [Å]			
4000	4047	-22.04	0.80	1
4050	4093	-19.57	0.78	1
4148	4196	-24.99	0.76	2
4197	4246	-24.16	0.84	1
4250	4310	-21.74	0.84	1
4367	4405	-23.49	0.86	1
4423	4464	-23.45	0.87	1
4466	4522	-24.53	0.92	4
4524	4581	-22.40	0.82	4
4594	4694	-26.78	0.77	1
4930	5043	-21.12	0.92	1
5046	5199	-22.41	0.94	3
5212	5281	-24.24	0.96	2
5290	5358	-23.34	0.92	3
5375	5435	-21.91	0.96	3
5460	5544	-21.66	0.75	2
5547	5597	-22.18	0.78	2
5638	5703	-24.65	0.55	0
5733	5821	-22.82	0.26	0
6034	6126	-25.12	0.36	2
6142	6234	-22.36	0.46	1
6373	6453	-21.83	0.50	2
6637	6713	-24.00	0.19	0
6744	6846	-21.32	0.13	0
7477	7590	-23.81	0.28	1
8391	8517	-26.39	0.61	0

Table 7: Individual radial velocities for different spectral segments. The columns R_{max} and #lines(Tab. 9) show different weights.

The scatter of the individual values is due to different error sources:

- The rotational velocity is rather high and therefore the width of the cross correlation profile as well. A slight deviation in the symmetry of the profile causes a shift in the center of the fitted Gaussian. The typical width of a medium-strength spectral line of HD 8801 is 2 Å. The error of about 1.6 km/s corresponds to a velocity shift of 0.027 Å at 5000 Å which is 1/75th of a typical line width.
- The resolving power of the spectrograph is around 60 000 at its maximum. This corresponds to an instrument profile with a width of 5 km/s ($R = \delta\lambda/\lambda = \delta v/c \Rightarrow \delta v \approx 5 \text{ km/s}$). The error is therefore lower than the resolution limit of the spectrograph.
- Spectral regions that cannot be fitted well (see the maximum correlation coefficient in Figure 27 and column R_{max} in Table 7) usually show a larger deviation from the average value than regions with a good agreement between observation and synthesis.

- If the quality of the wavelength calibration shows errors due to optical distortions of the spectrograph, these errors directly influence the radial velocity determination.

At this point, it is advisable to use weighted averages. Two different weightings were applied.

- The maximum correlation coefficient (column R_{max} in Table 7, see also Figure 27) can directly be used for weighting as it is a value for the quality of the fit between the observation and the synthesis.
- The number of high quality, unblended lines found in a spectral segment as listed in Table 9 (column $\#lines(Tab.9)$ in Table 7) is a measure for the scientific usability and can therefore be used as weight.

Table 8 shows the resulting weighted averages including weighted errors.

Weight	$\langle v_{rad} \rangle$ [km/s]	$\sigma_{vrad, weighted}$ [km/s]
no weight	-23.2	1.7
R_{max}	-23.1	1.7
$\#lines(Tab. 9)$	-23.1	1.5

Table 8: Average radial velocities and errors.

R_{max} - and $\#lines(Tab.9)$ - weightings both result in the same value for the radial velocity of -23.1 km/s with an average error of 1.6 km/s. The whole spectrum was finally corrected for this velocity shift. The result is a spectrum with a wavelength in the rest frame of the star.

In order to get an astronomically relevant value, the velocity has to be referred to a reference point. Either the local standard of rest (LSR), or the sun. The IRAF Task *rvcorrect* calculates this correction based on the date, time and location of the observation. The values are 1.4 km/s related to the sun and 3.3 km/s relative to the LSR. Wilson (1953) gives a value of 1.3 km/s for HD 8801 relative to the sun.

By-products of the cross correlation technique are the individual maximum values of the cross correlation coefficient R , which are a measure of the similarity between the observation and the synthesis for the different spectral segments (column R_{max} in Table 7). This is shown in Figure 27.

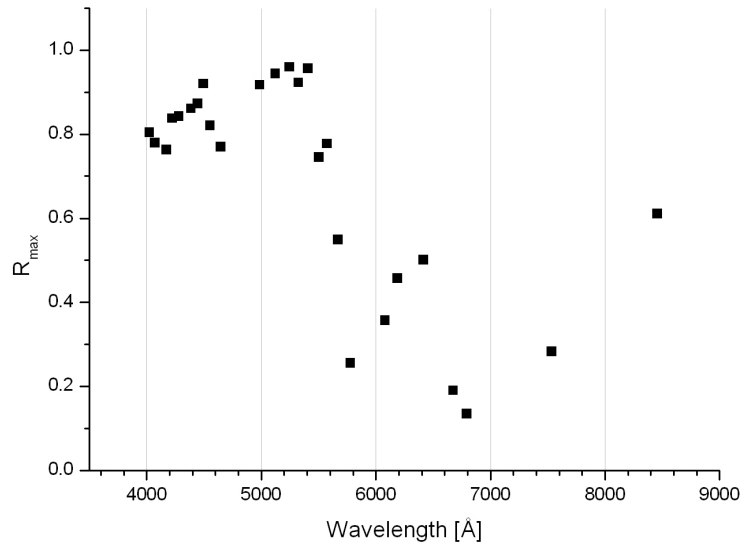


Figure 27: Maximum cross correlation coefficients for different spectral segments.

The rapid decrease from 5600 Å redwards is due to the increase in telluric lines which were not modelled. The decrease to lower wavelengths is due to the increasing number of spectral lines and hence the stronger influence of the wrong abundances. Such a diagram can assist in the process of line selection.

Line fitting method

Throughout the whole spectrum with several thousands of contributing spectral lines, only 40 lines are clean enough to measure their centre with sufficient accuracy. This line selection was done manually by comparing the observation with the synthetic spectra calculated before. The software *rotate_OLEG* was used to semi-automatically find the optimal value for the radial velocity. The already synthesized spectra from the cross correlation method described above, were iteratively shifted and χ^2 was minimized within a manually selected interval around a spectral line.

Doing this for all 40 lines results in a radial velocity of -22.7 ± 1.7 km/s (see Table 9). This result agrees well within the errors with the result of the cross correlation of 23.1 km/s (see Figure 28).

The Analysis

Element	Wavelength [Å]	v_{rad} [km/s]	Quality	$vsini$ [km/s]
Fe I	4005.242	-25.6	continuum bad	
Fe I	4063.594	-24.2	continuum bad	
Ti II	4163.644	-22.9	continuum bad	
Fe I	4191.431	-25.0	continuum bad	
Fe I	4222.213	-20.2	OK	50.4
Fe I	4271.154 and 4271.761	-22.0	OK	48.1
Fe I, Ti II	4367.578 and 4367.652	-21.3	abundance off	
Fe I	4427.298 and 4427.310	-21.7	OK	57.7
Ti II	4501.27	-23.9	abundance off	
Fe II	4508.288	-23.7	OK	50.8
Fe II	4515.339	-21.0	OK	49.9
Fe II	4520.224	-24.9	OK	49.7
Fe II, Ti II	4549.474 and 4549.622	-21.5	OK	55.5
Cr II	4558.65	-19.9	OK	49.3
Ti II	4563.757	-21.4	OK	54.7
Ti II	4571.971	-18.6	OK	48.2
Fe I	4602.941	-24.0	continuum bad	
Fe I	4957.299 and 4957.597	-22.9	OK	54.3
Fe I	5090.774	-21.8	OK	54.8
Fe I	5162.273	-21.4	OK	51.4
Fe I	5191.455 and 4192.344	-21.0	continuum bad	
Ti II, Fe I	5226.538 and 5226.862	-24.1	abundance off	
Fe I, Ca I, Fe I	5269.537, 5270.270 and 5270.356	-25.2	abundance off	
Fe I	5302.302	-24.9	OK	54.4
Fe II	5316.615 and 5316.784	-23.1	OK	52.4
Fe I	5353.374	-22.5	OK	53.3
Fe I	5383.369	-19.7	OK	52.6
Fe I	5400.502	-23.3	OK	54.4
Fe I	5429.697	-21.6	OK	56.1
Fe I	5497.516	-24.9	OK	53.4
Fe II	5534.847	-21.0	OK	49.8
Fe I	5569.618	-22.6	OK	52.5
Fe I	5572.842	-24.7	OK	52.3
Fe I	6065.482	-23.2	OK	54.4
Ca I	6102.723	-25.2	OK	57.7
Fe I	6191.558	-22.8	OK	53.0
Fe I	6393.601	-21.9	OK	56.5
Fe I	6411.649	-22.3	OK	54.1
Ca I	6439.075	-22.4	OK	55.6
Fe I	7495.066	-24.0	OK	56.0

Table 9: Results for v_{rad} and $vsini$ using the software *rotate_OLEG*. Multiple wavelengths indicate blended lines. In this case, the whole spectral feature was fitted.

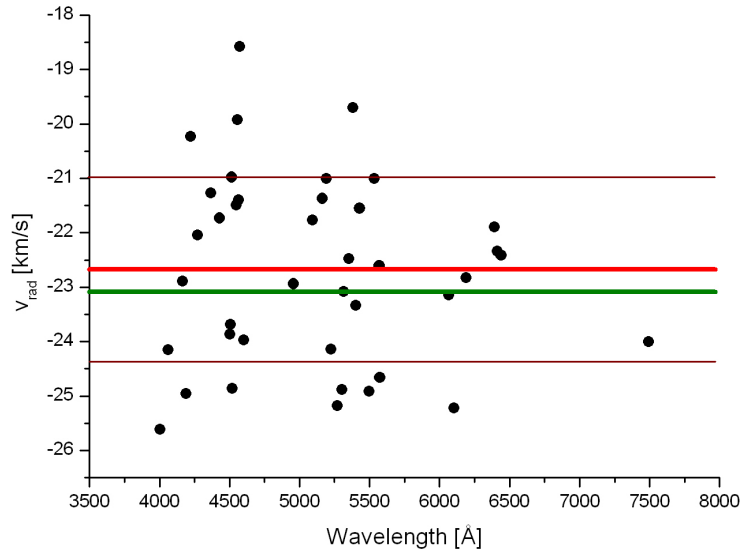


Figure 28: Radial velocities for individual lines derived by line fitting using *rotate_OLEG*. The thick red line marks the average, the thin dark red lines mark the 1σ error. The green line is the cross correlation result.

2.5. Projected rotational velocity

Rotate_OLEG also provides a fitting algorithm for the projected rotational velocity. Therefore a synthetic spectrum with no rotational broadening is required. This spectrum is then folded with a rotation profile until χ^2 is minimized. 30 out of the 40 lines used in the chapter above were suitable for this analysis (see column *Quality* in Table 9). If the continuum fit was too bad or the abundance for the specific line was obviously wrong, the line was skipped. This resulted in a projected rotational velocity of 53.1 ± 2.7 km/s which was used in this analysis.

Another method to determine $v \sin i$ is again using the cross correlation technique. This is done by calculating synthetic spectra with different rotational broadening and cross correlate them with the observation. The maxima of the cross correlation profiles are plotted against the according rotational velocity. Fitting an appropriate function and finding its maximum gives the best fitting rotational velocity. This can be done either for the whole spectrum at once or for spectral segments individually.

For HD 8801 this was done at the end of the analysis, based on the final atmospheric parameters and abundances for the spectral segment with the highest cross correlation coefficient (5375 – 5435 \AA with $R_{\text{max}} = 0.962$). The result is shown in Figure 29.

The velocity of 57 km/s lies slightly above the upper limit of the result obtained with the line fitting method. The maximum cross correlation value is 0.97636. A change of 1 % in this value, results in a velocity change of 6.6 km/s. The maximum is therefore not well defined and a slight error in the cross correlations due to a bad fit can cause a large error in the rotational velocity determination.

So this method should only be used for slower rotating stars, where the cross correlation profiles are narrower and the maxima are better defined.

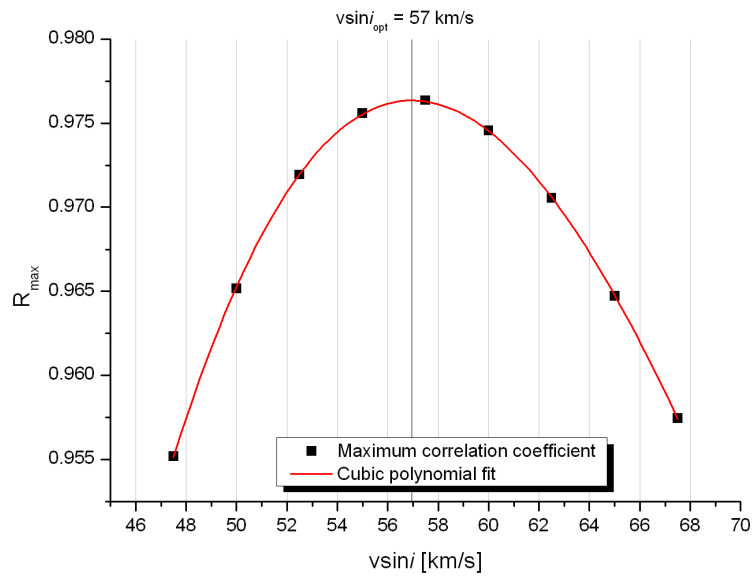


Figure 29: Determination of the projected rotational velocity using the maximum cross correlation coefficients for syntheses with different $v \sin i$. The maximum is marked by the vertical line.

3. The iterative approach

3.1. Principles

As an abundance analysis is a multidimensional optimization problem, two approaches are possible.

- Calculating points in the multidimensional parameter space and finding the optimal solution among them.
- Performing an iteration scheme within the parameter space and close in on the optimal solution step by step.

The parameter space is spanned by four coordinates.

- The effective temperature
- The gravity
- The microturbulence
- The element abundances

The element abundances itself span a multidimensional space of as many dimensions as elements. That makes it nearly impossible to calculate a parameter grid in advance.

The iterative approach

The only feasible solution is an iteration scheme. Such a scheme is shown in Figure 30 and described below.

First column:

The determination of the fundamental parameters is followed by an abundance determination. The results are then again used as an input for the next parameter determination and so on. This is done until convergence or in other words, until no significant change between two iteration steps is found. Parameters derived from photometry mark the starting point.

Second column:

Each abundance determination step is a sequence of individual element abundance determinations. Each result is used as an input for the next element in the sequence. In principle, this process also has to be continued until convergence, but as the abundance determination process itself is repeated and due to the huge amount of calculation time the achievement of convergence would consume, this can and has to be skipped.

Third column:

The fundamental parameter determination itself follows an iteration scheme in which the result of one step, e.g. the determined gravity, is the basis for the determination of the next parameter, e.g. the effective temperature. This is continued until convergence.

Fourth column:

Each parameter itself can be based on multiple elements so that a reliable average can be used for the next step. This depends on the number of useable lines. In the beginning, only iron was used in this analysis. Other elements entered the process in the refining step.

The iterative approach

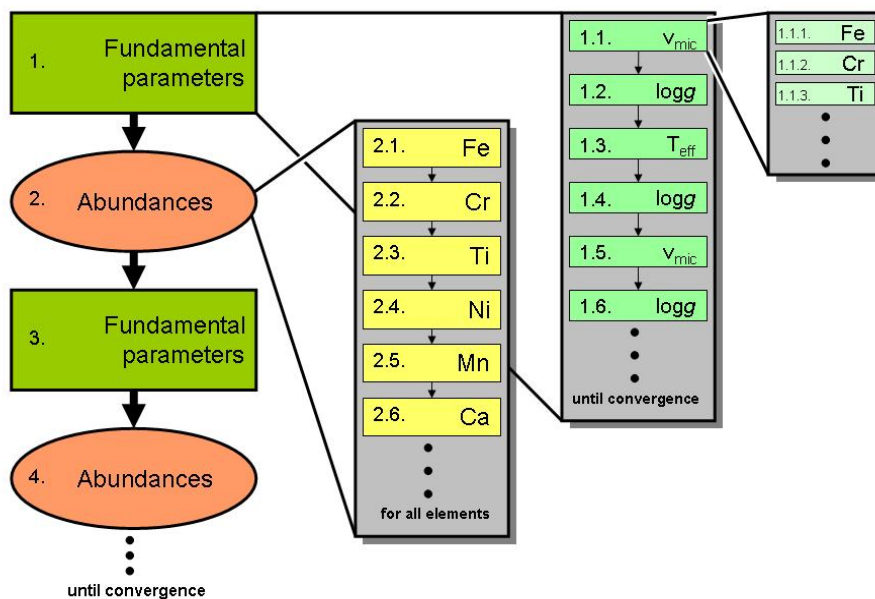


Figure 30: The iterative approach as used in this analysis

Strömgren photometry usually provides parameters with sufficient accuracy in order to start the process. Due to the fact, that the effective temperature determination from photometry is based on the flux distribution, the value can be quite different from the spectroscopically determined one, especially for Am stars as mentioned in the introduction. Therefore additionally, the hydrogen lines can be used as spectroscopic temperature indicators.

Figure 31 shows the observed hydrogen line together with three synthetic spectra for different effective temperatures (ODF-models with $\log g = 4.13 \text{ cm/s}^2$, $v_{\text{mic}} = 2 \text{ km/s}$, $Z = 0.2$). This indicates that the assumed temperature of 7250 K derived from photometry is probably too high by 200 K.

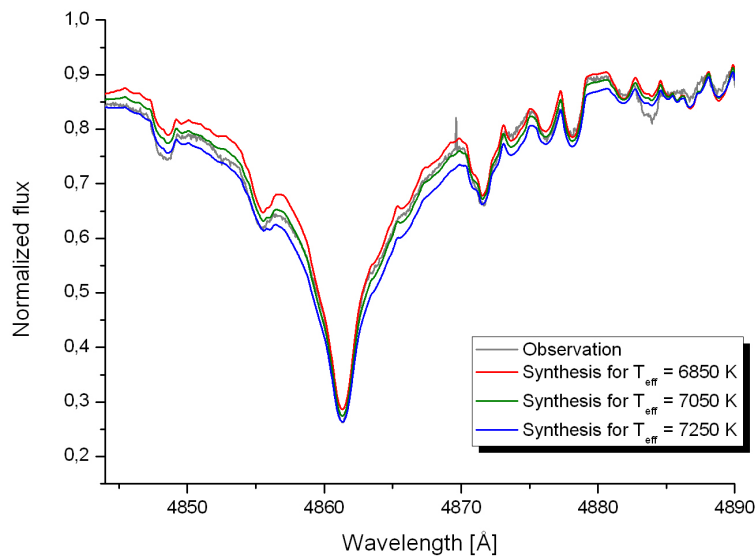


Figure 31: Observation and syntheses around H β for different effective temperatures (6850 K, 7050 K and 7250 K).

This is surprising, as for Am stars the photometrical temperature is typically lower than the spectroscopically derived.

H α gives the same result as H β with high accuracy (Figure 32).

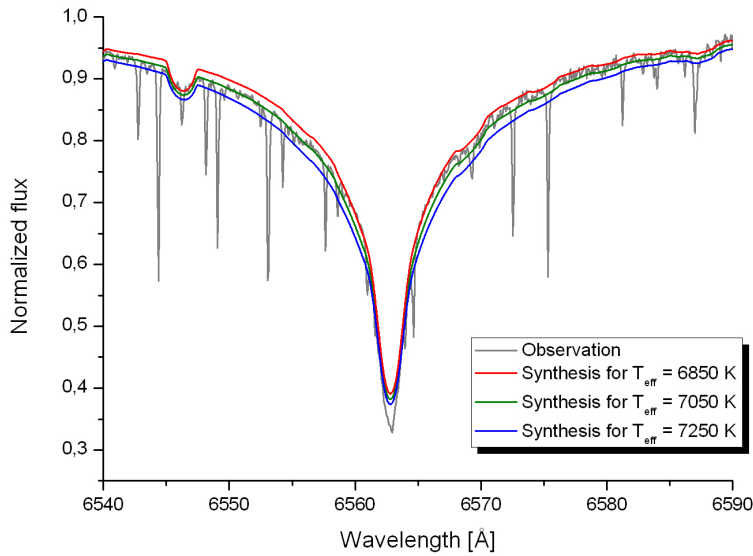


Figure 32: Observation and syntheses around H α for different effective temperatures (6850 K, 7050 K and 7250 K).

In order to confirm this result, the polarimetric observations, taken at the OHP observatory to scan for the existence of a magnetic field were used, as they also cover the H α line (Figure 33). The spectrum was reduced automatically so that a mistake in the continuum normalization process applied to the McDonald observations as described above can be ruled out to be the reason for the low temperature derived from the hydrogen lines.

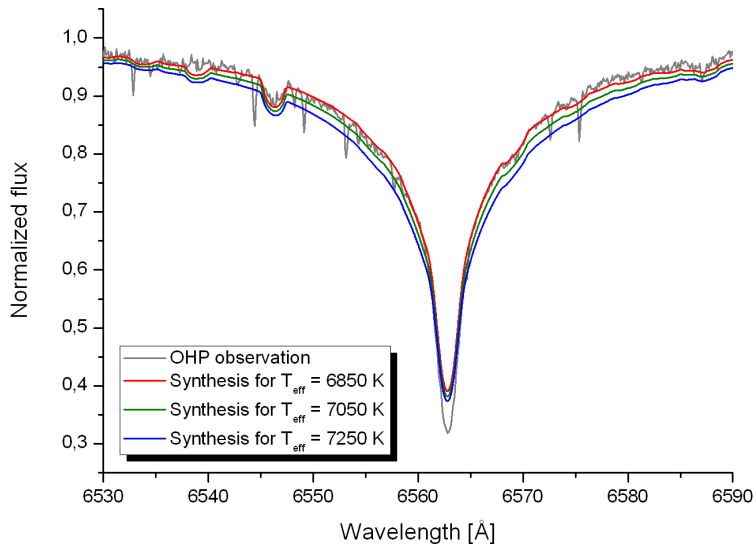


Figure 33: OHP Observation and syntheses around H α for different effective temperatures (6850 K, 7050 K and 7250 K).

The OHP observations suggest a temperature between 6850 and 7050 K which confirms the results obtained from the McDonald observations. Nevertheless, the photometrically derived value of 7250 K was kept as a starting point.

3.2. The fundamental parameter iteration scheme

During the determination process it is unavoidable to check and refine the atmospheric parameters of the star. As mentioned above, photometrically determined atmospheric parameters can differ from spectroscopically determined. This is not surprising, as Strömgren photometry only uses 4 measured values whereas spectroscopy usually uses several thousand.

The whole problem of selecting the “correct” atmospheric parameters for a star consists mainly of finding three linked values: the effective temperature (T_{eff}), the gravity ($\log g$) and the microturbulence (v_{mic}). Turning one wheel, turns the others as well. Nonetheless, each parameter has its specific behaviour.

The basis of the determination method is the curve of growth (COG) method which was used in early years to determine these parameters. Nowadays it is possible to use a statistical approach based on the COG. The measurement of several spectral lines and the analysis of different dependencies give hints to the correct solution. There are some assumptions made in order to be able to disentangle the parameters. One is, that all lines are formed at one depth in the stellar atmosphere. No stratification is present and the line formation layer is infinite thin. This restricts the method to hotter stars. Another one is LTE (local thermal equilibrium). The used dependencies are described in the following sections and a detailed discussion can be found in Gray (1992).

Due to the fact, that microturbulence shows the most significant behaviour and is therefore the “easiest” parameter to determine, it is a good starting point for the iterative process. Models with different microturbulence velocities are calculated and the optimal solution is derived. Temperature, gravity and metallicity are taken from photometry.

In the next step, the optimal gravity is determined based on the new microturbulence, as this is, after microturbulence, the least difficult parameter.

At last, the effective temperature is identified. This is usually the most difficult parameter and in many cases, the photometrical value or the temperature derived from hydrogen line fitting has to be kept.

Now, there are two different ways to continue: either the process is continued with another microturbulence determination or a gravity determination. In this analysis, the second sequence was used (second scheme, see below). Each step is described in detail in the chapters 3.2.4 through 3.2.11 below.

This is done until convergence which means, that no significant changes occur between two iteration steps. Significant means “within the typical errors”. In case of a completely wrong initial guess, the process could lead to a “wrong” solution. It is possible, that many different points of convergence exist in the parameter space. One possibility to distinguish between wrong and right is the abundance scatter within the used line sample. Such a case is shown in the last iteration step for the effective temperature below. Usually this doesn’t happen in the case of existing Strömgren photometry and a non-peculiar star as the initial parameters are typically accurate enough and lie close to the final solution.

- $v_{\text{mic}} - \log g - T_{\text{eff}} - v_{\text{mic}} - \log g - T_{\text{eff}} - v_{\text{mic}} - \log g \dots$
- $v_{\text{mic}} - \log g - T_{\text{eff}} - \log g - v_{\text{mic}} - \log g - T_{\text{eff}} - \log g \dots$ (used in this analysis)

3.2.1. Element selection

Usually, iron is used to determine the fundamental parameters but in case of a normal (solar type), slow rotating star, chromium, titanium, nickel or manganese can be used additionally. Each element will give its own value for microturbulence, gravity and effective temperature. This allows to estimate errors in the determination of the parameter.

In case of a more peculiar object, the element with the best known atomic parameters and most observable, unblended lines has to be used and this typically is iron.

In this analysis, both methods were used. For the initial determination, only iron lines were used. For the refining process, chromium, titanium and nickel were added.

This is reasonable, as in the beginning, the blending effect in fast rotating stars links up all abundances. It is unproblematic in stars with a solar scaled abundance pattern, but can lead to nondistinctive results in peculiar objects.

3.2.2. Line selection

In order to get information about any stellar parameters it is necessary to measure or fit quantities of individual spectral lines with known atomic parameters. As HD 8801 shows an enormous amount of such lines and rotates rapidly, most of the spectral lines overlap. This prevents one from measuring equivalent widths for a sufficient number of lines. Only 25 completely unblended lines (see Table 9) were found throughout the whole observed wavelength range. This is not sufficient for a competent knowledge of the stellar parameters.

In such cases it is possible to fit the observed spectrum with a synthetic one. This is done by modifying the element abundance of the stellar model and synthesis until the synthetic spectral line fits the observed one. Doing this for as many lines as possible allows one to find the appropriate atmospheric parameters for a star.

Prior to the fitting procedure it is unavoidable to carefully select the lines (or spectral features) that should be fitted. They should not be blended too much by lines with unknown abundances, the continuum should be normalized well, no atmospheric lines should be present, the S/N ratio should be high enough etc.. 90 Fe I and 22 Fe II lines matched these requirements in the range from 4000 – 7500 Å. In order to have a homogeneous and sufficiently large sample, iron lines were used to determine the fundamental parameters at the beginning. All other elements show less usable lines.

3.2.3. The line fitting process

C. Stütz developed a software package called *ATC* which implements a line fitting procedure. This fitting procedure was used to automatically fit the selected spectral lines as an individual manual fitting of all lines would take several days for one synthesis. The algorithm first selects all contributing spectral lines from the *VALD* database based on the stellar model around the line under consideration within a specified wavelength interval. In the next step, the RMS error is calculated and the element abundance is optimized until the abundance change between two iterations is below 0.1 dex. This is done for all lines individually.

Selecting the fitting width

The width of the interval around a spectral line used to calculate the RMS error is in two points crucial for the result.

First, the selection of lines contributing to the spectrum at the position of the spectral line under investigation has to be as complete as possible. Due to the fact that HD 8801 shows a rather fast rotation, the interval has to be larger than in slower rotating stars.

Second, the fitting width should not be too large to avoid fitting neighbouring lines of the same element which are possibly not useable due to wrong atomic parameters, bad continuum normalization etc..

Therefore, the average abundance and abundance errors for the iron line sample used in this analysis were investigated for different fitting intervals between 0.25 and 4.5 Å. The result is shown in Figure 34. As can be seen, using a fitting width of 2 Å is sufficient for this star. Using a larger interval only increases computation time.

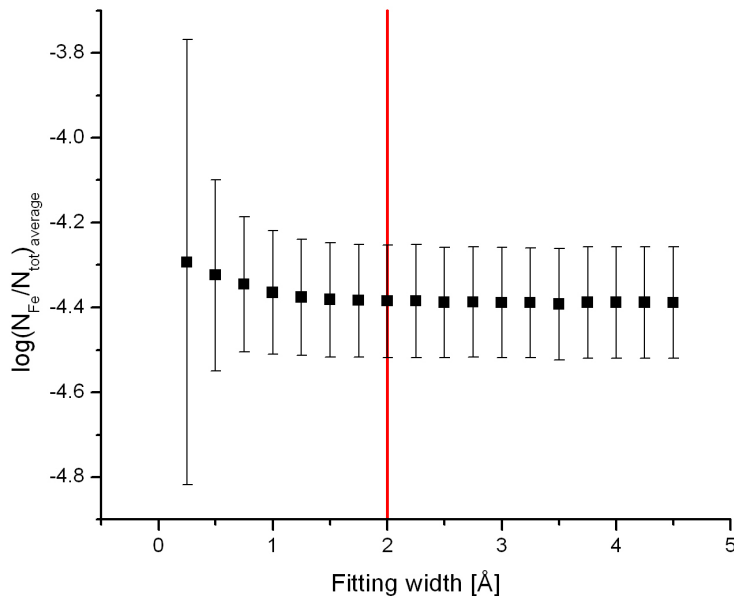


Figure 34: Average iron abundance for different fitting widths.

3.2.4. Step 1 - First microturbulence determination

Microturbulence is still one of the less understood parameters in the process of spectral analysis. It is still more or less a so called “fudge parameter” which is probably linked to turbulence in the stellar atmosphere. Microturbulence simply adds an additional isotropic velocity term in the calculation of the radiation transfer.

The observational evidence for the existence of a microturbulence velocity is the fact, that without microturbulence it is impossible to fit strong and weak lines of the same element with a single abundance. Using this fact allows the determination of the value. Strong lines, that mean lines with a large absorption and therefore a large equivalent width, would give a different abundance than weak lines with a small equivalent width. In the case of HD 8801, equivalent widths cannot be measured but the fact, that the central line depth is proportional to the equivalent width can be used.

Calculating element abundances for all 112 Fe I and Fe II lines and plotting these abundances versus their individual central line depth, result in diagrams like Figure 35 and Figure 36. It can be clearly seen, that the slope of the linear fit changes significantly with microturbulence.

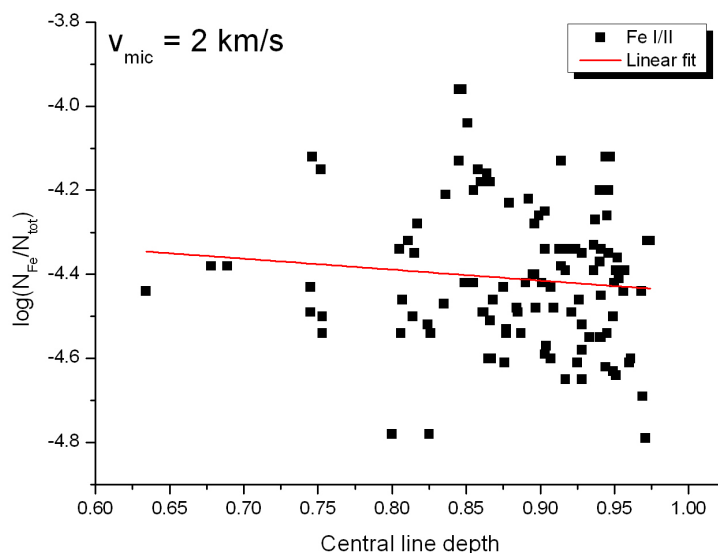


Figure 35: Individual iron line abundances for a model with $v_{\text{mic}} = 2 \text{ km/s}$.

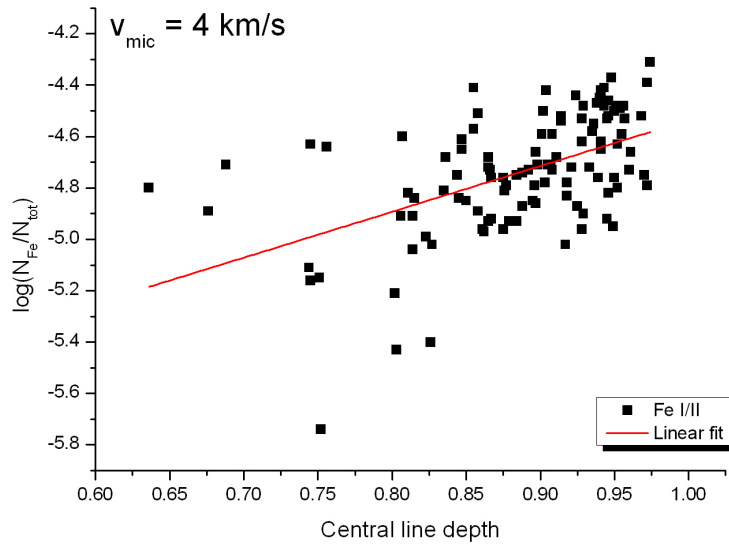


Figure 36: Individual iron line abundances for a model with $v_{\text{mic}} = 4 \text{ km/s}$.

Calculating slopes of linear fits as shown in Figure 35 and Figure 36 for different microturbulence velocities, results in Figure 37. T_{eff} , $\log g$ and Z were taken from photometry.

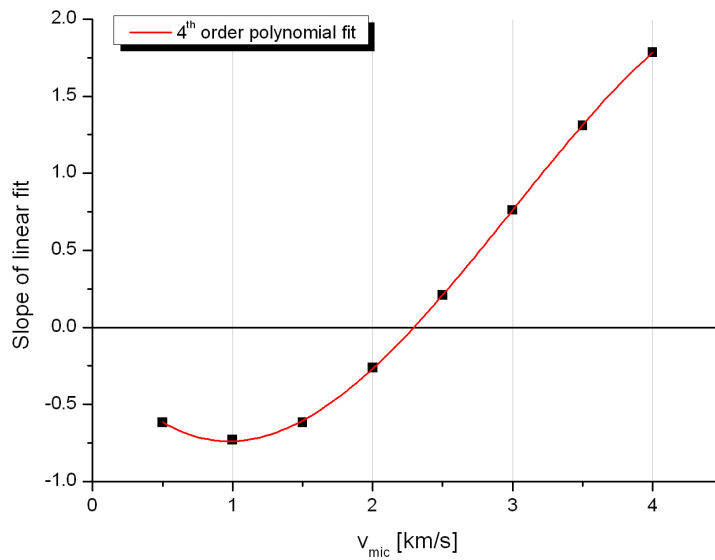


Figure 37: Slopes of linear fits vs. microturbulence velocity for 112 Fe I/II lines.

A 4th order polynomial fit was applied. The zero of this fit gives the optimal microturbulence of 2.29 km/s.

Another indicator is the abundance scatter as it also increases as a trend becomes visible. Plotting these errors against microturbulence, results in Figure 38.

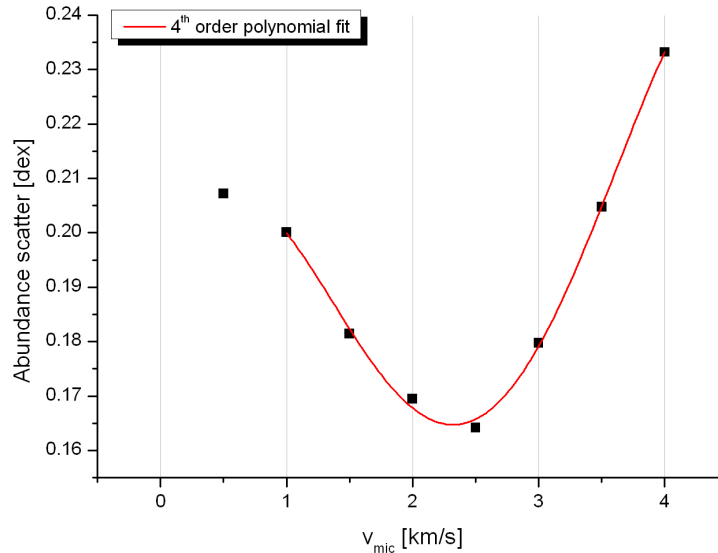


Figure 38: Abundance scatter vs. microturbulence velocity for 112 Fe I/II lines.

The minimum of the polynomial fit suggests a microturbulence of 2.32 km/s.

Both methods result in nearly the same value. So the new microturbulence used for the next iteration step was set to 2.31 km/s. A new stellar model with this value was then calculated.

3.2.5. Step 2 - First gravity determination

Gravity influences the pressure in the stellar atmosphere and this furthermore has influence on the ionization equilibrium through the Saha equation via the electron pressure. In case of the correct value for the surface gravity, it should be possible to model all lines of a specific element independent of their ionization stage with one abundance value. If the average abundance for one ionization stage differs from the value for lines of the same element but from another ionization stage, then the surface gravity cannot be correct.

The model, calculated with the new value for microturbulence was used as a starting point. Figure 39 shows the slopes for Fe I and Fe II lines separately. The average abundance determined from neutral iron lines does not match the abundance determined from single ionized lines. The difference amounts to 0.21 dex. This indicates a wrong gravity assumption.

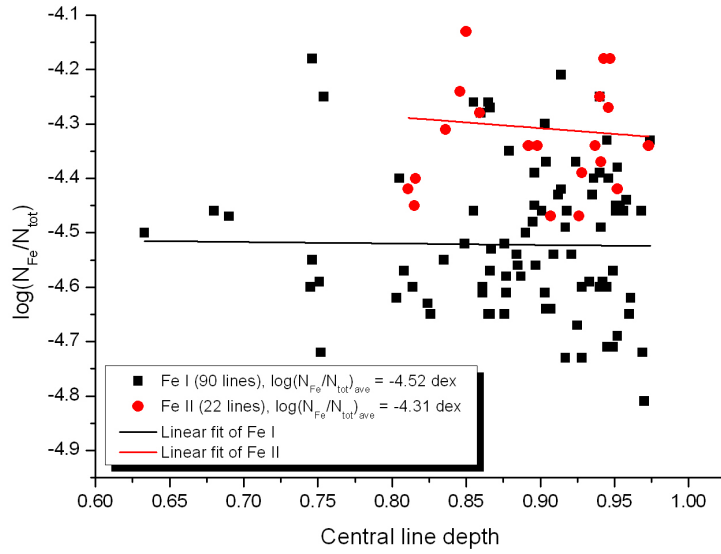


Figure 39: Individual line abundances of Fe I and Fe II lines vs. central line depth. The slopes of the linear fits are close to zero which indicates a correct microturbulence but the average abundances do not match.

Calculating average abundances for neutral and single ionized iron for stellar models with different gravities allowed to find the correct solution. The results are shown in Figure 40 and Figure 41.

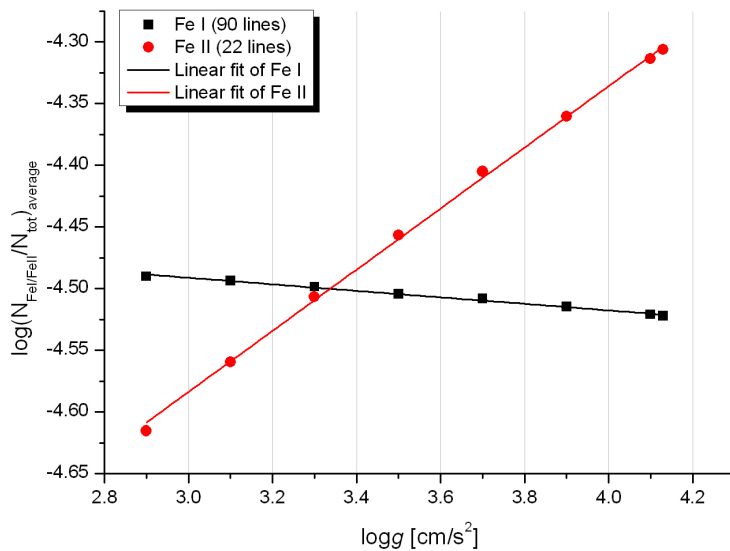


Figure 40: Average abundances for Fe I and Fe II separately for models with different gravities.

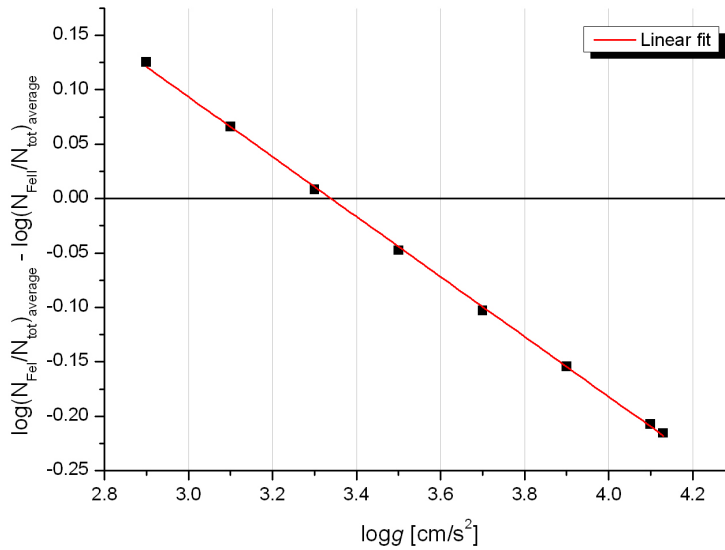


Figure 41: Abundance differences for models with different gravities.

Finding zero of the linear fit in Figure 41 results in a gravity of 3.34 cm/s² which was used for the next calculation step.

3.2.6. Step 3 - First effective temperature determination

Lines with different excitation potential should give the same abundance in case of a correct effective temperature. This fact is used to determine the correct temperature. Figure 42 shows a plot of the individual line abundances versus their excitation potentials for the initial temperature of 7250 K with the new microturbulence and gravity. A trend can be seen which indicates, that the assumed effective temperature is not correct. Models with different temperature were calculated and the slopes of the linear fits in the abundance-versus-excitation potential plots determined. The result is shown in Figure 43.

The determination of the effective temperature is usually difficult and sometimes spectroscopy cannot give better results than photometry. This is on one hand due to the definition of this parameter and on the other hand, its strong dependency on the quality of the excitation potential determination. A star simply doesn't have "a" temperature and the line forming region is not infinitely thin. Therefore lines originate from layers with different temperatures. This generates a natural variance. On the other hand, the values for the excitation potentials of the spectral lines are sometimes not correct and add an additional error in the temperature. Nonetheless, it can be seen from the diagrams below that the effective temperature of 7250 K is too low. 7600 K fit the observations better. This is a typical outcome of an analysis of an Am star. Due to the stronger metallic lines, the absorption is different than assumed in the photometric calibrations.

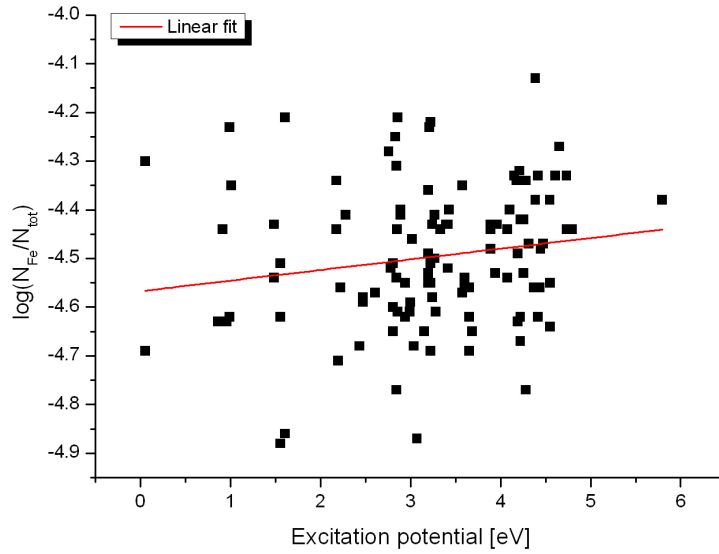


Figure 42: Individual line abundances for Fe I/II lines vs. excitation potential.

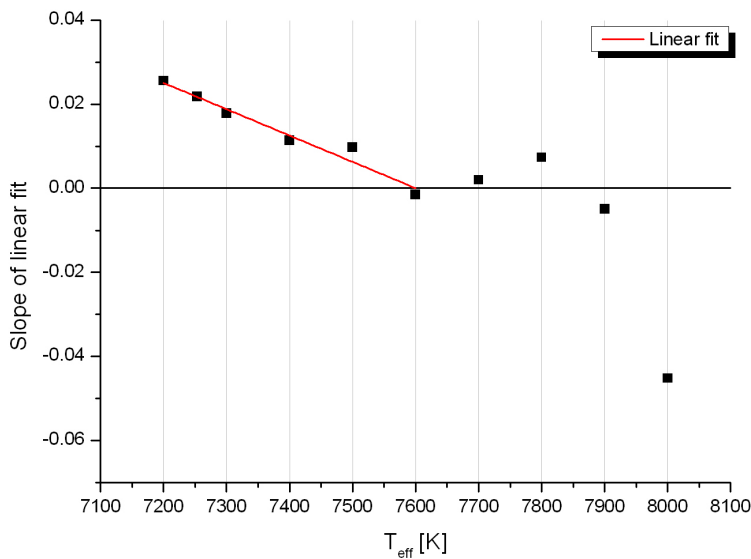


Figure 43: Slope of linear fits to Fe I/II vs. excitation potentials.

Two zeros can be found from Figure 43 (near 7600 K and around 7850 K). In order to identify the correct temperature, a look at the slope errors (see Figure 44) can be helpful. The error is smallest between 7250 and 7600 K so that the solution with a temperature of 7850 K is unlikely. Therefore the solution with the lower temperature was regarded as the correct one and was used in the next steps. Figure 45 shows a plot where line abundances for chromium are plotted against their excitation potentials. Due to the fact, that there are no lines with an excitation potential between 1 and 3 eV, a reliable fit cannot be applied to chromium. The same applies to the other elements so that only iron could be used to determine the effective temperature reliably.

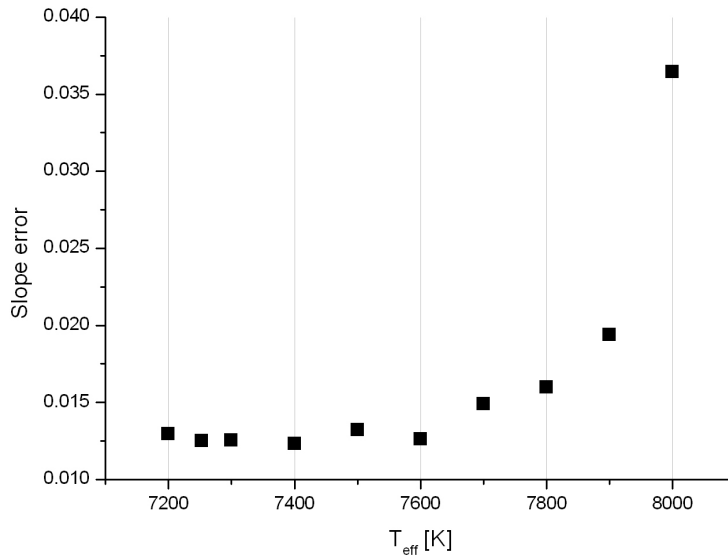


Figure 44: Slope errors versus effective temperature.

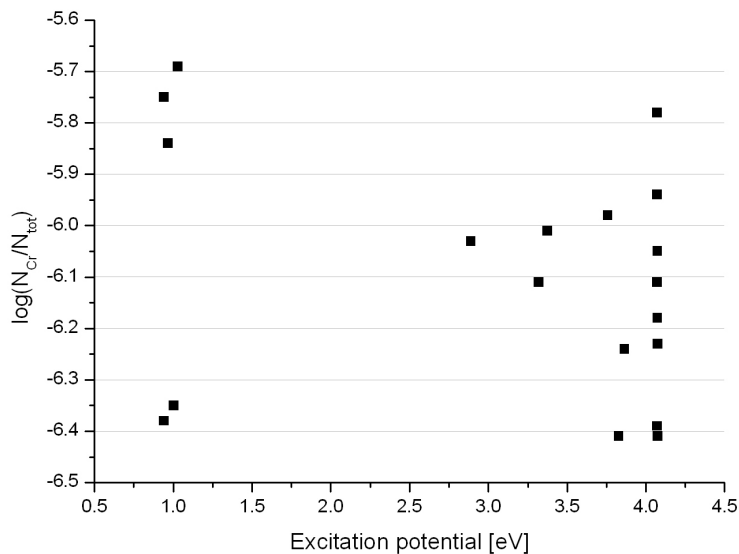


Figure 45: Individual line abundances of Cr I/II lines vs. excitation potential.

As mentioned above, this method not always leads to a solution and Figure 42 already shows one of the problems. The scatter is rather large and the errors for the calculated slopes are large as well (see Figure 44).

In such cases, the temperature could also be checked by fitting hydrogen profiles. Unfortunately this is not possible in the case of HD 8801 as the hydrogen lines show an unusual behaviour for which the reason is unknown.

Other elements than iron could be used as well but in faster rotating stars, the blending typically generates errors too large to be accepted in this initial phase and many elements do not have enough measurable lines with different excitation potentials.

3.2.7. Step 4 - Refining the gravity

A look at the average Fe I and II abundances showed that a correction of the gravity was necessary. Calculating average abundances for models with different gravities resulted in Figure 46.

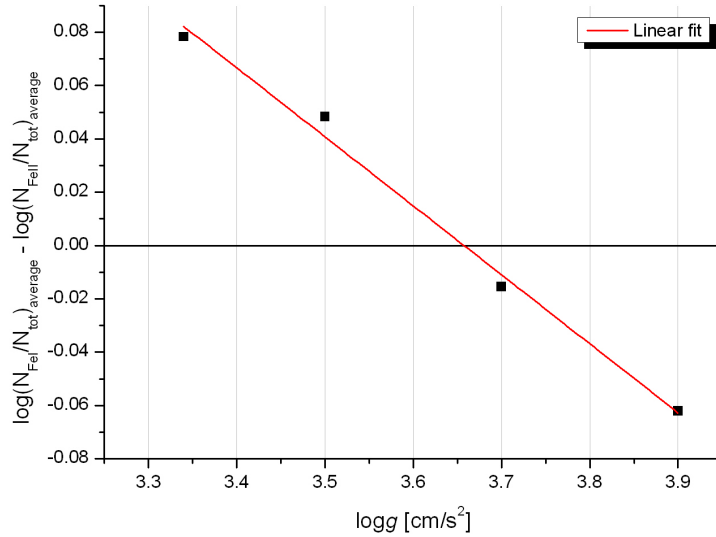


Figure 46: Abundance differences for models with different gravities.

The zero of the linear fit results in a refined gravity of 3.66 cm/s².

3.2.8. Step 5 - Refining the microturbulence

The changed gravity now again produced a trend in the plot abundances-versus-central line depths (see Figure 47) and therefore needed further adjustment.

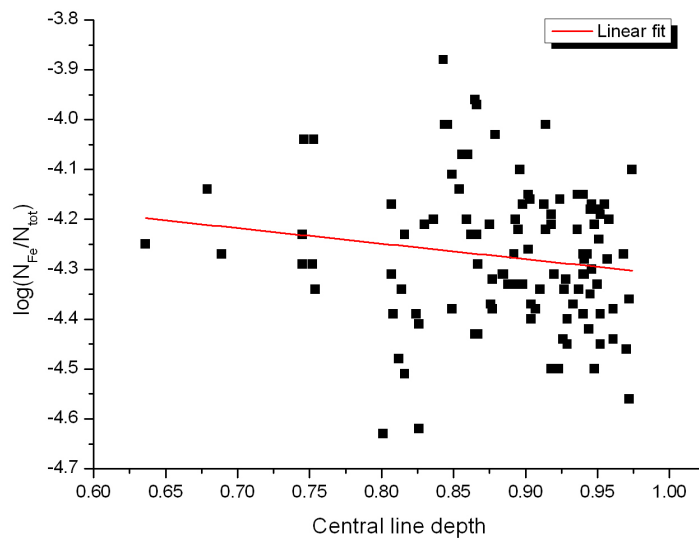


Figure 47: Individual line abundances of Fe I/II lines vs. central line depth.

Figure 48 shows the slopes for models with different microturbulence velocities. Due to the smaller stepwidth in v_{mic} , a linear fit was sufficient.

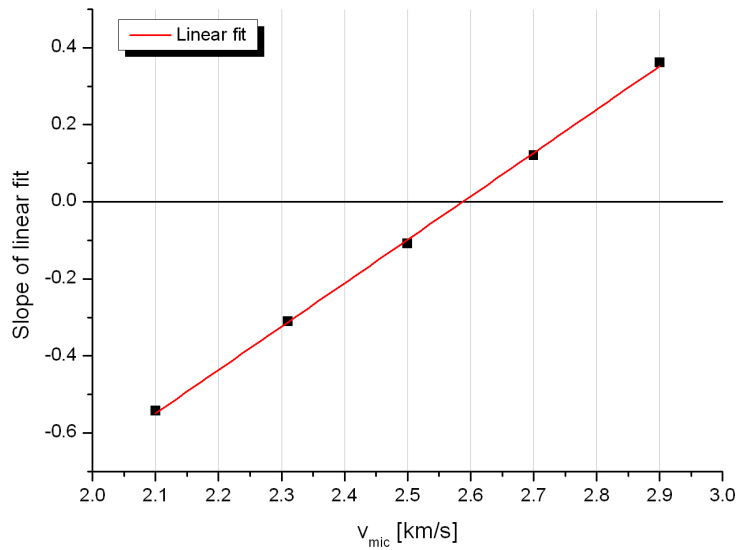


Figure 48: Slopes of linear fits vs. microturbulence velocity for 112 Fe I/II lines.

Finding the zero of the linear fit leads to a new microturbulence of 2.59 km/s.

3.2.9. Step 6 - Refining the gravity

Again, gravity needed to be adjusted slightly and the result is shown in Figure 49. The new value was 3.74 cm/s^2 .

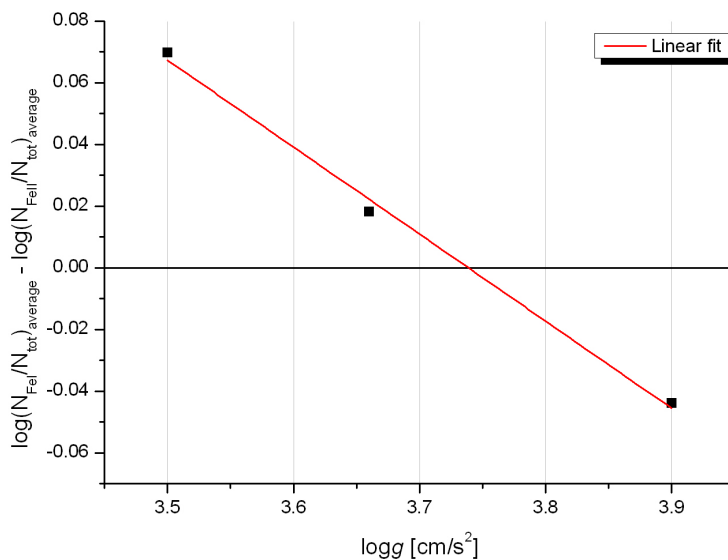


Figure 49: Abundance differences for models with different gravities.

3.2.10. Step 7 - Refining the effective temperature

A last adjustment to the effective temperature was made and resulted in a final value of 7540 K (see Figure 50).

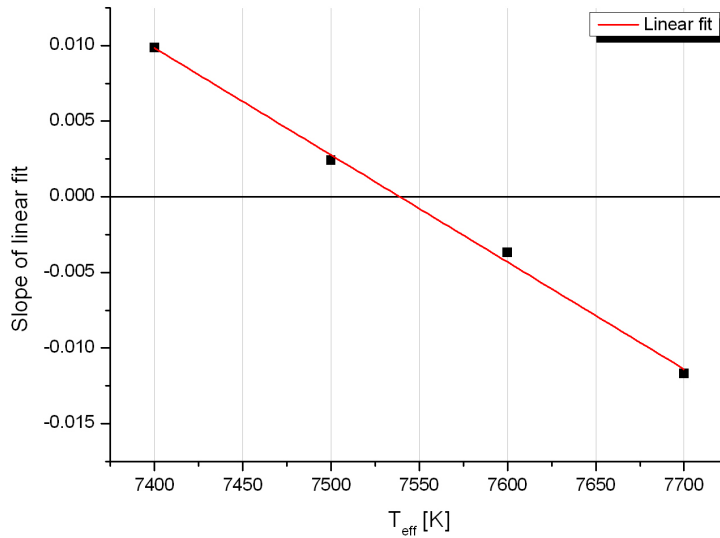


Figure 50: Slope of linear fits vs. effective temperature.

3.2.11. Step 8 - Refining the gravity

With the final temperature, a last check of the gravity was made (see Figure 51).

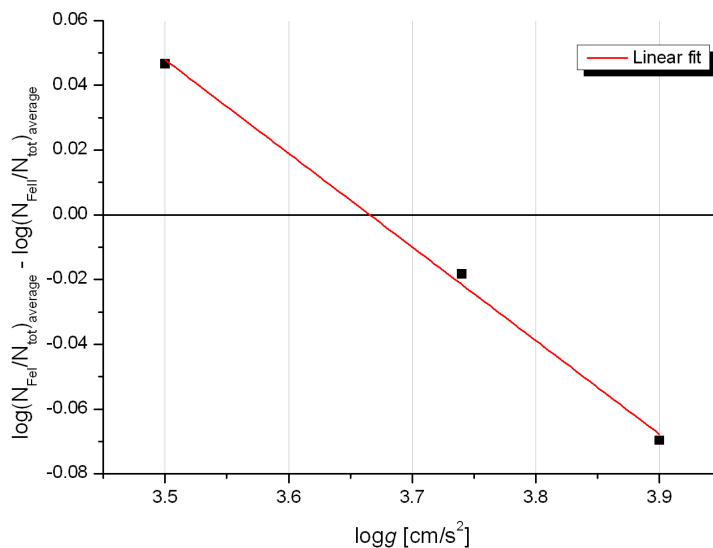


Figure 51: Abundance differences for models with different gravities.

The gravity converged to 3.67 cm/s^2 . The very small abundance-versus-line depths slopes showed that no further adjustment of the microturbulence was necessary.

3.3. Element abundances

Now, that the atmospheric parameters were initially fixed, it was possible to determine the abundances for all other elements.

The initial part is the most crucial: the line selection. “How many lines should be used?”, “How strong should they be?”, etc.

In the case of HD 8801, it is not useful to select lines with a central line depth of less than 0.01 as the errors in the continuum normalization exceed that value. Additionally, extremely weak lines will not be visible as the high $v_{\text{sin}i}$ works as a strong smoothing filter.

3.3.1. Line selection for abundance determination

The line selection process was done in two steps. First, all existing transitions in the observed wavelength range were extracted from the *VALD* database using the extraction tool *Preselect*. Second, based on an initial stellar model, those lines were extracted, that absorb a certain amount of radiation from the continuum using the tool *Select*. Some elements have several thousand transitions in a given spectral range (e.g. Fe, see Figure 52 and Figure 53), others have none. The more the line absorbs, the better it can be fitted, as the S/N ratio becomes less important. The stronger a line, the better the atomic parameters are usually known. This leads to the conclusion for the abundance determination (not for the determination of the fundamental parameters! For microturbulence, weak lines are necessary!), that using strong lines should give better results.

A limit to the number of lines is more or less a technical one: the computation time. Fitting 5 lines manually takes as long as fitting 100 lines automatically. In the case of HD 8801, a semi-automatic routine was used and the calculation time for 100 lines is about 20 minutes at a 4 processor computer.

In order to limit the number of spectral lines, only lines that have a central line depth larger than a specified fraction of the continuum can be selected. A limit of 0.2 means, that the center of the line has to be at a normalized flux of 0.8 or below (1 marks the continuum level). Weaker lines are ignored.

For iron, setting this limit to 0.1 would result in the selection of about 2000 lines as can be read from Figure 53. As iron was used to find the fundamental parameters and the lines have already been selected carefully by hand, no further selection was made. For barium, even a limit of 0.01 only returned 4 lines that could be used, but due to the overabundance of this element, these lines could be fitted well. The column *central line depth limit* in Table 10 shows the individual limits and the effect of this limit on the number of the selected lines for all analysed elements.

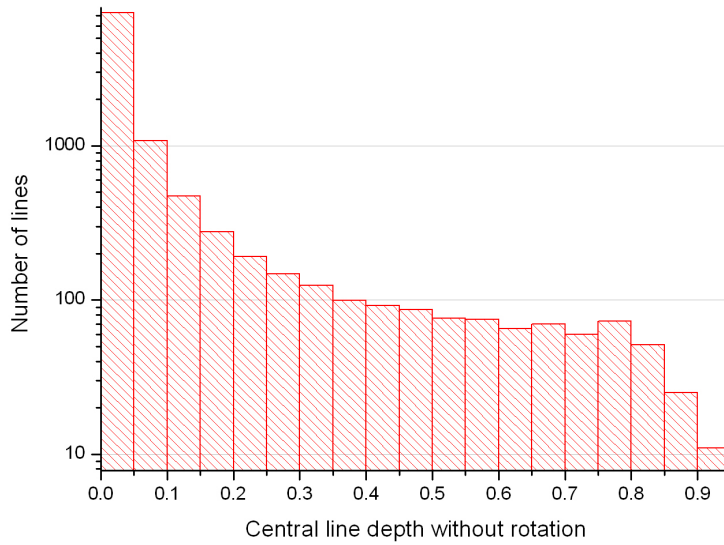


Figure 52: Number of iron lines with a central line depth within a given interval.

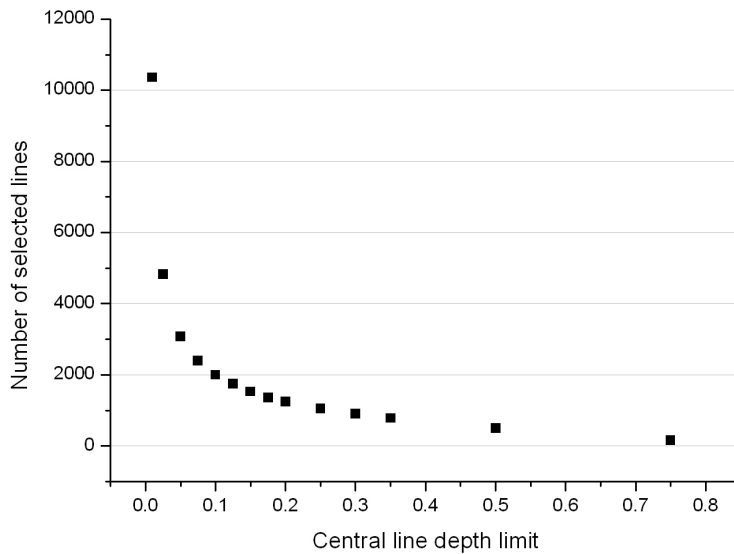


Figure 53: Number of iron lines with a central line depth above a certain limit.

Finally, the following procedure was applied to all elements in order to use only “good” lines:

1. All lines with a central line depth above a certain limit between 4000 and 7500 Å were selected. For elements that showed more lines, 0.1 was used as the limit. For elements with fewer lines, 0.025 or even 0.01 was used and the wavelength range was extended to the whole observation. These are subjective values and were derived by trial-and-error. If too few lines were selected, the continuum limit was lowered and the wavelength range extended.
 2. Lines where no spectrum was observed (due to gaps between the Echelle orders) were rejected.
-

3. The semi-automatic procedure *linfit* from the ATC package was used to fit these lines.
4. Lines with an RMS error of > 1 were rejected. This removed the worst fitted lines. Figure 54 shows the effects of this limit on the line selection of neodymium.
5. Lines around hydrogen lines were rejected.
6. The standard deviation of the remaining sample was calculated and all lines with abundances more the 3σ deviation were rejected (see also Figure 54).
7. A histogram with appropriate bin width was created. The bin width was more or less subjective and depended on the number of useable lines (typically 0.1 to 0.4 dex per bin). This allowed to check the shape of the distribution and the applied χ^2 -minimization algorithm in the fitting process resulted in a more reliable center finding in cases with non-Gaussian distributions.
8. A Gaussian bell function was fitted to the histogram. The center and width are the average abundance and its error. Figure 56 and Figure 57 exemplarily show the histogram and fitted Gaussian bell function for Fe I.

For elements with only few lines, a manual check was done. The final fit was compared to the observation and in case of a “bad” fit, the line was rejected. Figure 55 shows the effect of this manual check for neodymium.

Figure 55 demonstrates another effect: Increasing the number of lines also increases the scatter in abundance. The error estimation in abundance analysis is always a tricky task. The errors in the atomic parameters are typically unknown. Therefore, using a normal error propagation approach is impossible and the only scientific way to get an idea of the size of the error bars is to use the scatter of the individual line abundances as indicators. Here Figure 55 comes into play: the less restrictive the line selection, the larger the scatter. Using only a few “good” lines typically results in smaller error bars. But the definition of “good” mainly depends on the experience of the scientist. If a specific spectral line can be fitted well in stars with different atmospheric configurations, the atomic parameters and opacity calculations obviously reproduce the observations well. One big problem is the absence of a central database for this knowledge and the information can only be acquired through personal communication.

The iterative approach

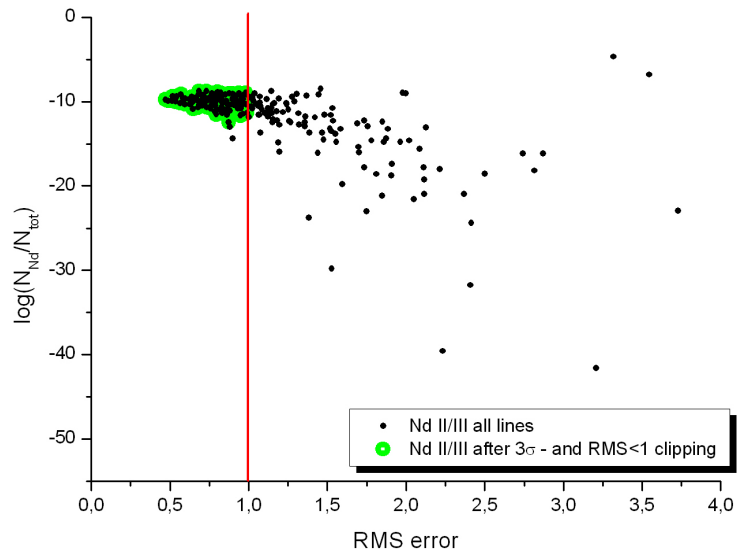


Figure 54: Individual line abundances vs. RMS error for Nd II and III lines. The red line marks the RMS < 1 limit.

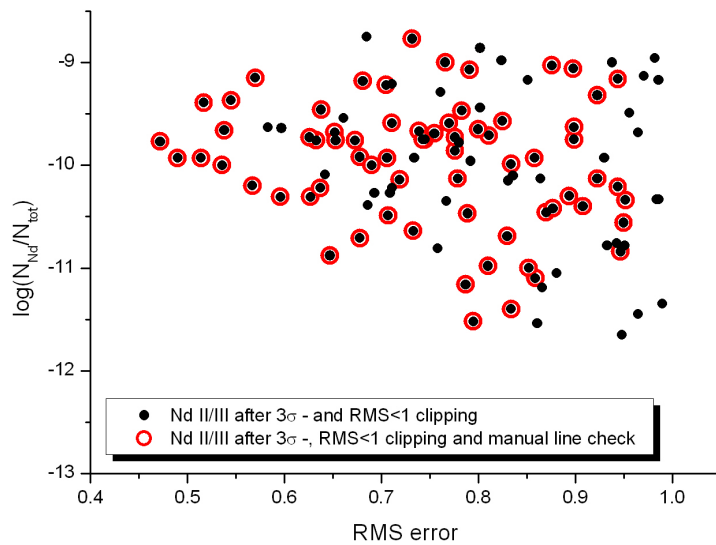


Figure 55: Nd II/III lines before and after manual line selection.

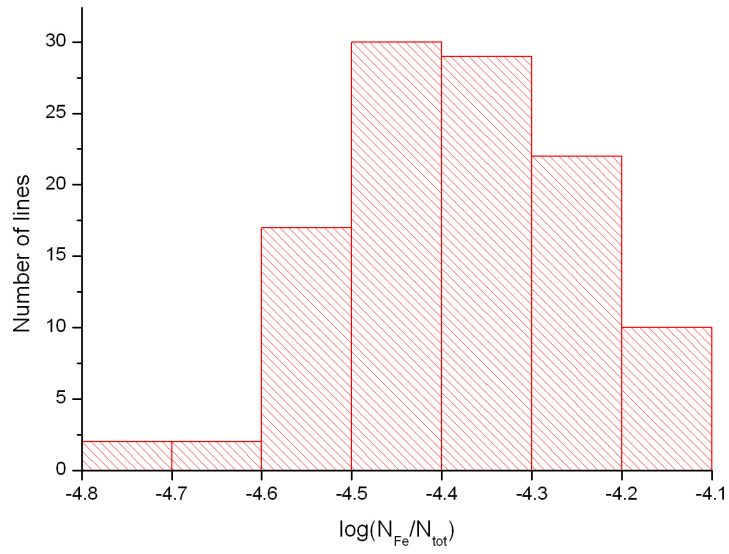


Figure 56: Histogram for Fe I and II lines.

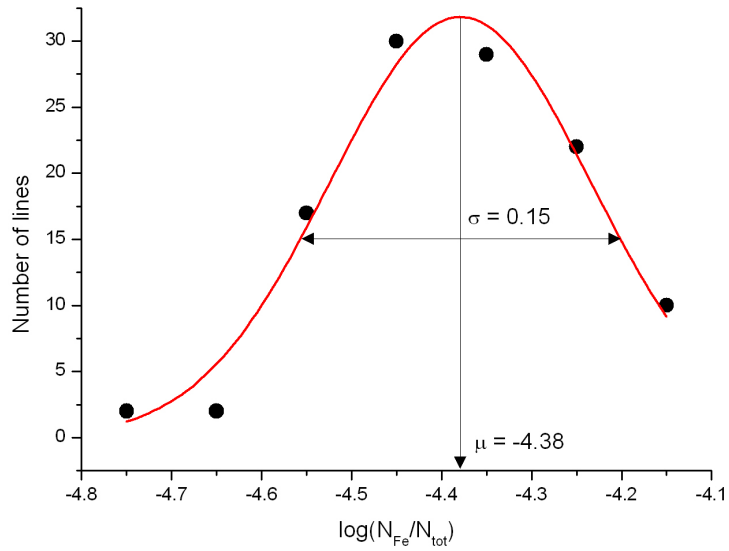


Figure 57: Gaussian fit to the histogram from Figure 56.

3.3.2. Results

Table 10 shows the sequence, the central line depth limit used for the line selection and the number of finally useable lines.

The sequence is based on the number of useable lines and the opacity contribution. Elements that show many good lines will be fitted with a higher accuracy, elements with a higher abundance are more important for the structure of the stellar model. A combination of the criteria results in the table shown below.

After the abundance of iron was determined, chromium was analysed based on the new iron abundance. With the new abundances for iron and chromium, the titanium abundance was determined and so on. Each abundance determination in the list is based on the abundance determinations above it. The central line depth limit was changed from 0.1 to 0.01 until enough good lines could be fitted. For some elements as Co, Zr, Nd and Gd, a decreased limit resulted in a much larger sample of useable lines. This is mainly caused by the overabundance of these elements. The line selection and the contribution limit are initially based on solar abundance. Using weaker lines typically doesn't improve the situation but in the case of overabundance, lines that were assumed to have a small central line depth in a solar type star become more prominent. One should therefore lower the contribution limit until a reliable decision on the element abundance can be made.

Element	Central line depth limit	#lines	Element	Central line depth limit	#lines
Fe		112	Zn	0.05	2
Cr	0.1	94	Sr	0.05	2
Ti	0.1	113	Sr	0.01	3
Ca	0.1	48	Zr	0.05	13
Ni	0.1	76	Zr	0.025	27
Mg	0.1	15	Nd	0.05	11
Mn	0.1	33	Nd	0.025	69
Si	0.1	21	Eu	0.05	1
Na	0.05	5	Eu	0.025	1
Sc	0.05	18	Gd	0.05	1
V	0.05	17	Gd	0.025	42
O	0.05	10	Dy	0.05	0
C	0.05	47	Dy	0.025	4
N	0.01	0	Ga	0.05	0
Ba	0.01	4	Ga	0.025	1
La	0.01	17	Ho	0.05	0
Y	0.05	11	Ho	0.025	1
Ce	0.05	21	Pr	0.05	0
S	0.05	12	Pr	0.025	1
Al	0.01	3	Sm	0.05	2
Co	0.05	2	Sm	0.025	5
Co	0.025	84	Th	0.05	0
Cu	0.05	2	Th	0.025	0

Table 10: Analysis sequence (top left to bottom right), central line depth limit and number of useable lines.

The iterative approach

Element	$\log(N/N_{\text{tot}})$ neutral	Error (st.dev.)	#lines	$\log(N/N_{\text{tot}})$ single ionized	Error (st.dev.)	#lines
C	-3.79	0.39	47			
O	-3.72	0.13	10			
Na	-5.56	0.07	5			
Mg	-4.52	0.16	9	-4.68	0.23	6
Al	-5.46	0.19	3			
Si	-4.64	0.31	18	-4.98	0.32	3
S	-4.84	0.12	12			
Ni	-5.54	0.37	74	-5.45	0.45	2
Sc				-9.16	0.13	18
Ti	-7.06	0.15	35	-7.27	0.29	78
V	-8.04	0.35	3	-7.97	0.62	14
Cr	-6.01	0.40	46	-5.93	0.37	48
Mn	-6.73	0.48	31	-6.59	0.48	2
Fe	-4.38	0.15	90	-4.38	0.12	22
Co	-6.17	0.52	75	-6.30	0.51	9
Ca	-5.74	0.21	36	-6.20	0.42	12
Cu	-7.59	0.22	2			
Zn	-7.26	0.17	2			
Ga				-8.96		1
Sr	-8.02	0.62	2	-8.71		1
Y				-9.50	0.30	11
Zr				-9.15	0.54	27
Ba				-8.54	0.31	4
La				-9.97	0.30	17
Ce				-9.87	0.39	21
Pr				-9.75		1
Nd(II/III)	-9.82	0.56	66	-10.12	0.49	3
Sm				-10.46	0.40	5
Eu				-11.50		1
Gd				-9.38	0.28	42
Dy				-10.45	0.63	4
Ho				-11.53		1

Table 11: Abundances, internal sample errors (standard deviation) and number of used lines for different ionization stages.

Table 11 above shows the results for the individual ionization stages (for Nd, the given values are for single and double ionized ions). Table 12 below shows the average abundances for the two ionization stages together with the solar abundances taken from Asplund, Grevesse, Sauval (2005) and Holweger (2001).

Figure 58 is a plot of the data from Table 11 and shows the abundances derived for individual elements and different ionization stages with respect to the sun ($Diff. = 0$ in Table 12).

The iterative approach

Element	Sun $\log(N/N_{\text{tot}})$	HD 8801 $\log(N/N_{\text{tot}})$	Error (st.dev.)	Diff.
C	-3.65	-3.79	0.39	-0.14
O	-3.38	-3.72	0.13	-0.34
Na	-5.87	-5.56	0.07	0.31
Mg	-4.51	-4.58	0.20	-0.07
Al	-5.67	-5.46	0.19	0.21
Si	-4.53	-4.71	0.43	-0.18
S	-4.90	-4.84	0.12	0.06
Ni	-5.81	-5.54	0.37	0.27
Sc	-8.99	-9.16	0.13	-0.17
Ti	-7.14	-7.23	0.29	-0.09
V	-8.04	-7.98	0.57	0.06
Cr	-6.40	-5.97	0.39	0.43
Mn	-6.65	-6.72	0.48	-0.07
Fe	-4.59	-4.38	0.15	0.21
Co	-7.12	-6.15	0.55	0.97
Ca	-5.73	-5.74	0.32	-0.01
Cu	-7.83	-7.59	0.22	0.25
Zn	-7.44	-7.26	0.17	0.18
Ga	-9.16	-8.96		0.20
Sr	-9.12	-8.25	0.59	0.87
Y	-9.83	-9.50	0.30	0.33
Zr	-9.45	-9.15	0.54	0.30
Ba	-9.87	-8.54	0.31	1.33
La	-10.91	-9.97	0.30	0.94
Ce	-10.46	-9.87	0.39	0.59
Pr	-11.33	-9.75		1.58
Nd	-10.59	-9.84	0.58	0.75
Sm	-11.03	-10.46	0.40	0.57
Eu	-11.52	-11.50		0.02
Gd	-10.92	-9.38	0.28	1.54
Dy	-10.90	-10.45	0.63	0.45
Ho	-11.53	-11.53		0.00

Table 12: Solar abundances compared to HD 8801.

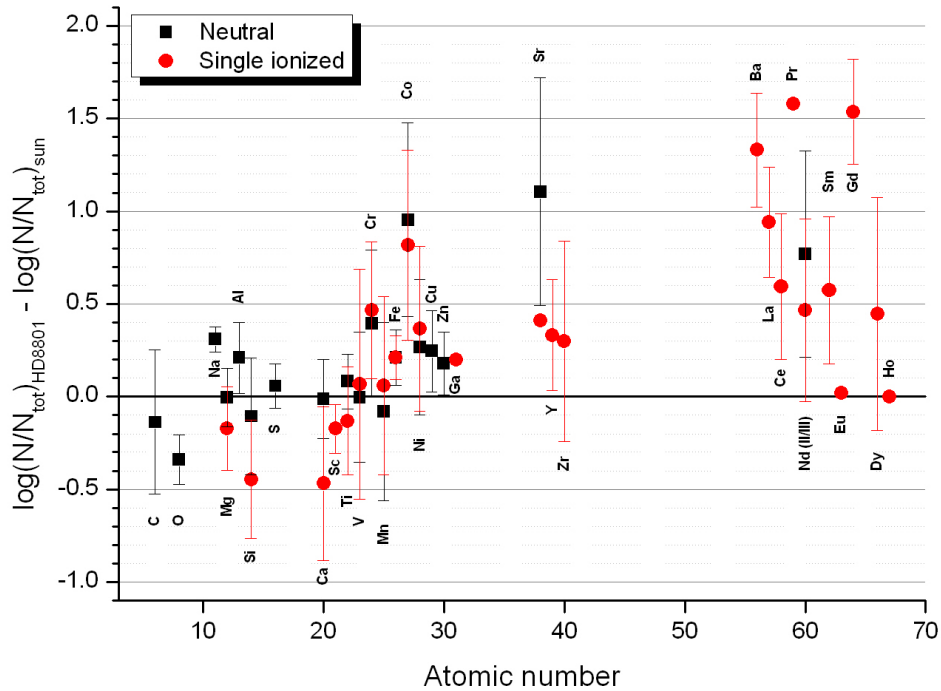


Figure 58: Abundances relative to the sun for different ionization stages after first iteration.

3.4. Refining the parameters

In case of a slow rotating star with mostly unblended lines and an abundance pattern similar to the sun, the abundance analysis would now be finished. In the case of HD 8801 at least a second iteration had to follow. This is because all lines are more or less blended by other lines and a change in the abundance of one element influences the abundance determination of the others. In the beginning, the abundances of all elements were assumed to be solar. If there is more pre-knowledge about the abundances of a star, the initial abundances could be adjusted in the beginning but for HD 8801, this was not the case.

The first element for which an abundance was calculated was iron. This abundance determination was based on a solar abundance pattern for all other elements. Therefore, the absorption contribution of blending lines originating from other elements like chromium, titanium, nickel etc. were under- or overestimated (in the case of this star, mostly underestimated).

The atmospheric parameters are not influenced strongly by the changed abundance pattern because the analysed trends are independent from the absolute abundances. Nevertheless, a fine tuning of the atmospheric parameters is advisable before starting the second abundance determination because only after the process has converged, the correct abundances can be determined. Some lines which were selected in the beginning are possibly no longer useable, whereas some other could become useful. In this case, 99 iron lines out of the initially 112 remained. This is mainly because of the increased abundances for all other elements and their resultant absorption domination over the weaker iron lines.

3.4.1. Refining the microturbulence

In the refining process it was possible to use other elements than iron as well, as the absorption contributions of blending lines were now estimated accurately enough. Chromium, titanium and nickel now showed enough lines of good quality. ODF-models were calculated for different microturbulences and the same methods were applied as in chapter 0.

The errors given in the summary tables are only standard deviations based on the line sample and do not include the slope errors nor any error propagation. This is discussed later in chapter 4.

Iron

Table 13 and Figure 59 show the results for iron without Fe I at 4181.754 Å.

v_{mic} [km/s]	Slope	Slope error
1.60	-0.85	0.27
1.80	-0.68	0.25
2.00	-0.47	0.24
2.20	-0.25	0.23
2.40	0.02	0.23
2.59	0.17	0.22
2.80	0.50	0.22
3.00	0.73	0.23

Table 13: Slopes and errors without Fe I at 4181.754 Å.

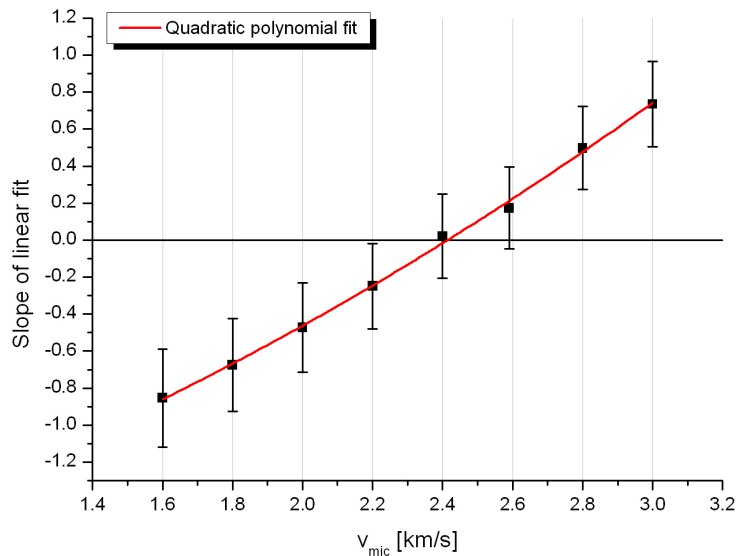


Figure 59: Plot of data from Table 13.

The zero of the applied fit leads to a microturbulence of 2.41 km/s.

Instead of using slopes of abundance-versus-central line depth fits, the abundance error (standard deviation) for the different microturbulence velocity models can be used. This is shown in Figure 60. The minimum of a polynomial fit through the data resulted in a value of 2.58 km/s which confirmed the value of 2.41 km/s within the estimated errors (see error bars in Figure 59).

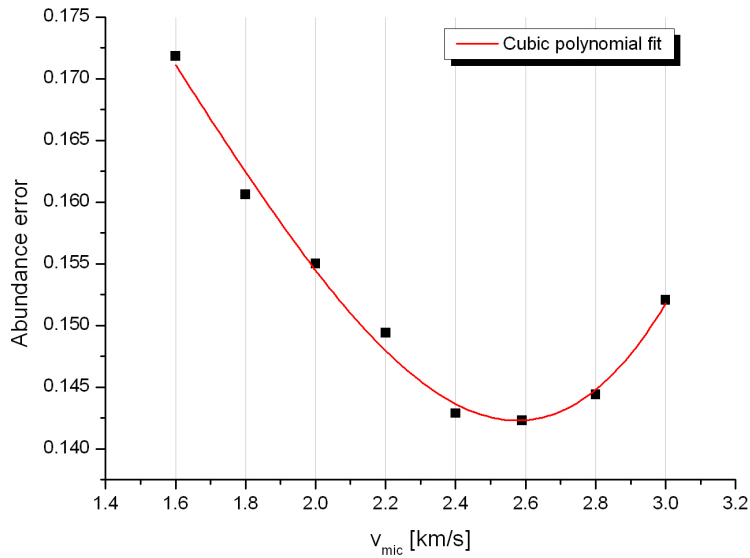


Figure 60: Abundance errors of the 99 iron line sample versus microturbulence.

Sometimes, not all lines in a sample can be used to determine all atmospheric parameters. For some lines, the dependency of blending lines on a parameter can have a large influence on the result. This was the case for a single iron line at 4181.754 Å. The abundance for this line jumped from -4.77 dex for $v_{mic} = 2.0$ km/s to -4.08 dex for $v_{mic} = 2.25$ km/s and influenced the slope of the linear fit significantly (see Figure 61). This emphasizes the need to carefully select the lines used to determine the atmospheric parameters and to have an eye on the results during the iteration process.

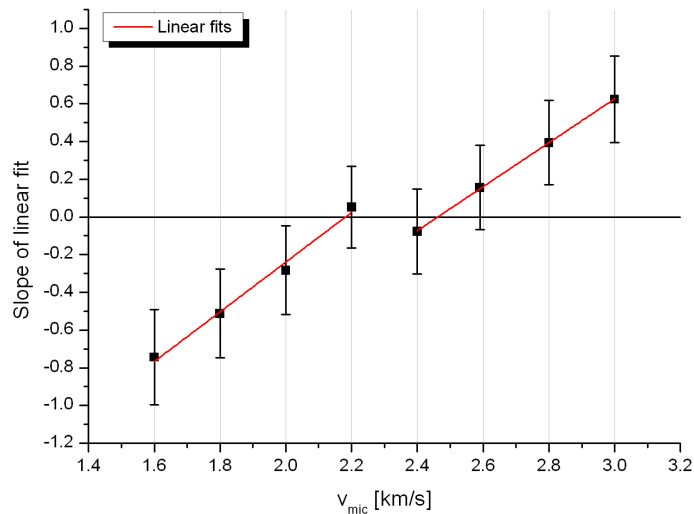


Figure 61: Slope jump due to a single Fe I line at 4181.754 Å.

Chromium

The line selection was repeated with the new abundances from chapter 0 and now resulted in 130 lines. The results for the different microturbulences are shown in Table 14 and Figure 62 below.

v_{mic} [km/s]	Slope	Slope error	$\log(N_{\text{Cr}}/N_{\text{tot}})_{\text{ave}}$	Abundance error (st.dev.)
2.00	-3.49	0.64	-6.09	0.44
3.00	-0.98	0.83	-6.30	0.52
4.00	0.88	0.74	-6.34	0.47

Table 14: Slopes, errors and abundances for chromium for different microturbulences.

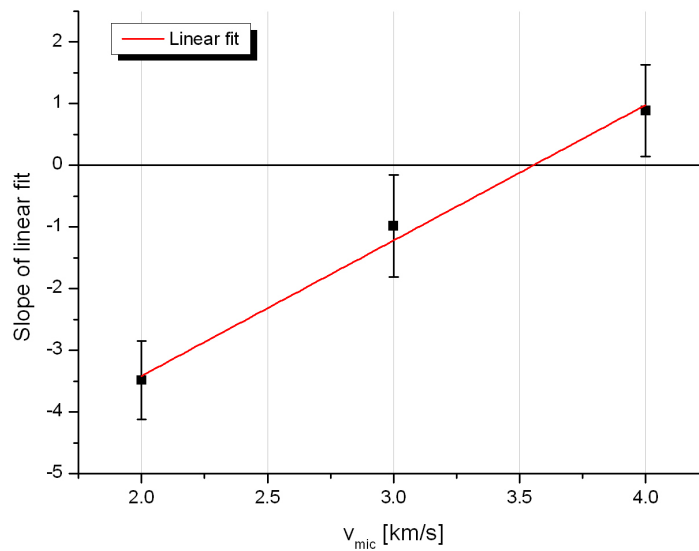


Figure 62: Plot of data from Table 14.

The zero for the linear fit in Figure 62 is at a microturbulence of 3.55 km/s.

Titanium

78 lines were found to be useable and remained after removing all lines with an RMS error > 1 and 3 σ outliers. Results are shown in Table 15 and Figure 63.

v_{mic} [km/s]	Slope	Slope error	$\log(N_{\text{T}}/N_{\text{tot}})_{\text{ave}}$	Abundance error (st.dev.)
2.00	-3.49	0.64	-6.09	0.44
3.00	-0.98	0.83	-6.30	0.52
4.00	0.88	0.74	-6.34	0.47

Table 15: Slopes, errors and abundances for titanium for different microturbulences.

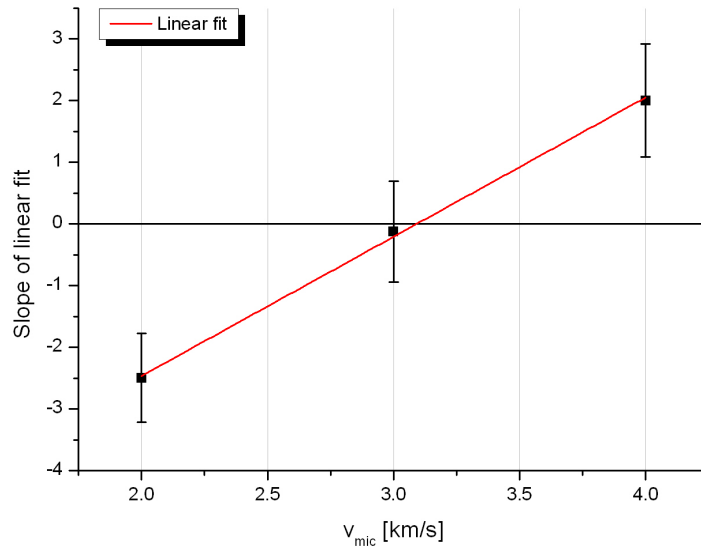


Figure 63: Plot of data from Table 15.

The optimal microturbulence for titanium would be 3.09 km/s.

Nickel

Using 117 Nickel lines resulted in Table 16 and Figure 64.

v_{mic} [km/s]	Slope	Slope error	$\log(N_{Ni}/N_{tot})_{ave}$	Abundance error (st.dev.)
2.00	-2.90	0.74	-5.44	0.40
3.00	-0.33	0.75	-5.59	0.39
4.00	2.04	0.73	-5.64	0.39

Table 16: Slopes, errors and abundances for nickel for different microturbulences.

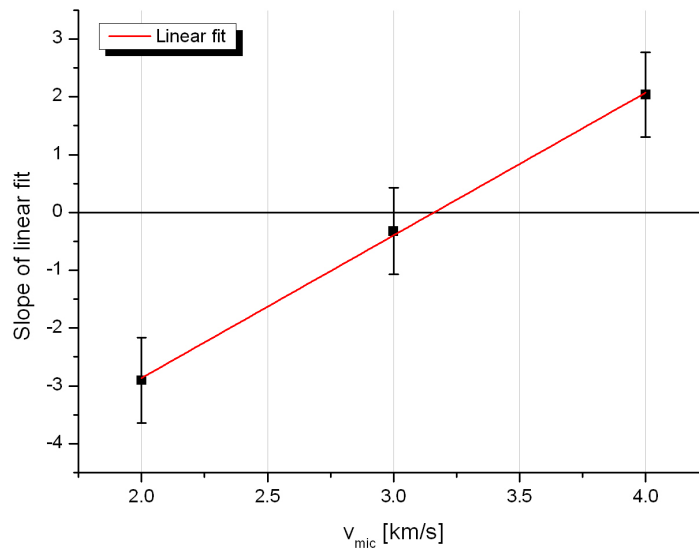


Figure 64: Plot of data from Table 16.

Nickel requires a microturbulence of 3.16 km/s.

Summary

Cr, Ti and Ni indicated a larger value for the microturbulence than iron (see Table 17). The average is taken as the final value.

Element	v_{mic} [km/s]	#lines
Fe	2.41	99
Cr	3.55	130
Ti	3.09	78
Ni	3.16	117
Average	3.05	
St.dev	0.48	

Table 17: Final determination for the microturbulence velocity based on four elements.

As this value was about 0.5 km/s higher than the initial one, the abundances for iron would change and consequently the solar scale which was used in the ODF-models. In order to account for that change, the abundance for iron was determined by fitting a polynomial through the abundance averages for the different microturbulences (Table 18). This is shown in Figure 65.

v_{mic} [km/s]	$\log(N_{\text{Fe}}/N_{\text{tot}})_{\text{ave}}$
1.60	-4.22
1.80	-4.27
2.00	-4.32
2.20	-4.37
2.40	-4.41
2.59	-4.45
2.80	-4.49
3.00	-4.52

Table 18: Average iron abundances for models with different microturbulences.

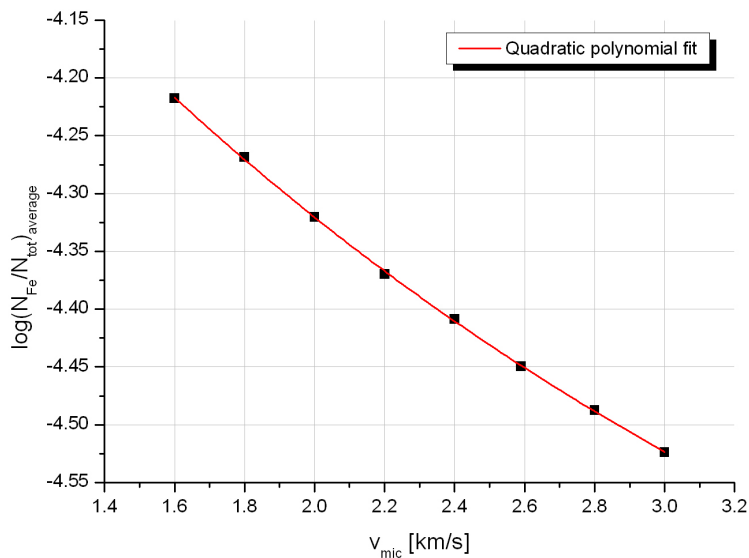


Figure 65: Iron abundances for different microturbulences. Extrapolation of the polynomial fit to 3.05 km/s resulted in an iron abundance of -4.53 dex.

The iron abundance of -4.53 dex gives a solar scaled value of +0.06. This was used for the next iteration step.

3.4.2. Refining the gravity

Here, only iron and chromium could be used as nickel showed only two lines of Ni II and titanium gave a significantly higher value for the gravity which wasn't suitable for the other elements. The reason for this is unclear.

Iron

Table 19 and Figure 66 show the results for iron.

$\log g$ [cm/s ²]	$\log(N_{\text{FeI}}/N_{\text{tot}})_{\text{ave}}$	Error (st.dev.)	$\log(N_{\text{FeII}}/N_{\text{tot}})_{\text{ave}}$	Error (st.dev.)	Abundance difference
3.47	-4.47	0.15	-4.63	0.15	0.16
3.67	-4.48	0.15	-4.58	0.15	0.10
3.87	-4.48	0.15	-4.53	0.15	0.04
4.07	-4.49	0.15	-4.48	0.16	-0.01

Table 19: Abundance differences for models with different gravities for iron.

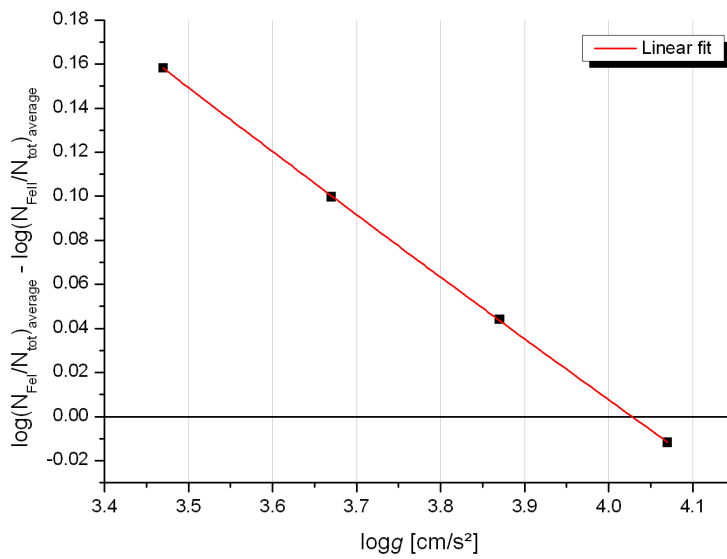


Figure 66: Plot of data from Table 19.

The zero of the linear fit lies at 4.03 cm/s².

Chromium

Table 20 and Figure 67 contain the results for chromium.

$\log g$ [cm/s^2]	$\log(N_{\text{CrI}}/N_{\text{tot}})_{\text{ave}}$	Error (st.dev.)	$\log(N_{\text{CrII}}/N_{\text{tot}})_{\text{ave}}$	Error (st.dev.)	Abundance difference
3.47	-6.11	0.41	-6.20	0.38	0.09
3.67	-6.08	0.38	-6.15	0.38	0.06
3.87	-6.05	0.37	-6.09	0.39	0.04
4.07	-6.03	0.38	-6.03	0.38	0.00

Table 20: Abundance differences for models with different gravities for chromium.

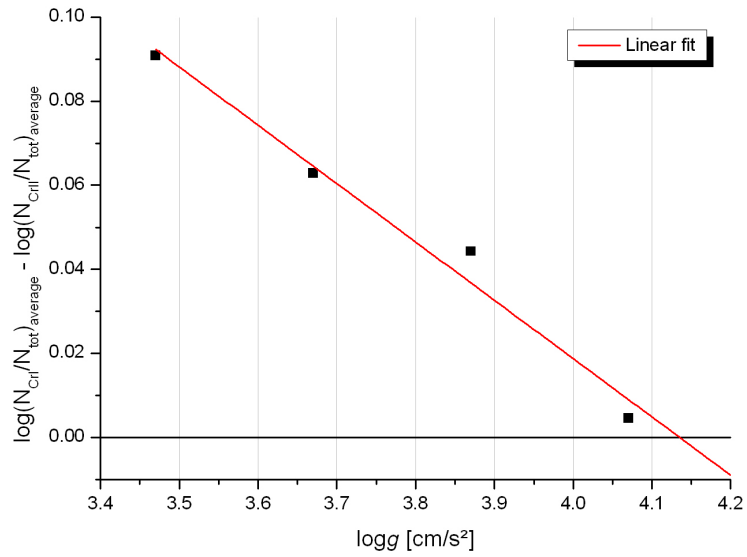


Figure 67: Plot of data from Table 20.

The zero of the linear fit lies at 4.14 cm/s^2 .

Titanium

The results for titanium are shown in Table 21 and Figure 68.

$\log g$ [cm/s ²]	$\log(N_{\text{TiI}}/N_{\text{tot}})_{\text{ave}}$	Error (st.dev.)	$\log(N_{\text{TiII}}/N_{\text{tot}})_{\text{ave}}$	Error (st.dev.)	Abundance difference
3.47	-7.14	0.29	-7.51	0.38	0.37
3.67	-7.11	0.28	-7.42	0.35	0.32
3.87	-7.09	0.28	-7.35	0.32	0.26
4.07	-7.07	0.28	-7.27	0.30	0.20

Table 21: Abundance differences for models with different gravities for titanium.

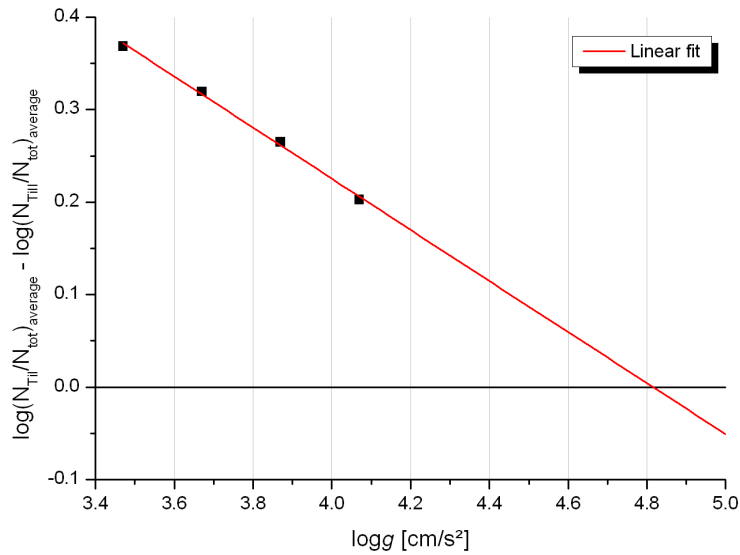


Figure 68: Plot of data from Table 21.

The zero is found to be at 4.82 cm/s² as can be seen from Figure 68. Titanium doesn't behave like iron or chromium and was omitted in the determination process although 19 Ti I and 65 Ti II lines were used. The reason for this discrepancy is unknown.

Summary

Table 22 collects the results for iron and chromium. The standard deviation cannot be taken as a real error. This will be discussed in chapter 4.

Element	logg [cm/s ²]	#lines
Fe	4.03	99
Cr	4.14	130
Average	4.08	
St.dev	0.08	

Table 22: Final determination for the gravity based on two elements.

The new iron abundance of -4.48 dex which was determined similar to the iron abundance as described in the summary of chapter 0, gives a value for Z of +0.11.

3.4.3. Refining the effective temperature

Iron

The results for iron are shown in Table 23 and Figure 69 below.

T _{eff} [K]	Slope	Slope error	log(N _{Fe} /N _{tot}) _{ave}	Abundance error (st.dev.)
7340	0.01	0.02	-4.62	0.17
7540	0.00	0.01	-4.49	0.15
7740	-0.01	0.01	-4.36	0.13

Table 23: Slopes, errors and abundances for iron for different effective temperatures.

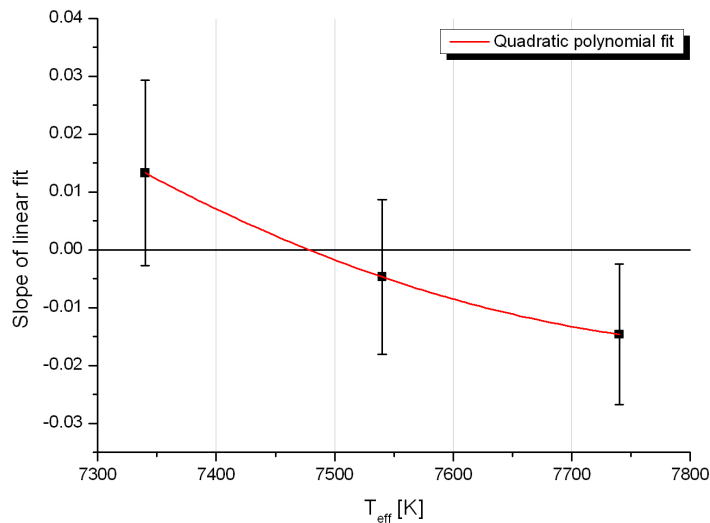


Figure 69: Plot of data from Table 23.

The zero of the polynomial fit in Figure 69 results in a temperature for iron of 7478 K.

Chromium

Table 24 and Figure 70 hold the results for chromium.

T_{eff} [K]	Slope	Slope error	$\log(N_{\text{Cr}}/N_{\text{tot}})_{\text{ave}}$	Abundance error (st.dev.)
7340	0.13	0.03	-6.40	0.52
7540	0.09	0.02	-6.03	0.35
7740	0.07	0.03	-5.80	0.37

Table 24: Slopes, errors and abundances for chromium for different effective temperatures.

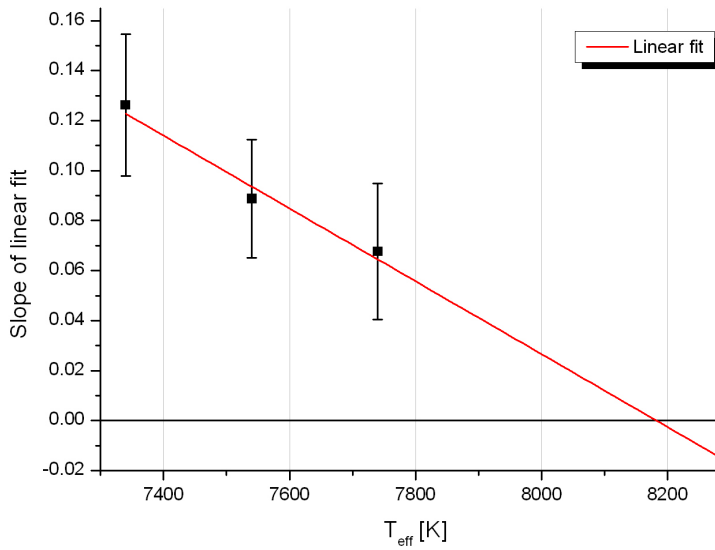


Figure 70: Plot of data from Table 24.

Chromium shows a significant higher optimum temperature (8180 K) than iron, titanium or nickel and was therefore omitted. The reason for this is again unknown.

Titanium

Table 25 and Figure 71 show the results for titanium.

T_{eff} [K]	Slope	Slope error	$\log(N_{\text{Ti}}/N_{\text{tot}})_{\text{ave}}$	Abundance error (st.dev.)
7340	0.02	0.07	-7.56	0.40
7540	0.01	0.05	-7.25	0.31
7740	-0.03	0.05	-6.99	0.29

Table 25: Slopes, errors and abundances for titanium for different effective temperatures.

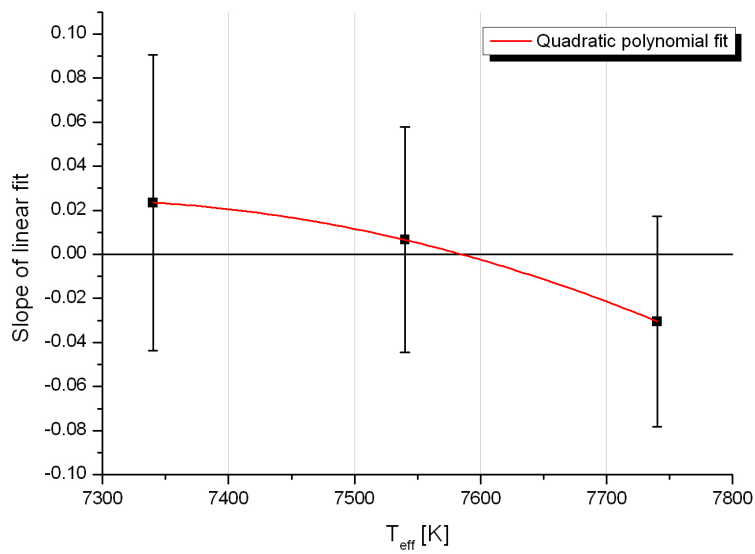


Figure 71: Plot of data from Table 25.

The zero for the polynomial fit results in a temperature for titanium of 7585 K.

Nickel

The values for nickel are shown in Table 26 and Figure 72.

T_{eff} [K]	Slope	Slope error	$\log(N_{\text{Ni}}/N_{\text{tot}})_{\text{ave}}$	Abundance error (st.dev.)
7340	0.15	0.07	-5.85	0.55
7540	0.03	0.04	-5.53	0.36
7740	-0.02	0.04	-5.23	0.29

Table 26: Slopes, errors and abundances for nickel for different effective temperatures.

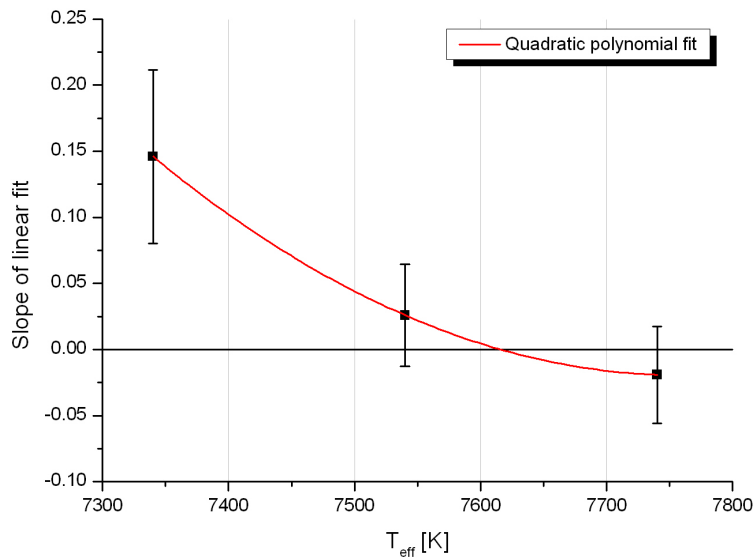


Figure 72: Plot of data from Table 26.

Nickel needs 7616 K to remove the trend from the excitation potential-versus-abundance relation.

Summary

Element	T_{eff} [K]	#lines
Fe	7478	99
Ti	7585	73
Ni	7616	111
Average	7560	
St.dev	72	

Table 27: Final determination of the temperature based on three elements. The last digit in the temperature values are purely mathematical and should not be taken serious.

The final temperature was determined to 7560 K (see Table 27) which was only slightly higher than the initial value. This indicated that the system converged.

Here, the number of lines was not used to calculate a weighted average, as the number of lines is not a good measure for the quality of the determination. Having many bad lines doesn't result in a reliable average value.

In order to check the convergence, the slopes of abundance-versus-central line depth, abundance-versus-excitation potential and the abundance differences between the ionization stages I and II were calculated for iron, chromium, titanium and nickel.

The results indicated that a final solution was found as all slopes and the abundance differences were close to 0. Therefore, the iteration was stopped at this point.

3.5. Final abundances

With the preliminary abundances and the new atmospheric parameters, an LL stellar model was calculated as this calculation type takes the individual abundances and therefore opacities into account. With this model the abundances and different slopes used in the determination processes for the atmospheric parameters for iron, chromium, titanium and nickel were calculated once more. The differences were small compared to the errors and no further adjustment was necessary.

Using this final model, the abundances for all other elements were determined again. As the distributions for the individual line abundances were now closer to a Gaussian distribution, the standard deviation and arithmetic means were used to calculate the abundances and internal errors.

Figure 73 shows the abundance differences for titanium, chromium, iron and nickel based on the final ODF-model and the final LL-model. The LL-model gives slightly lower abundances than the ODF-model.

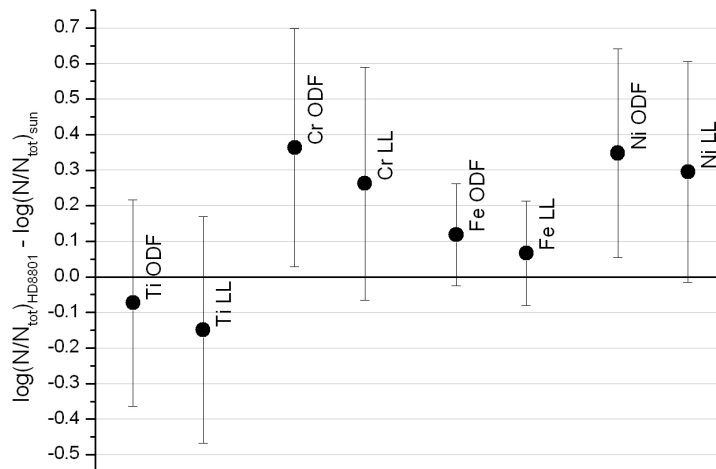


Figure 73: Abundances based on the final ODF-model with $Z = +0.12$ and the LL-model based on the abundances from the first determination.

The same element sequence and line selection was used as for the initial analysis. The RMS error for each line was checked and the line was removed if the value exceeds 1. Lines that show an abundance, 3σ away from the sample average were rejected too. This led to a smaller sample, but with better defined lines. Lines that can be fitted with different stellar models (the initial models and the models after the first abundance

The iterative approach

determination) are of higher quality as lines that are unstable to changes in the stellar parameters.

The fact that the abundances were now better defined, allowed to search for lines originating from elements with low abundance and/or a sparsely populated line pattern. The following tables (Table 28 and Table 29) show the final results of this abundance analysis including errors, Figure 74 and Figure 75 are graphical representations.

Element	Sun log(N/N _{tot})	HD 8801 log(N/N _{tot})	Error (st.dev.)	Diff.
C	-3.65	-3.75	0.31	-0.10
N	-4.26	-4.58	0.29	-0.32
O	-3.38	-3.71	0.27	-0.33
Na	-5.87	-5.84	0.36	0.03
Mg	-4.51	-4.66	0.18	-0.15
Al	-5.67	-5.51	0.19	0.16
Si	-4.53	-4.79	0.34	-0.26
S	-4.90	-4.78	0.14	0.12
Cl	-6.54	-6.54		0.00
K	-6.96	-6.43		0.53
Ca	-5.73	-5.89	0.20	-0.16
Sc	-8.99	-9.13	0.27	-0.14
Ti ODF	-7.14	-7.21	0.29	-0.07
Ti LL	-7.14	-7.29	0.32	-0.15
V	-8.04	-7.95	0.35	0.09
Cr ODF	-6.40	-6.04	0.33	0.36
Cr LL	-6.40	-6.14	0.33	0.26
Mn	-6.65	-6.90	0.40	-0.25
Fe ODF	-4.59	-4.47	0.14	0.12
Fe LL	-4.59	-4.52	0.15	0.07
Co	-7.12	-6.06	0.42	1.06
Ni ODF	-5.81	-5.46	0.29	0.35
Ni LL	-5.81	-5.51	0.31	0.30
Cu	-7.83	-7.70	0.20	0.13
Zn	-7.44	-7.31	0.08	0.13
Sr	-9.12	-8.30	0.52	0.82
Y	-9.83	-9.35	0.30	0.48
Zr	-9.45	-8.95	0.25	0.50
Ba	-9.87	-8.63	0.30	1.24
La	-10.91	-9.83	0.18	1.08
Ce	-10.46	-9.73	0.19	0.73
Pr	-11.33	-9.70	0.21	1.63
Nd	-10.59	-9.65	0.44	0.94
Sm	-11.03	-10.15	0.17	0.88
Eu	-11.52	-11.30		0.22
Gd	-10.92	-9.22	0.40	1.70
Dy	-10.90	-9.91	0.54	0.99
Ho	-11.53	-11.66	0.12	-0.13

Table 28: Average abundances with errors, solar abundances taken from Asplund et al. and Holweger and abundance differences.

The iterative approach

Element	$\log(N/N_{\text{tot}})$ neutral	Error (st.dev.)	#lines	$\log(N/N_{\text{tot}})$ single ionized	Error (st.dev.)	#lines
C	-3.75	0.31	42			
N	-4.58	0.29	4			
O	-3.71	0.27	10			
Na	-5.84	0.36	5			
Mg	-4.64	0.16	9	-4.70	0.22	6
Al	-5.51	0.19	3			
Si	-4.78	0.35	18	-4.87	0.29	3
S	-4.78	0.14	10			
Cl	-6.54		1			
K	-6.43		1			
Ca	-5.90	0.17	35	-5.86	0.31	9
Sc				-9.13	0.27	17
Ti ODF	-7.10	0.33	18	-7.25	0.27	57
Ti LL	-7.19	0.35	18	-7.32	0.30	57
V	-8.13	0.28	5	-7.86	0.36	10
Cr ODF	-6.04	0.34	76	-6.04	0.33	46
Cr LL	-6.16	0.33	76	-6.10	0.32	46
Mn	-6.95	0.37	28	-6.28	0.08	2
Fe ODF	-4.47	0.14	79	-4.47	0.15	20
Fe LL	-4.53	0.15	79	-4.49	0.14	20
Co	-6.05	0.43	69	-6.11	0.35	10
Ni ODF	-5.46	0.29	110			
Ni LL	-5.51	0.31	110			
Cu	-7.70	0.20	2			
Zn	-7.31	0.08	2			
Sr	-8.12	0.56	4	-8.65	0.16	2
Y				-9.35	0.30	10
Zr				-8.95	0.25	14
Ba				-8.63	0.30	4
La				-9.83	0.18	9
Ce				-9.73	0.19	16
Pr				-9.70	0.21	13
Nd (II/III)	-9.63	0.44	31	-9.95	0.15	2
Sm				-10.15	0.17	5
Eu				-11.30		1
Gd				-9.22	0.40	37
Dy				-9.91	0.54	9
Ho (II/III)	-11.63	0.14	2	-11.73		1

Table 29: Average abundances for different ionization stages with errors including the number of analysed lines. For Nd and Ho the ionization stages are II and III.

The iterative approach

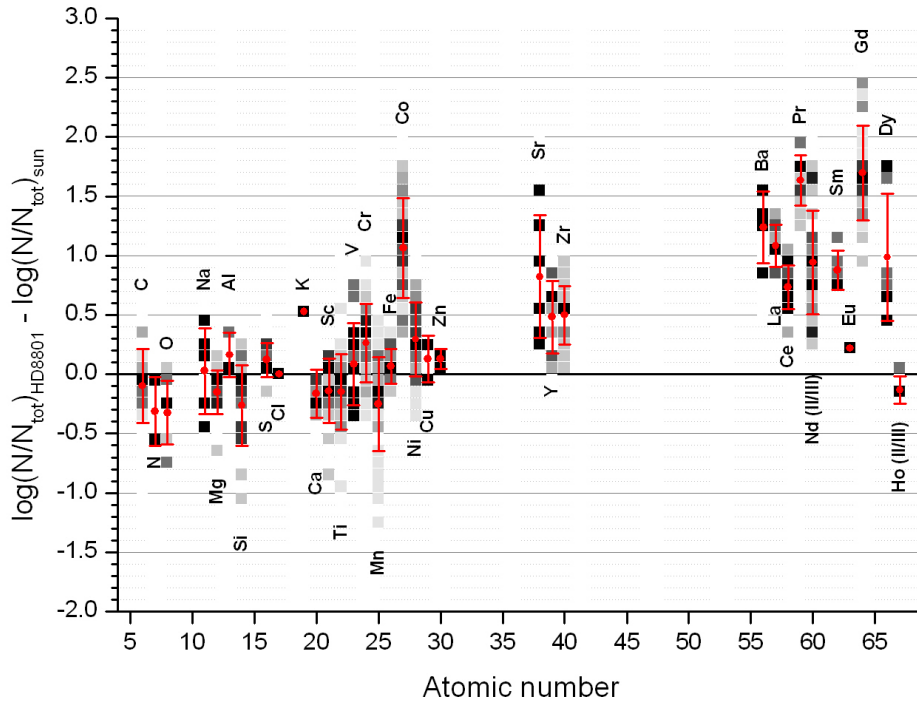


Figure 74: Average abundances. The grey bars are color coded histograms of the line-by-line abundances. The scale is from black (many lines) to light grey (few lines). The red dots with error bars mark the average values.

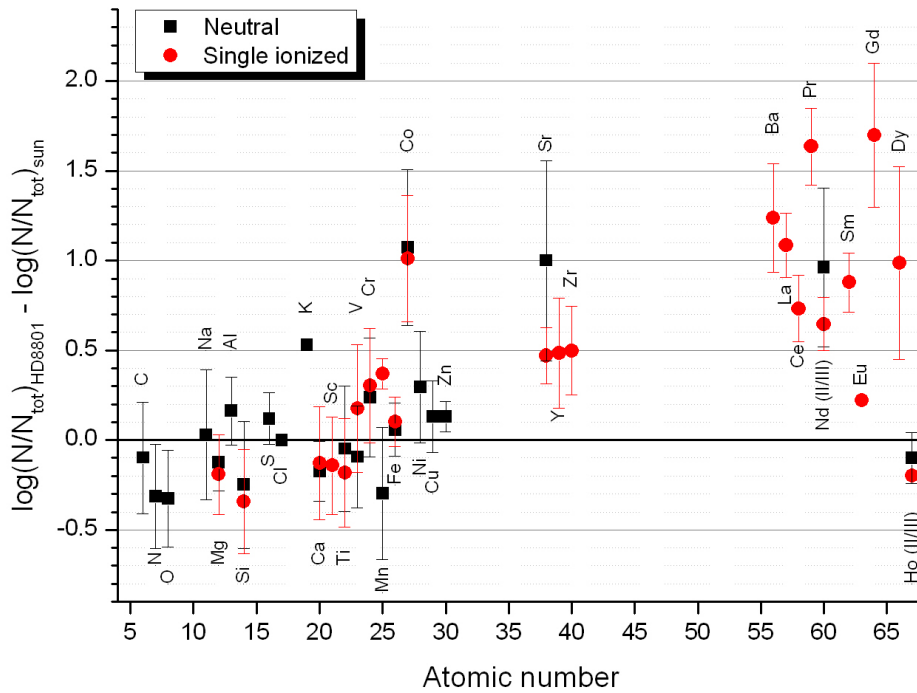


Figure 75: Abundances for individual ionization stages.

3.5.1. Individual elements

C, Sc, Ti, Zr and Ca

Due to the ionization energies of these elements comparable to the ionization energies of either H I, He I or He II, these elements usually show lower abundances than the typical overabundances of the other elements in Am stars. Table 30 shows the ionization energies for H I, He I and II together with the comparable energies for some other elements.

O, Cl, S, Eu and eventually Ho also show ionization energies close to H and He and should therefore behave similarly. Table 31 shows the abundances derived for HD 8801 for the mentioned elements. Whether the low abundance of Ho can be explained by this effect is doubtful because of the larger energy difference.

Ion	Ion. energy [eV]	Ion	Ion. energy [eV]	Ion	Ion. energy [eV]
H I	13.598	He I	24.587	He II	54.418
Sc II	12.8	C II	24.383	Ca III	50.913
Ti II	13.576	Sc III	24.757		
Ca II	11.872	(Zr III)	22.99		
O I	13.618	S II	23.338	O III	54.936
Cl I	12.968	Cl II	23.814		
(Ho II)	11.8	Eu III	24.92		
		(Ho III)	22.8		

Table 30: Ionization energies for H I, He I and II and comparable energies for different elements.

Element	$\log(N/N_{\text{tot}})_{\text{HD8801}} - \log(N/N_{\text{tot}})_{\text{sun}}$
C	-0.10
Sc	-0.14
Ti	-0.15
Zr	0.5
Ca	-0.16
O	-0.33
Cl	0
S	0.12
Eu	0.22
(Ho)	-0.13

Table 31: Abundances of elements from Table 30.

N

4 nitrogen lines were found in the infrared part of the spectrum (see Table 32 below) and result in an abundance of -4.58 ± 0.3 dex which is 0.32 dex below the solar value. The S/N in that region is rather low so that the internal error should be taken as a lower limit.

Wavelength [Å]	$\log(N_N/N_{\text{tot}})$
8629.235	-4.81
8686.149	-4.84
8703.247	-4.29
8718.8354	-4.36

Table 32: Nitrogen lines.

K

For potassium, only one but unblended line at 7698.9740 Å could be used. The best fit with $\log(N_K/N_{\text{tot}}) = -6.43$ dex is shown together with two other syntheses in Figure 76 below. A conservative error limit would be 0.3 dex. The sharp lines left to the potassium line are telluric lines.

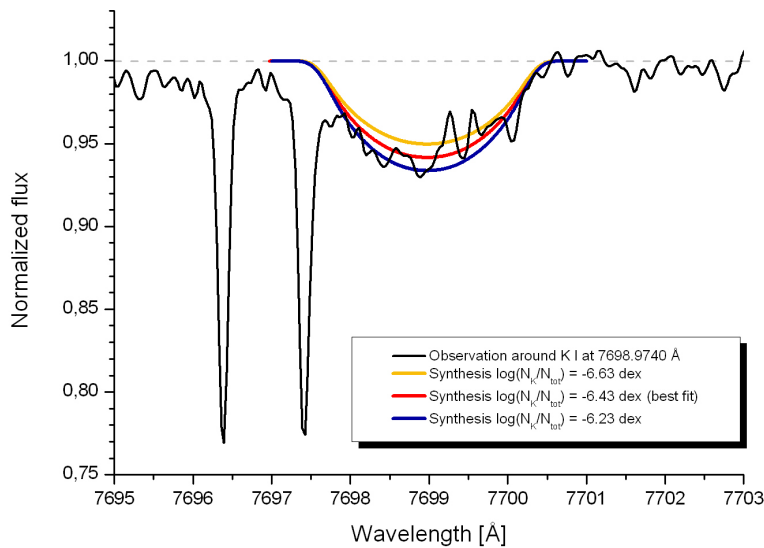


Figure 76: Synthetic spectra compared to the observation for K I line at 7698.9740 Å.

Cl

One chloride line was observable at 8912.9230 Å which was unfortunately strongly blended by a Ca II line at 8912.0680 Å. A comparison between the observation and different syntheses is shown in Figure 77. In this case, only an upper limit of $\log(N_{\text{Cl}}/N_{\text{tot}}) = -5.37$ dex for the abundance of chloride can be given. The best fit with $\log(N_{\text{Cl}}/N_{\text{tot}}) = -5.87$ dex is only marginally different than the fit with $\log(N_{\text{Cl}}/N_{\text{tot}}) = -6.37$ dex. Even completely removing chloride from the calculations would provide a feasible solution, so that no lower limit can be given. The abundance for chloride was therefore assumed to be solar.

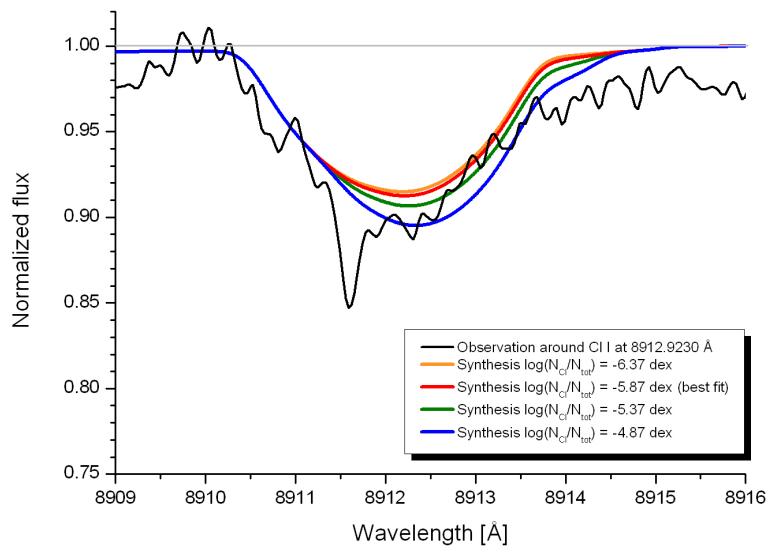


Figure 77: Synthetic spectra compared to the observation for Cl I line at 8912.9230 Å.

Eu

For europium, one line at 4435.578 Å was found. This line is strongly blended by several elements (see Figure 78). Here, only an estimation and an upper limit can be given. The best fit gives $\log(N_{\text{Eu}}/N_{\text{tot}}) = -11.30$ dex, $\log(N_{\text{Eu}}/N_{\text{tot}}) = -10.80$ dex is possible and $\log(N_{\text{Eu}}/N_{\text{tot}}) = -10.30$ dex is improbable.

Nevertheless, europium shows a lower abundance than other rare earth elements which could be due to the vicinity of the ionization energies of Eu III and He I (see Table 30 above).

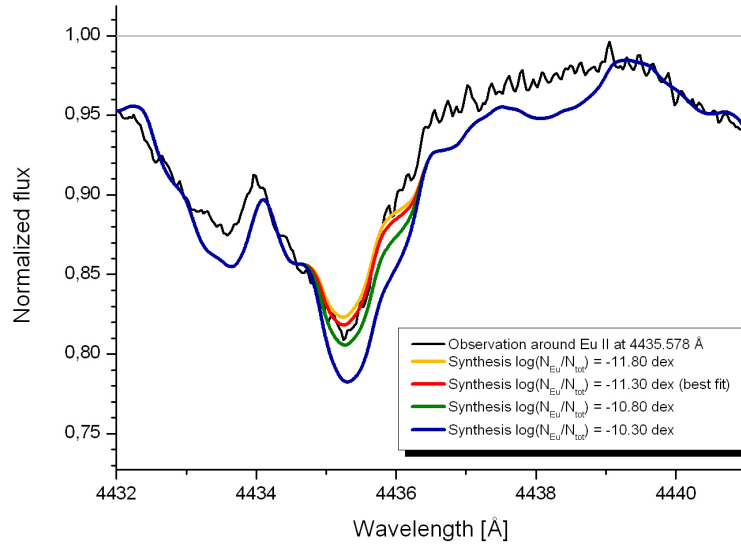


Figure 78: Synthetic spectra compared to the observation for Eu II line at 4435.578 Å.

Comparison between observation and synthesis

Figure 79 and Figure 80 show comparisons between the observation, an initial synthesis based on the atmospheric parameters derived from photometry and solar abundances and the synthesis based on the final atmospheric parameters and abundances. The agreement between the final synthesis and the observation is well throughout the whole spectrum.

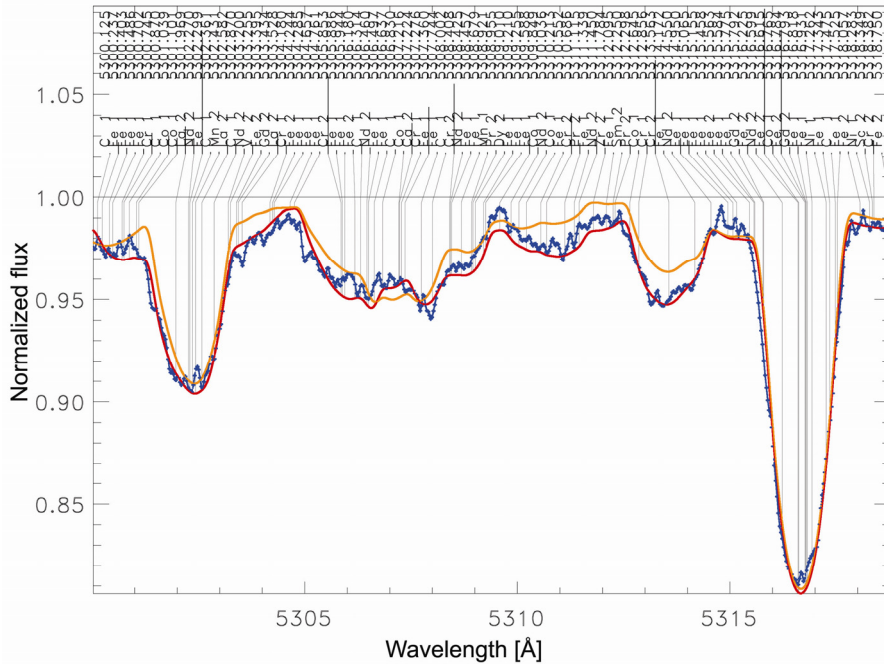


Figure 79: Comparison between observation (blue), initial synthesis based on photometry (orange) and synthesis based on the final atmospheric parameters and abundances (red).

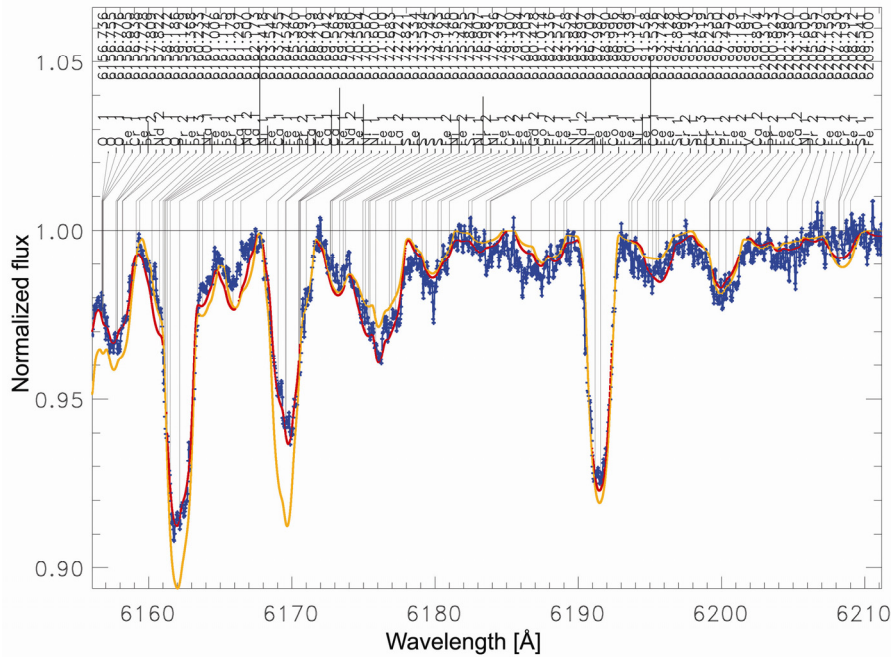


Figure 80: Same as Figure 79 but for a different wavelength region.

4. Discussion of errors

4.1. Continuum errors

The continuum normalization is the main error source in abundance analysis. This is demonstrated by the following experiment.

The total observation was shifted by 1% in the positive and negative direction in relative intensity. The iron line abundances based on the 99 iron line sample were calculated for the shifted observation and compared to the unshifted results. This allowed to estimate the individual errors for each line due to a wrong normalization. Figure 81 shows the iron lines including these errors. Averages are marked by the colored horizontal lines.

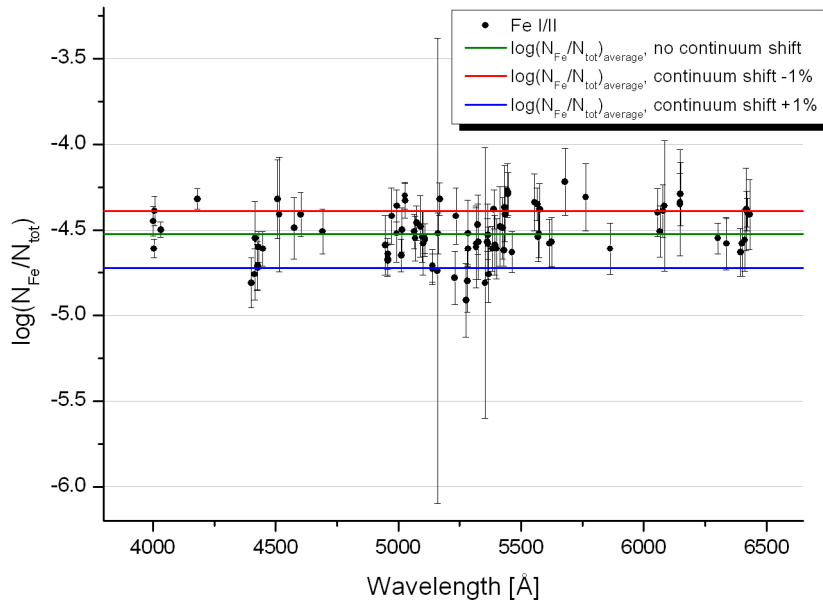


Figure 81: Iron line abundances with individual errors due to a wrong continuum normalization.

Some lines show an extraordinary large error which is caused by the inability of the algorithm to fit the specific line when a shift in the continuum is applied. The typical error is 0.17 dex with a minimum at 0.05 dex and a maximum at 1.36 dex.

This is larger than the total error within the line sample itself (0.15 dex). As the real continuum error varies throughout the observation in both directions (positive and negative), no change in the average abundance is expected but a large increase in the scatter. Line blending together with rotational broadening can produce such a systematic shift as shown in chapter 2.3.2. A careful correction of this effect is necessary for faster rotating stars especially in the blue part of the spectrum where the continuum is not reached to avoid a shift in abundance.

This shows that it is unavoidable to take great care in the normalization process before starting the analysis process.

4.2. Influence of the S/N ratio

In order to get information about the influence of the signal-to-noise ratio on the abundance determination, a synthetic spectrum based on the final atmospheric parameters and abundances was calculated for the wavelength-range 4000 – 4100 Å. This region was chosen, as the line blending is strongest at the blue limit of the observations and the influence of the S/N ratio on the line fitting algorithm should be maximal. A normal distributed noise was then added to the synthetic spectrum to simulate a noisy observation. This was done for different values of the S/N ratio. These artificial observations were then used as observations. Iron lines with a central line depth larger than 0.3 (without rotational broadening) were selected and afterwards automatically fitted. The results are shown in Table 33 and Figure 82.

S/N ratio	$\log(N_{\text{Fe}}/N_{\text{tot}})$	Error (st.dev.)
10	-4.526	0.189
25	-4.520	0.087
50	-4.520	0.035
100	-4.518	0.010
200	-4.519	0.007
300	-4.519	0.004
∞	-4.520	0.000

Table 33: Abundance determinations for artificial spectra with different S/N ratios.

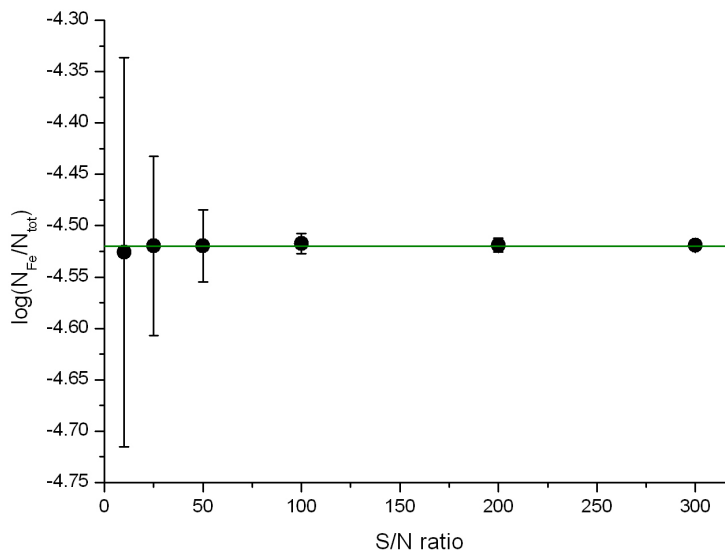


Figure 82: Plot of data from Table 33.

The average S/N ratio of the observations for HD 8801 can be estimated to be above 150 for the region 4000 – 7500 Å which corresponds to an error in abundance for the stronger lines of below 0.01 dex. For the weaker lines, this error will increase. Lines with a central depth of only 0.1 show errors of 0.05 dex at maximum for a S/N ratio of 100.

4.3. Influence of the radial velocity accuracy

In order to analyse the influence of the error made in the radial velocity determination on the abundance determination, the observation was shifted by ± 2 km/s to the red and blue respectively around the correct value of -23.1 km/s. The abundances of the 99 iron line sample were fitted with the *linfit* routine and are shown together with their errors in Table 34 below. There is no change in the abundance within the errors, so that the uncertainty of 1.6 km/s in the radial velocity determination does not influence the results significantly.

v_{rad} [km/s]	$\log(N_{\text{Fe}}/N_{\text{tot}})$	Error (st.dev.)
-21.1	-4.53	0.15
-23.1	-4.52	0.15
-25.1	-4.52	0.15

Table 34: Automatically derived average iron abundances for different values of radial velocity corrections.

4.4. Influence of the projected rotational velocity accuracy

The uncertainty in the determination of the projected rotational velocity can cause an error in the abundance determination as the line fitting algorithm tries to compensate the difference in the line depth by a change in abundance. If $v \sin i$ is assumed smaller than the correct value, the synthesis for a specific spectral line shows a larger central line depth for a given abundance than for the correct (higher) $v \sin i$ value. Therefore, the abundance would be assumed lower in order to fit the line. The opposite effect occurs for an overestimation of the projected rotational velocity.

In order to get an estimate of the influence of this effect on the abundance determination, the average iron abundances based on the 99 line sample were calculated for two models with ± 5 km/s $v \sin i$ around the finally determined value of 53.1 km/s. The result is shown in Figure 83. The abundance error due to the uncertainty of the projected rotational velocity is 0.04 dex for iron and can be assumed the same for all elements.

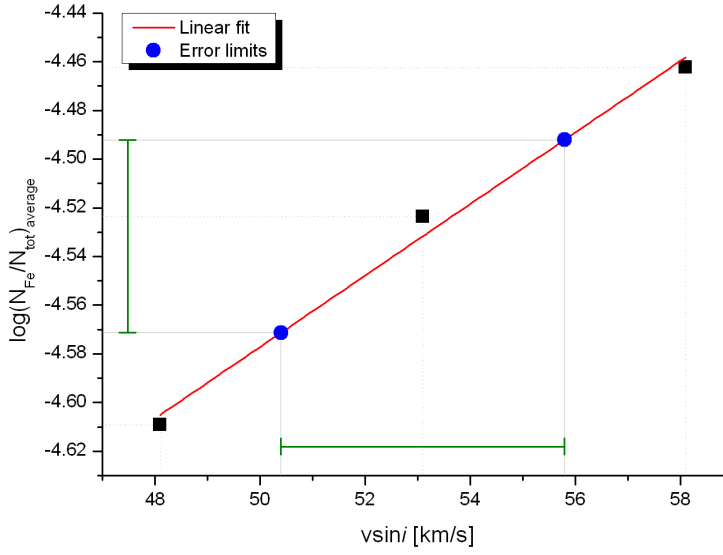


Figure 83: Iron abundances for models with different $v \sin i$. The blue dots mark the error of ± 2.7 km/s, corresponding to an abundance error of 0.04 dex.

4.5. Errors of the fundamental parameters

Due to the many unknown errors in the process of the determination and due to the huge amount of interactions between the parameters, a classical mathematically oriented error analysis is not feasible. Covariances would have to be analysed and the whole Gaussian error calculus would become extremely difficult. This effort is practically useless because of the incomplete knowledge of the errors.

But it is possible to make some educated guesses on the size of the error bars. This is described in the chapters below.

Due to the fact, that all atmospheric parameters are based on a more or less large sample of spectral lines, a standard deviation can be calculated for the determined abundances. This error can be included as instrumental weights $w_i = \frac{1}{\sigma_i^2}$ in the

calculation of the linear fits that were used to determine the three parameters microturbulence, gravity and effective temperature. These fits were calculated by

$$\text{minimizing } \chi^2 = \sum_{i=1}^n \frac{1}{\sigma_i^2} (y_i - \bar{y}_i)^2.$$

When the equation of the applied fit is $y = kx + d$, then the error of the slope is given by

$$\epsilon_k = \frac{s_\epsilon}{\sqrt{s_{xx}}} \text{ with } s_{xx} = \sum_{i=1}^n (x_i - \bar{x})^2 \text{ and } s_\epsilon^2 = \frac{\sum_{i=1}^n (y_i - \bar{y}_i)^2}{n-2}.$$

In a next step, functions were fitted through the upper and lower error limits of each data point and their zeros were calculated. Dividing the span of these zeros along the x-axis by two, gave a reasonable error estimation for the determined parameter. The detailed process is described in the chapters below.

4.5.1. Microturbulence

Iron

The errors of the zeros can be estimated, using a simple geometric approach as shown in Figure 84 below.

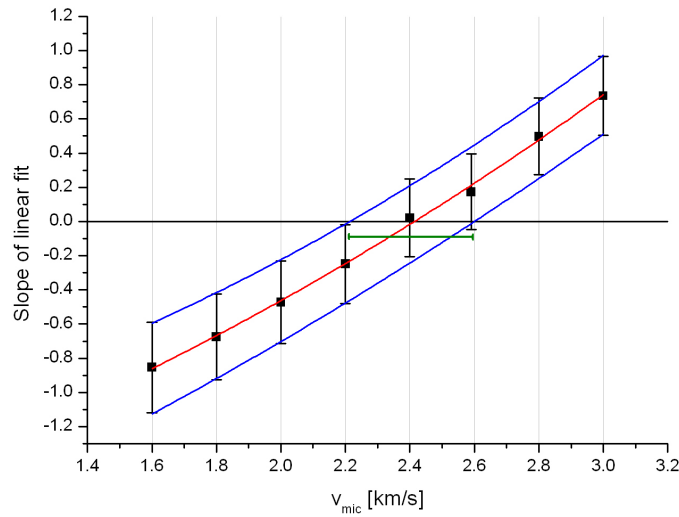


Figure 84: Slopes of linear fits through iron abundance vs. central line depth for models with different microturbulence. The error is marked by the green horizontal bar.

The microturbulence based on iron lines is 2.4 ± 0.2 km/s.

Chromium

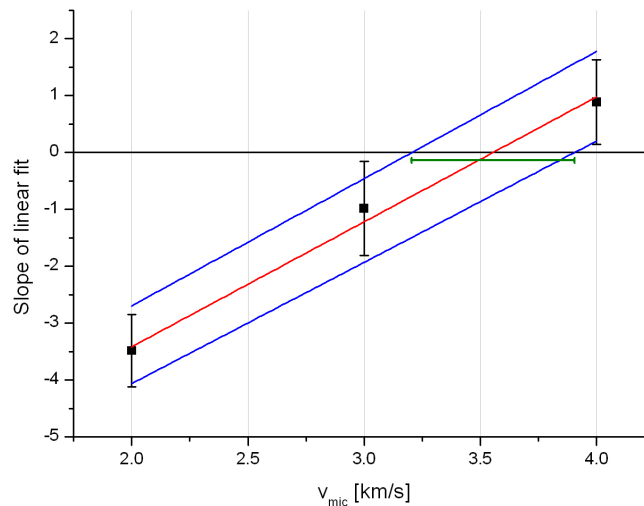


Figure 85: Slopes of linear fits through chromium abundance vs. central line depth for models with different microturbulence. The horizontal bar marks the estimated error.

The microturbulence derived from chromium is 3.6 ± 0.4 km/s (see Figure 85).

Titanium

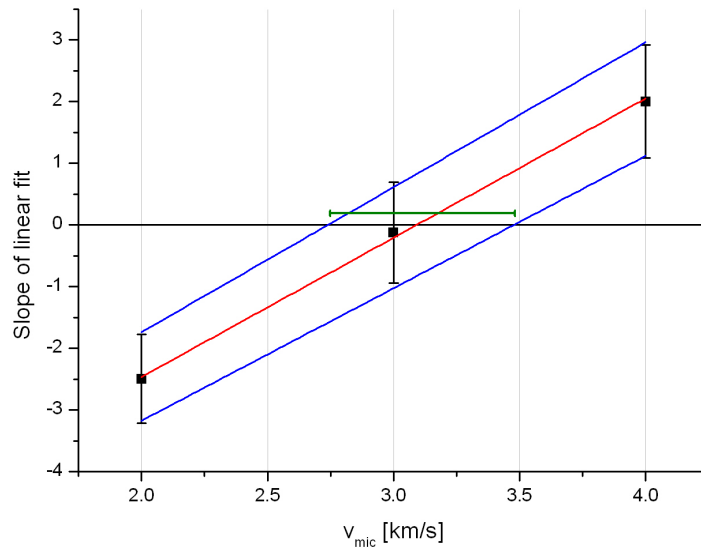


Figure 86: Slopes of linear fits through titanium abundance vs. central line depth for models with different microturbulence. The horizontal bar marks the estimated error.

For titanium a microturbulence velocity of 3.1 ± 0.4 km/s can be calculated (see Figure 86).

Nickel

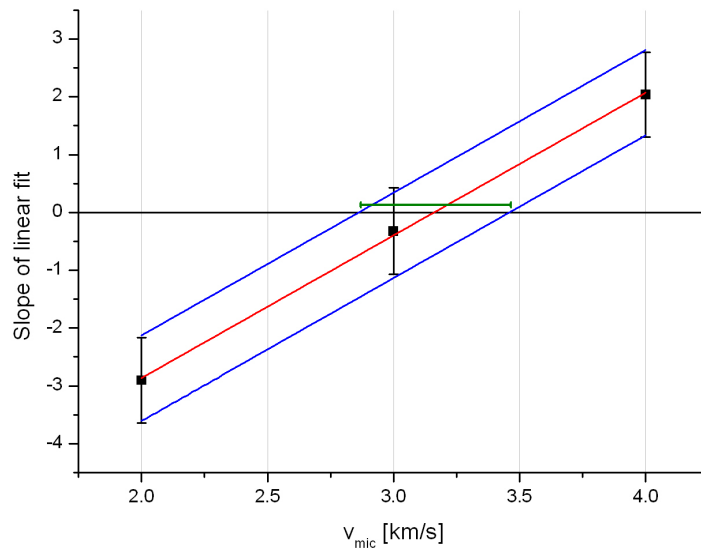


Figure 87: Slopes of linear fits through nickel abundance vs. central line depth for models with different microturbulence. The horizontal bar marks the estimated error.

The microturbulence for nickel is 3.2 ± 0.3 km/s (see Figure 87).

Summary

Collecting all results leads to the following Table 35.

Element	v_{mic} [km/s]	Error v_{mic}	#lines
Fe	2.4	0.2	99
Cr	3.6	0.4	130
Ti	3.1	0.4	78
Ni	3.2	0.3	117
Average	3.1		
Error	0.5		

Table 35: Final results including error estimates for microturbulence.

The error of the combined sample was calculated by using the following formula.

$$s = \sqrt{\frac{1}{N-1} \left\{ \sum_{i=1}^k [(n_i - 1) \sigma_i^2] + \sum_{i=1}^k [n_i (\bar{x}_i - \bar{x})^2] \right\}}$$

Formula 2: Combined error based on multiple samples with individual errors.

Here, N is the total number of lines used, n_i the number of lines for the element i . k is the number of used elements, σ_i the errors estimated in the chapter above, \bar{x}_i the average microturbulence for an element and \bar{x} the overall average for all elements.

4.5.2. Gravity

In the case of gravity, the standard deviations derived from lines from neutral and single ionized stages were used. Because the differences Ion I – Ion II are used, the combined error has to be calculated by $\varepsilon = \sqrt{\sigma_{Ion-I}^2 + \sigma_{Ion-II}^2}$, where σ_{Ion-I} is the standard deviation of the neutral and σ_{Ion-II} the standard deviation of the single ionized line sample.

Iron

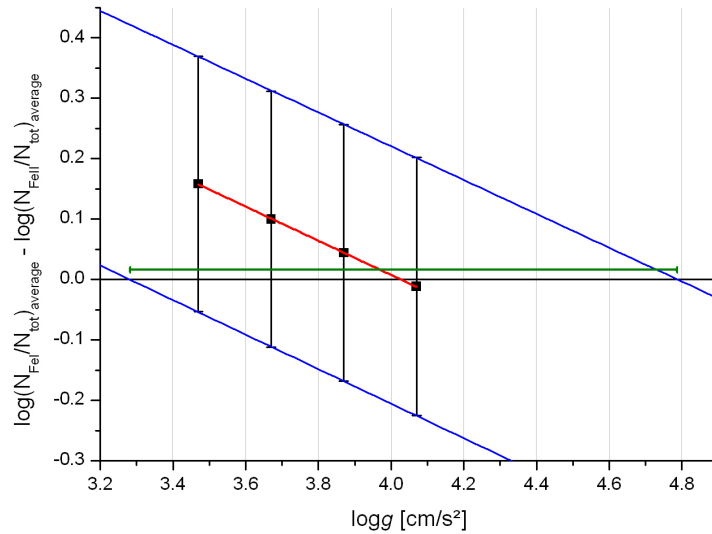


Figure 88: Abundance differences between neutral and single ionized iron. The green horizontal bar marks the estimated error.

The gravity, determined from Fe I and Fe II lines is found to be $4.0 \pm 0.8 \text{ cm/s}^2$ (see Figure 88).

Chromium

For chromium, the error bars for the abundance differences between the two ionization stages are extremely large (0.54 dex, see Figure 89) compared to the differences (max. 0.1 dex) so that using the lower error limits results in an unphysical solution of -1.4 cm/s^2 . The upper limit gives 7.1 cm/s^2 which is also an unphysical solution for this type of stars. Although the error estimation identifies this measurement as completely inconclusive, the result of 4.1 cm/s^2 was used in this analysis.

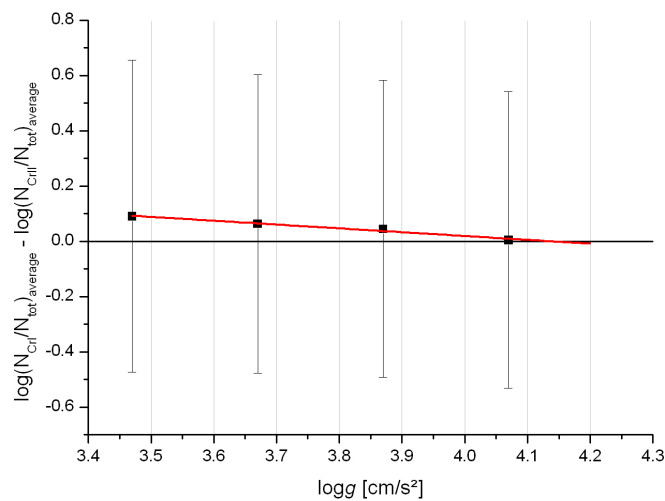


Figure 89: Abundance differences between neutral and single ionized chromium.

Titanium

Titanium gives a value of 4.8 cm/s^2 and was therefore omitted in the final calculation. Nevertheless, the error would be 1.4 cm/s^2 when calculated the same way as for iron and chromium. This mathematically “allows” the other two values to be still correct.

Summary

Due to the unusable error estimation based on chromium, the only remaining error is based on iron with $\pm 0.8 \text{ cm/s}^2$. The standard deviation in the iron line sample is around 0.15 dex which is a typical, and even very good value for an abundance analysis of a faster rotating star. Despite this small error, the gravity could not be determined well in terms of error analysis.

Experience shows, that the typical error in the gravity determination based on ionization equilibration for iron lies around 0.2 cm/s^2 . In this analysis, two elements were used which provide results, only 0.1 cm/s^2 apart. Additionally, both values (4.0 cm/s^2 for iron and 4.1 cm/s^2 for chromium) confirm the photometrically determined value of 4.1 cm/s^2 . This supports the correctness of the finally applied value of 4.1 cm/s^2 for HD 8801.

4.5.3. Temperature

Iron

Figure 90 shows the same graph as Figure 69 but with polynomial fits through the upper and lower errors. Finding the zeros of these fits, calculating the span and dividing it by two results in an error estimation for iron of $\pm 180 \text{ K}$.

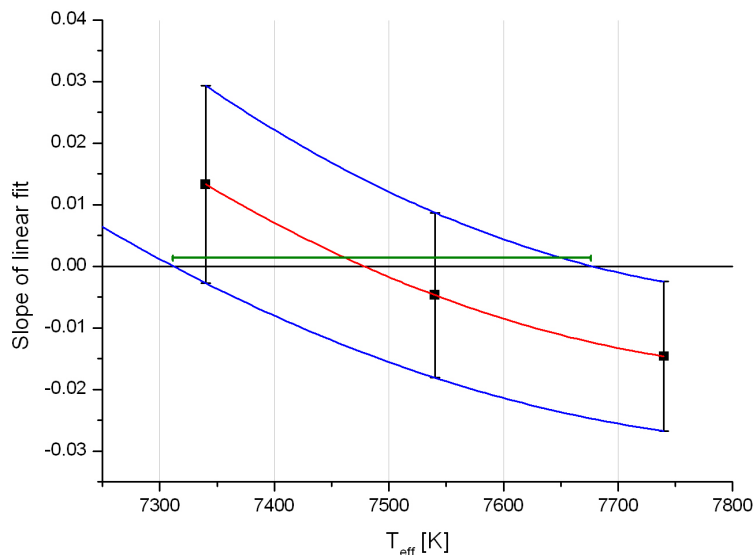


Figure 90: Slopes of average iron abundance vs. excitation potential for models with different effective temperatures including polynomial fits through errors. The green horizontal bar marks the error span.

Titanium

Titanium only allows to use the upper error limit and the error is estimated by the distance between the zeros of the polynomial fits through the averages and the upper error limit (see Figure 91). This gives a value of 230 K.

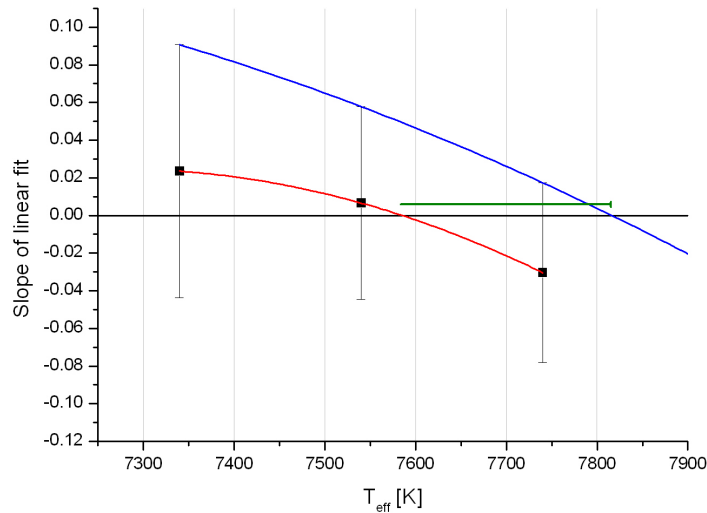


Figure 91: Slopes of average titanium abundance vs. excitation potential for models with different effective temperatures including polynomial fit through upper error limit. The green bar marks the error. The lower limit could not be used.

Nickel

For Nickel, only the lower error limit could be used as the fit through the upper limit doesn't reach zero (see Figure 92). Here the error can be estimated to 110 K.

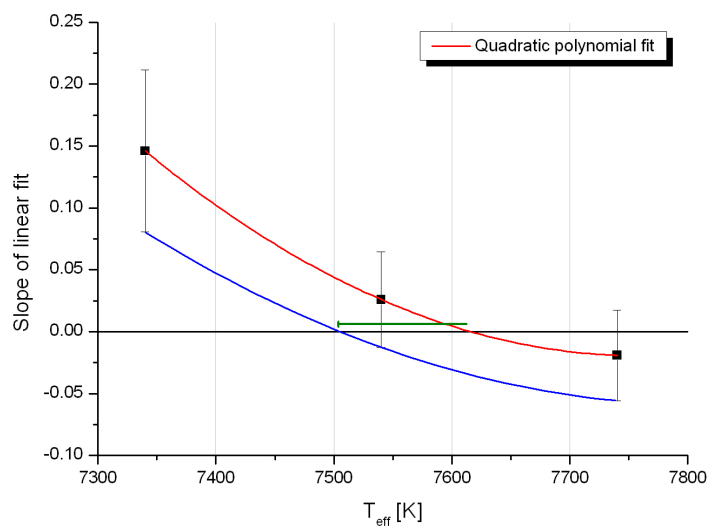


Figure 92: Slopes of average nickel abundance vs. excitation potential for models with different effective temperatures including polynomial fit through lower error limit. The green bar marks the error. The upper limit could not be used.

Summary

The collected results are shown in Table 36. The error is calculated according to Formula 2. As the temperature of 8180 K based on chromium is too high (see chapter 3.4.3), this element was omitted in the error analysis.

Element	T_{eff} [K]	Error T_{eff}	#lines
Fe	7480	180	99
Ti	7590	230	73
Ni	7620	110	111
Average	7560		
Error	180		

Table 36: Final results including error estimates for the effective temperature.

4.6. Error estimations for abundances

As for the error estimations for the atmospheric parameters, an experimental approach was made in order to see the influence of microturbulence, gravity, effective temperature and solar scaled abundance on the derived abundances.

For this purpose, the fundamental parameters were changed around the final solutions and the abundance for iron was calculated.

Applying a linear fit to the plots abundance-versus-parameter and calculating the abundance that corresponds to the final parameter +/- the estimated parameter error gives an error estimation for the element abundances which has to be added to the values given in Table 28 and Table 29. The according plots are shown in Figure 93 to Figure 96. Table 37 shows the results for all parameters. All errors have to be summed up and account for an additional error of 0.09 dex which can be applied to all elements.

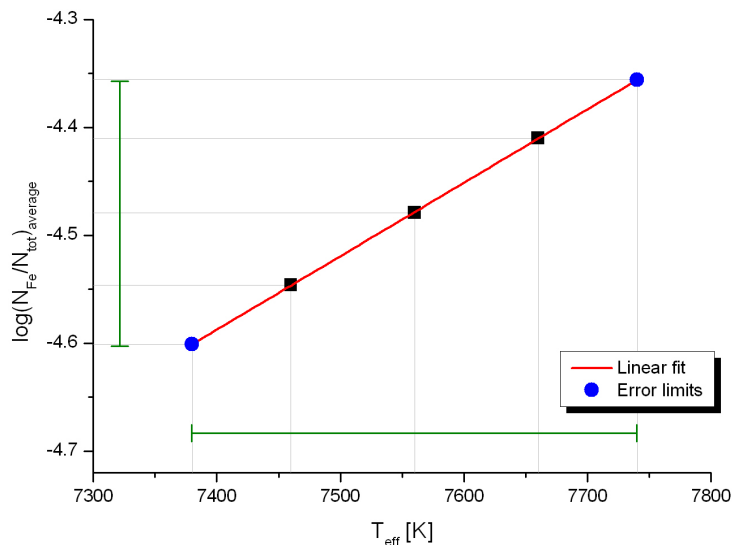


Figure 93: Iron abundances for models with different effective temperatures. The blue dots mark the error limits of ± 180 K which corresponds to an abundance error of 0.07 dex.

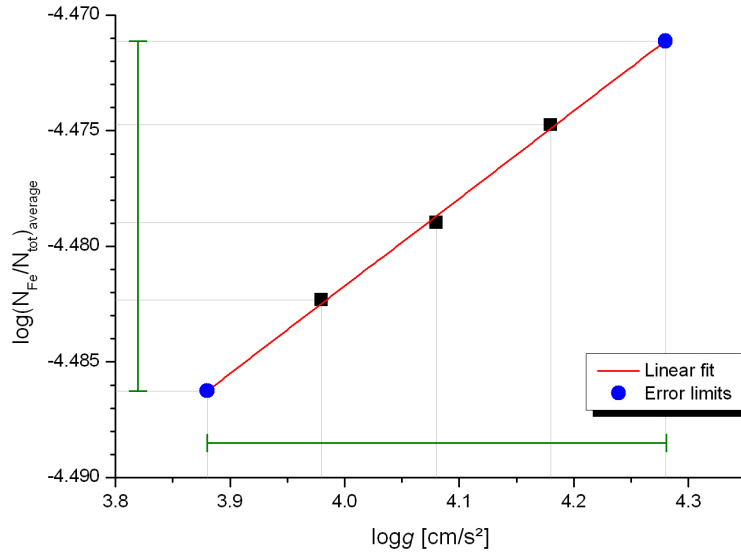


Figure 94: Iron abundances for models with different gravity. The blue dots mark an assumed error of ± 0.2 cm/s² which corresponds to an abundance error of only 0.005 dex.

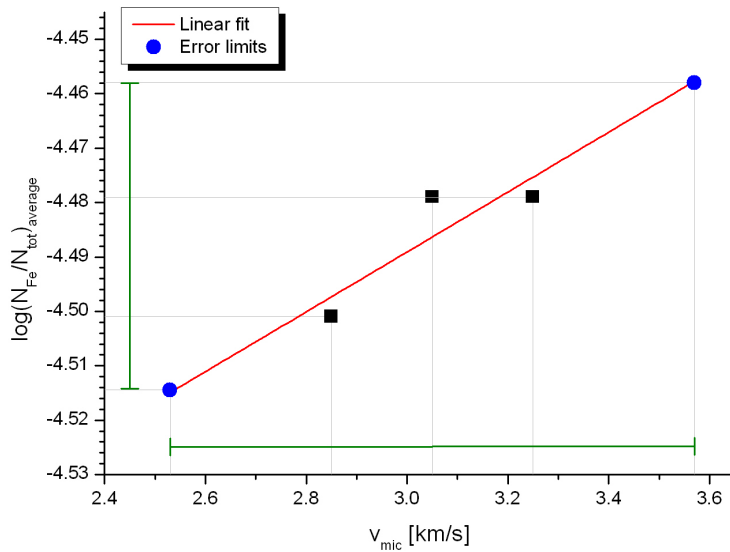


Figure 95: Iron abundances for models with different microturbulence. The blue dots mark the error limits of ± 0.5 km/s which corresponds to an abundance error of 0.01 dex.

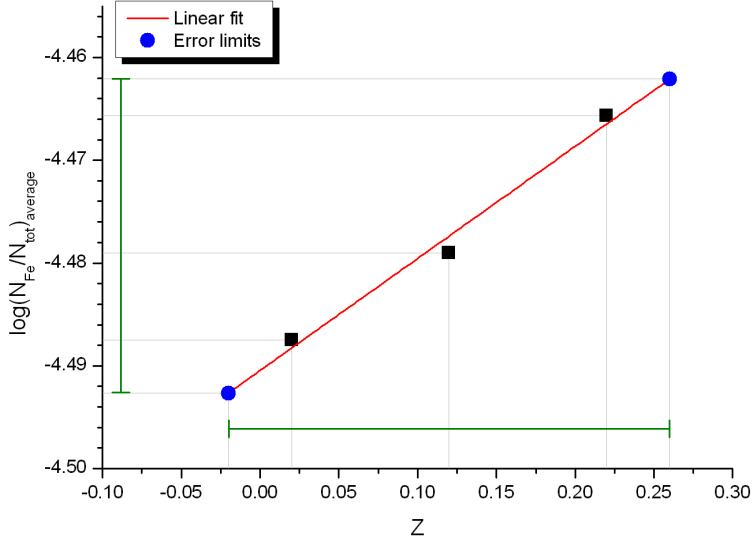


Figure 96: Iron abundances for models with different solar scaled metallicity. The blue dots mark the error in iron abundance of ± 0.15 dex that was used to determine the solar scaled abundance. This error corresponds to an abundance error of 0.005 dex.

Parameter	Value	Error	Fe _{error} [dex]
T _{eff} [K]	7560	180	0.07
logg [cm/s ²]	4.1	0.2	0.005
v _{mic} [km/s]	3.1	0.5	0.01
Z	0.12	0.15	0.005
Sum			0.09

Table 37: Influence of the individual parameter errors on the accuracy of the abundance determination.

4.7. Check of the fundamental parameters

For elements with a larger number of lines, slopes of abundance versus central line depth, abundance versus excitation potential and abundance differences between the ionization stages were calculated in order to check the quality of the microturbulence, effective temperature and gravity determination respectively. Figure 98, Figure 97 and Figure 98 show the corresponding plots.

All plots confirm the correctness of the parameters as the slopes and abundance differences for all elements are close to zero within the errors. As can be seen from the plots below, it is not possible to provide a single value for the atmospheric parameters which are suitable for all elements. This is due to measuring errors and approximations used for the stellar models. Including non-LTE effects, stratification, depth dependent velocity fields, magnetic fields etc. would certainly improve the situation. Therefore, to be on the safe side, well tested models and procedures have been used in this analysis and the results can be used as a basis for further, more sophisticated analyses. It was the main intention of this work, to provide theoreticians a well-founded set of input parameters for further investigations.

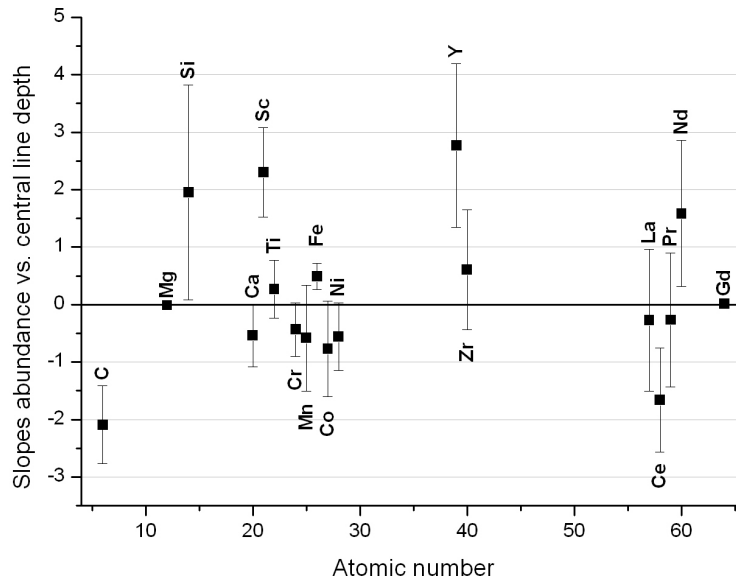


Figure 97: Abundance vs. central line depth slopes for different elements.

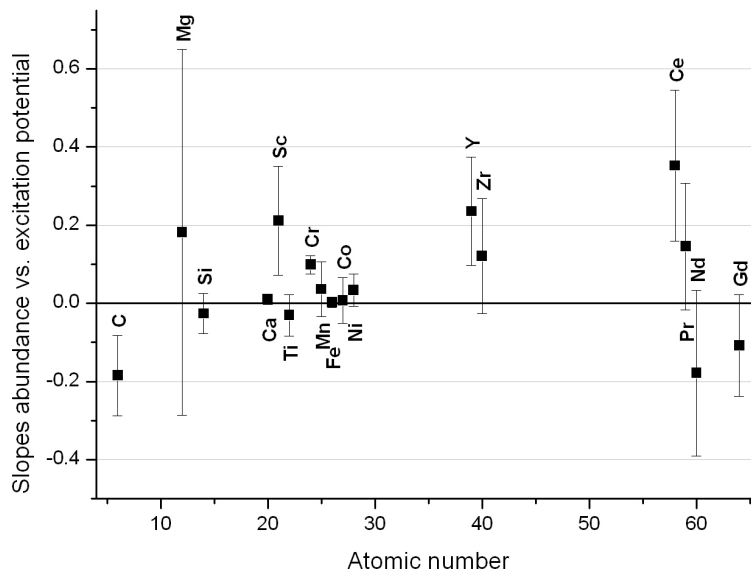


Figure 98: Abundance vs. excitation potential slopes for different elements.

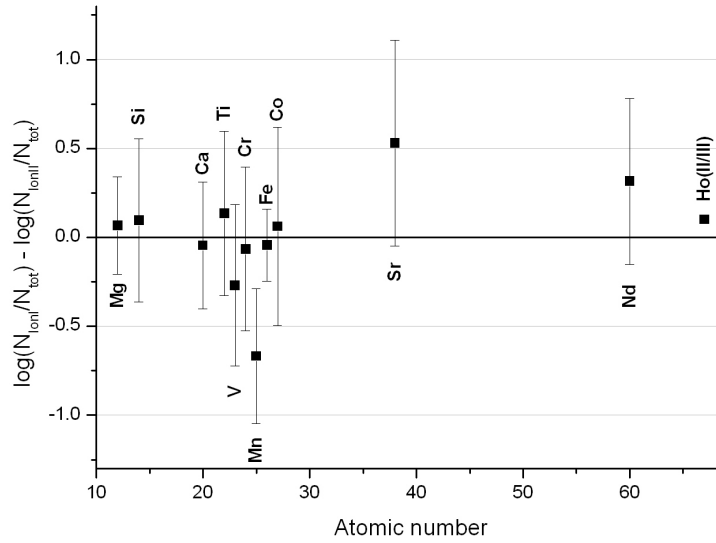


Figure 99: Abundance differences (neutral minus single ionized).

4.7.1. Hydrogen lines

As the spectrum around H β and H α was normalized successfully, the hydrogen lines were also used to check the effective temperature. The initial ODF-models suggested a temperature around 7050 K. The new LL-model with the final abundances and parameters is unable to fit neither of them as shown in Figure 100 and Figure 101 below.

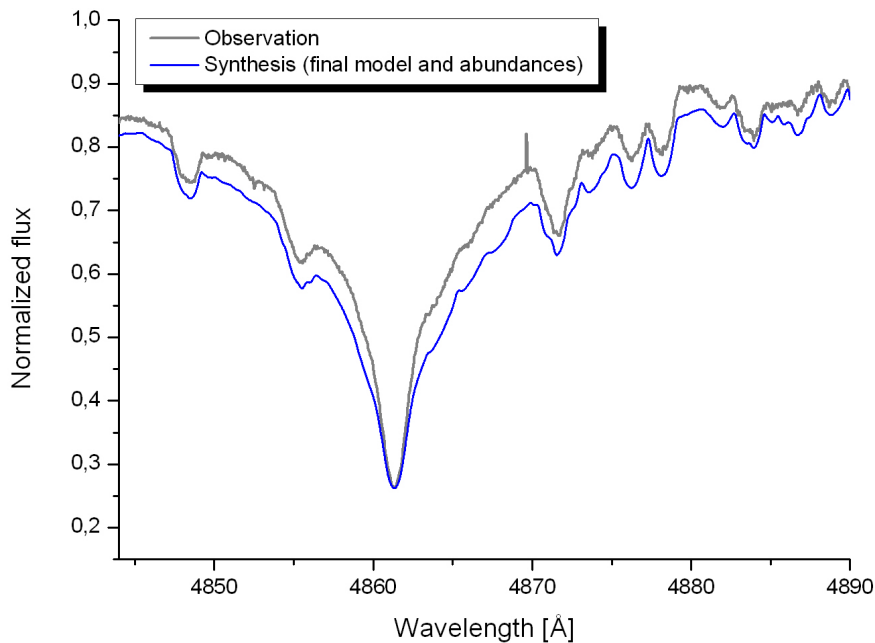


Figure 100: Observation around H β compared to synthesis based on final LL-model.

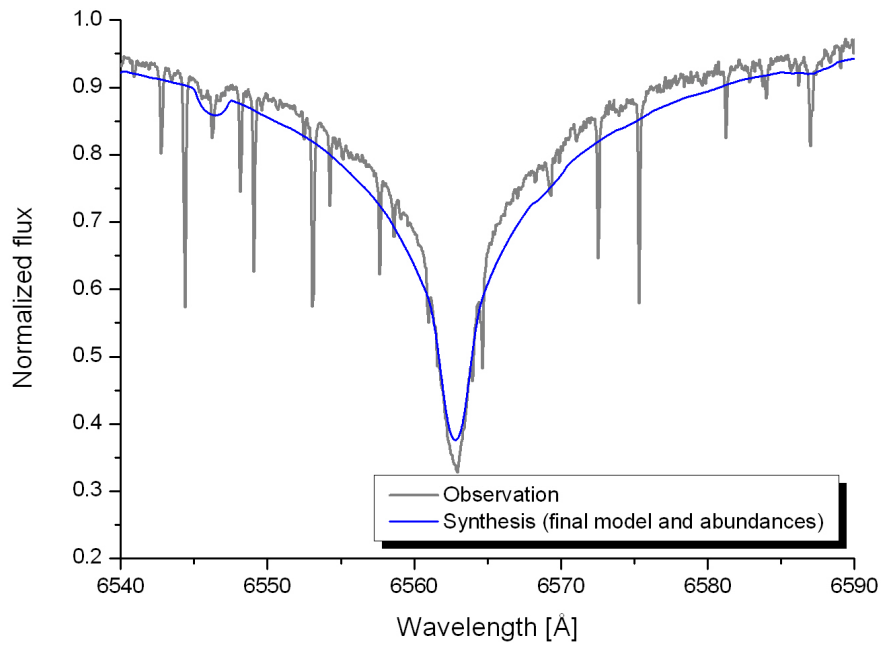


Figure 101: Observation around H α compared to synthesis based on final LL-model.

The observations taken at the OHP also confirm this discrepancy of 500 K which cannot be explained as yet. This is topic for further investigations.

5. Magnetic field

There are different possibilities to check whether a magnetic field is present in the stellar atmosphere or not. As the expected field strength for Am stars lies around 1kG (Böhm-Vitense 2006) and due to the high rotational velocity of HD 8801, the detection of such a weak field is a very complicated task. Three methods were applied and are discussed in the following chapters.

5.1. Line splitting

The shape of spectral lines is usually influenced by the presence of a magnetic field through the Zeeman effect. This effect causes the energy level to split up and a single line in a non magnetic regime would now show up as two (or even more) overlapping lines. The separation between the individual components is proportional to the strength of the magnetic field in the case of a simple doublet. A detailed description and application can be found in Stütz, Ryabchikova, Weiss (2003).

They used the splitting of a Fe II line at 6149.258 Å to determine the magnetic field strength of Ap stars.

Using the spectral synthesis code *synth_mag* written by O. Kochukov which allows to implement a magnetic field, the area around the mentioned iron line was synthesized (see Figure 102).

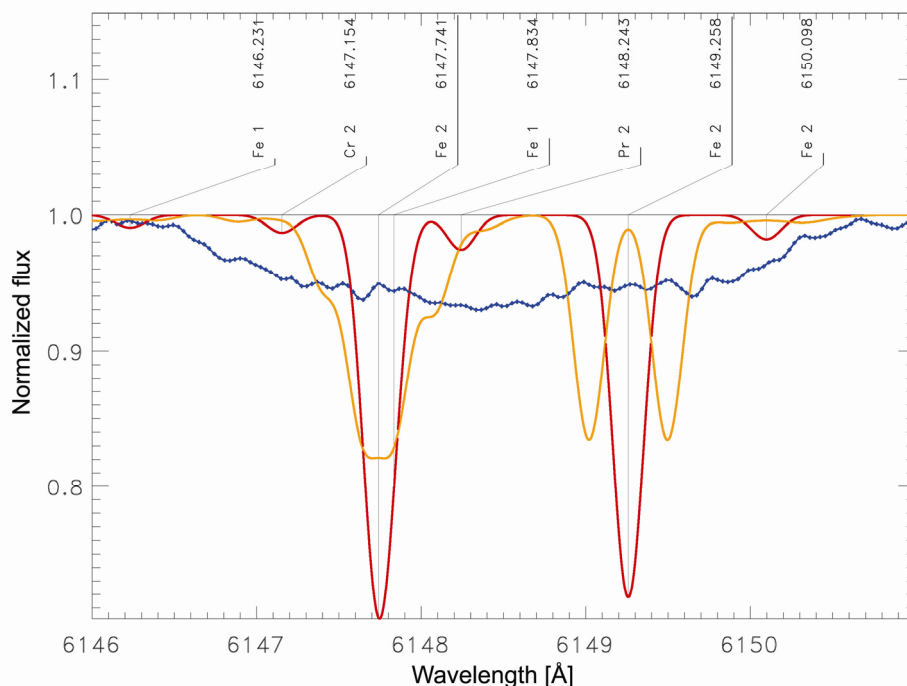


Figure 102: The blue line shows the observation, red the synthesis without magnetic field and orange with a radial magnetic field of 10 kG. The syntheses were calculated without rotational broadening in order to show the effect of the magnetic field.

As can be seen in Figure 102, the rotational broadening of HD 8801 is too strong to see the line splitting.

A convolution with the broadening function for 53.1 km/s results in Figure 103 below. The splitting is transformed to a modification of the whole spectral feature.

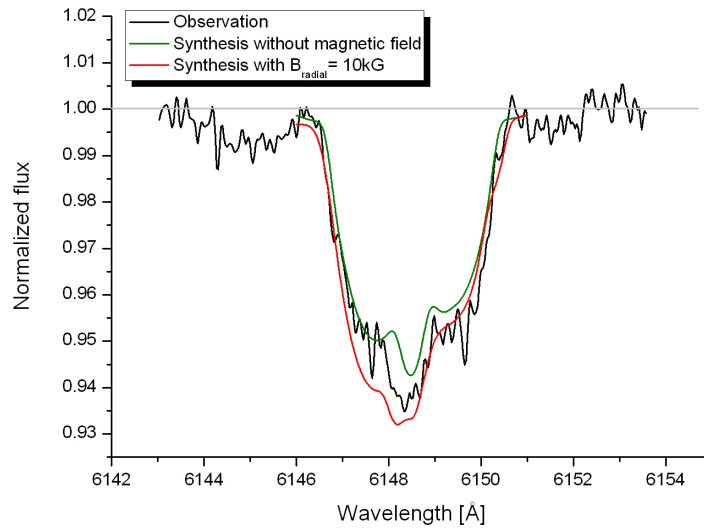


Figure 103: Spectrum around Fe II at 6149.258 Å including syntheses with and without magnetic field.

The result is inconclusive. The presence of a magnetic field allows to fit the red part of the spectral feature better. The blue part suggests no magnetic field.

5.2. Abundance versus Landé factor dependency

Another possibility to detect a magnetic field is to look for the existence of a trend in the diagram abundance versus Landé factor. If a magnetic field is present, lines with a large Landé factor should provide a higher abundance than those, with a small factor. Figure 104 shows a plot for iron. A linear fit was applied, upper and lower 95% confidence levels were calculated. This was checked for several elements and the results are shown in Table 38.

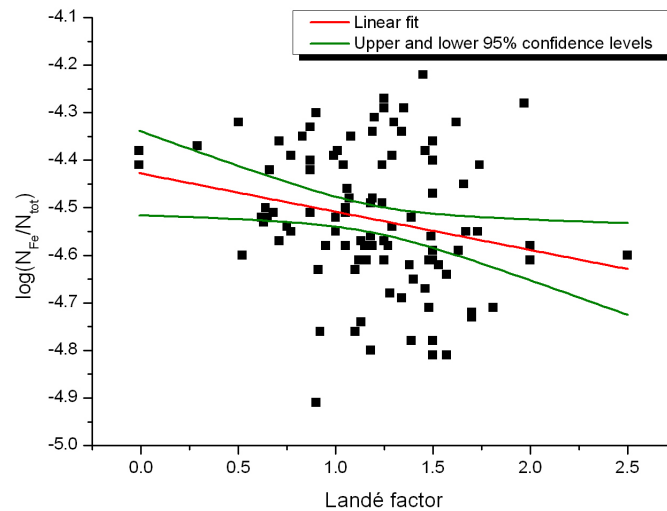


Figure 104: Iron abundances versus Landé factor.

Element	Slope abundance vs. Landé factor	Slope error	R ²
Fe	-0.080	0.035	0.041
Cr	-0.034	0.046	-0.004
Ti	0.196	0.121	0.022
Ni	-0.223	0.124	0.020
Ca	0.191	0.086	0.084
Co	-0.074	0.138	-0.009
Nd	-0.089	0.161	-0.022
Average	-0.016		0.019

Table 38: Slopes of abundances versus Landé factor, errors and adjusted coefficients of determination for different elements.

The low value for R² and the small negative slope (a magnetic field should create a positive slope) indicate that there is no strong magnetic field present.

5.3. Polarimetry

In order to completely rule out a strong magnetic field, polarimetric observations were carried out by M. Gruberbauer at the OHP (observatoire de haute province).

G.A. Wade thankfully reduced and analysed the spectra. He used LSD technique in order to increase the S/N ratio and used a line mask for an 8000 K star. The result is consistent with a null longitudinal magnetic field. Figure 105 shows the LSD profiles for Stokes I and V.

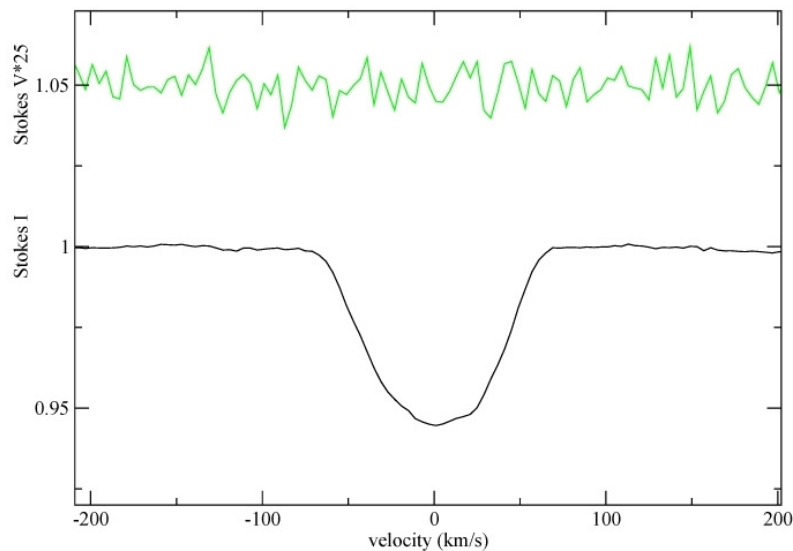


Figure 105: LSD profiles for stokes I and V. The profile for stokes V was multiplied by a factor of 25. No signal is visible and indicates the absence of a strong magnetic field.

5.4. Summary

There is no evidence for a strong magnetic field in HD 8801 although a weak toroidal or partly irregular field which doesn't show up in circular polarization cannot be completely ruled out due to the high rotational velocity.

6. Conclusion

HD 8801 shows an abundance pattern, very similar to Am stars except the higher abundance of scandium. A comparison with other Am stars is shown in Figure 106. The abundances for the 4 other stars were taken from Adelman et al. (1997, 1999) and Bolcal et al. (1992).

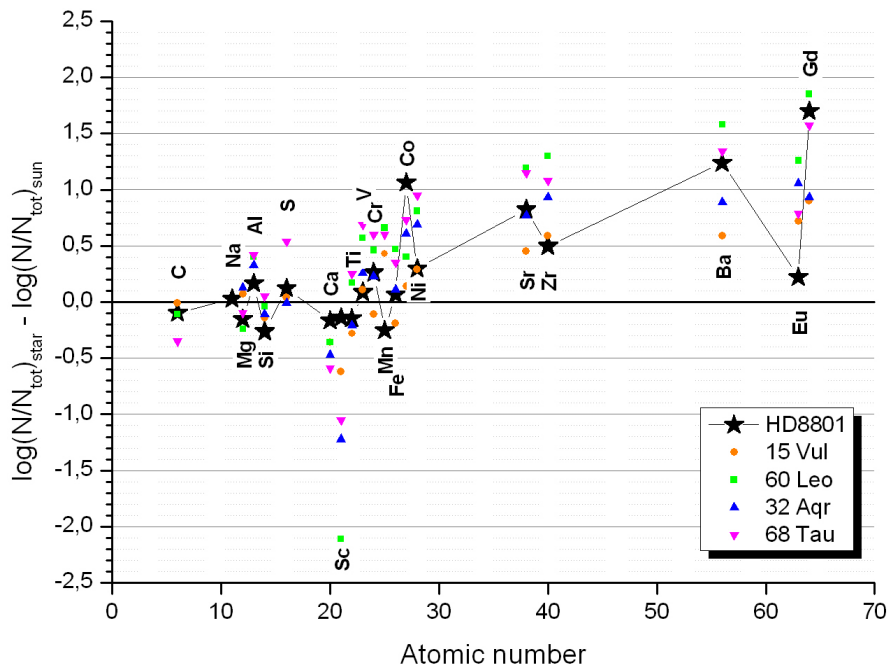


Figure 106: Abundance pattern for different Am stars. The stars denote the abundances derived for HD 8801 in this analysis.

In Figure 107, the element abundances are plotted against their ionization energies for different ionization stages. Around the values of H I, He I and He II, no overabundances are visible, which supports the explanation for the Am star phenomenon given by Böhm-Vitense (2006).

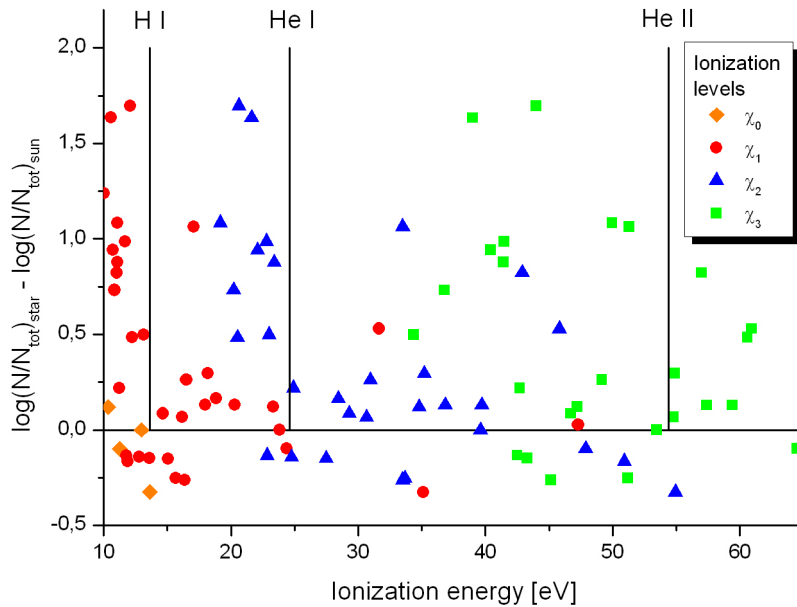


Figure 107: Abundances vs. ionization potentials. The vertical lines mark the ionization energies for H and He.

The discrepancy between the temperature determination from excitation potentials and hydrogen lines of about 500 K is puzzling and will be subject for further investigations. Using only chromium for the determination of the effective temperature based on the abundance-versus-excitation potential dependency, results in an effective temperature even higher (≈ 8200 K). When using titanium to determine the gravity acceleration, a value 0.8 dex higher than for iron and chromium is the result.

These facts show, that the atmospheric structure and the physical processes within the stellar atmosphere, cannot be modelled correctly with our tools as yet. This is not surprising as HD 8801 shows three different peculiarities rolled into one of which the δ Scuti phenomenon is currently the only one, well understood.

This makes HD 8801 a valuable object as it allows to study the influences of the mechanisms among each other. Theoretical models have to be able to explain the wide range of characteristics of this object. The results based on observational data provided in this analysis are the checkpoints for any theory of γ Doradus, δ Scuti and Am stars.

7. References

- Abt, H.A. (1961): ApJS, 6, 37A
Abt, H.A. (1965): ApJS, 11, 429A
Abt, H.A., Bollinger, G., Burke, E.W. Jr. (1983): ApJ, 272, 196A
Adelman, S., Claiskan, H., Kocer, D., Bolcal, C. (1997): MNRAS, 288, 470A
Adelman, S., Claiskan, Cay, T., et al. (1999): MNRAS, 305, 591A
Asplund, M., Grevesse, N., Sauval, A.J. (2005): ASPC, 336, 25A
Baker, N., Kippenhahn, R. (1965): ApJ, 142, 868B
Balona, L.A. (1994): MNRAS, 268, 119B
Bolcal, C., Kocer, D., Adelman, S. (1992): MNRAS, 258, 270B
Böhm-Vitense, E. (1976): IAU Colloq. 32, Physics of Ap Stars, 633
Böhm-Vitense, E. (1980): A&A, 92, 219B
Böhm-Vitense, E. (2006): PASP, 118, 419B
Breger, M., Montgomery, M.H. (2000): ASP Conf. Ser. 210
Breger, M., Stockenhuber, H. (1983): HvaOB, 7, 283B
Breger, M., et al. (1996): DSSN, 10, 24B
Breger, M., et al. (1998): A&A, 331, 271B
Canuto, V.M., Mazzitelli, I. (1991): ApJ, 370, 295C
Castelli, F., Gratton, R.G., Kurucz, R.L. (1997): A&A, 318, 841C
Conti, P.S. (1970): PASP, 82, 781C
Dupret, M.-A., et al. (2004): ESASP, 559, 408D
Eggen, O.J. (1956): PASP, 68, 238E
Fath, E.A. (1935): LicOB, 17, 175F
Fekel, F.C., Warner, P.B., Kaye, A.B. (2003): AJ, 125, 2196
Fresno E.M. (1994), Master Theses, Universidad de Barcelona
Gray, D.F. (1992): Camb. Astrophys. Ser., Vol. 20
Greenstein, J.L. (1949): ApJ, 109, 121G
Guzik, J.A., Kaye, A.B., et al. (2000): ApJ, 542L, 57G
Havnes, O., Conti, P.S. (1971), A&A, 14, 1H
Heiter, U., et al. (2008): J.Phys, Conf.Ser. 130
Henry, G.W., Fekel, F.C. (2005): AJ, 129, 2815
Henry, G.W., Fekel, F.C. (2005): AJ, 129, 2026
Holweger, H. (2001): AIPC, 598, 23H
Kaiser, A. (2006): ASPC, 349, 257K
Kaye, A.B., Handler, G., et al. (1999): PASP, 111, 840K
Koen, C., Kilkeny, D., O'Donoghue, D., Stobie, R.S. (1998): ASPC, 135, 135K
Krisciunas, K., Guinan, E. (1990): IBVS, 3511, 1K
Lane, M.C., Lester, J.B. (1984): ApJ, 281, 723L
Li, Y. (1992): A&A, 257, 133L
Moon, T.T., Dworetzky, M.M. (1985): MNRAS, 217, 305M
Napiwotzki, R., Schoenberger, D., Wenske, V. (1993): A&A, 268, 653N
Nesvacil, N., Stütz, C., Weiss, W.W. (2003): ASPC, 298, 173N
Pamyatnykh, A.A. (2000): ASPC, 203, 443P
Pesnell, W.D. (1987): ApJ, 314, 598P
Poretti, E., Mantegazza, L., et al. (1998): IAUS, 185, 387P
Ribas, I., Jordi, C., Torra, J., Gimenez, A. (1997): A&A, 327, 207R
Shulyak, D., et al. (2004): A&A, 428, 993S
Stix, M. (2004): The sun - an introduction, 2nd ed., A&A lib., Berlin: Springer, 2004
Stütz, C., Ryabchikova, T., Weiss, W.W. (2003): A&A, 402, 729S
Stütz, C. (2005): MSAIS, 8, 165S
-

References

- Titus, J., Morgan, W.W. (1940): ApJ, 92, 256T
Watson, W.D. (1970): ApJ, 162L, 45W
Wilson, R.E. (1953): GCRV, C, 0W
Wolff, S.C. (1983): NASSP, 463

The author wishes to thank G. Handler for providing the observational data, C. Stütz for his support during the analysis, M. Gruberbauer and G. Wade for acquiring and providing the polarimetric observations and W.W. Weiss for his supporting comments.

Zusammenfassung

„Häufigkeitsanalyse des Gamma Doradus – Delta Scuti Hybriden HD 8801“

HD 8801 ist ein bemerkenswertes Untersuchungsobjekt, da es drei physikalisch unabhängige Phänomene in sich vereint. Sowohl der Pulsationsmechanismus der Gamma Doradus Sterne, als auch der Ursprung der Am-Sterne ist noch nicht vollständig verstanden. Die Tatsache, dass diese beiden Phänomene zusammen mit jenem der Delta Scuti Pulsationen, ein und demselben Objekt zugeschrieben werden können, stellt einen für Theoretiker glücklichen und zugleich seltenen Fall dar. Jede Theorie, sowohl für Gamma Doradus, Delta Scuti als auch Am-Sterne, muss die Koexistenz der zugrunde liegenden Prozesse erlauben. Den Schnittpunkt dieser drei Phänomene markiert HD 8801.

Eine detaillierte Analyse dieses Sternes ist somit von großer Bedeutung, als die ermittelten physikalischen Größen sowohl als Eingangsparameter, als auch als Testparameter für sämtliche Theorien dienen können.

Die vorliegende Häufigkeitsanalyse liefert eine Zusammenstellung der meisten, aus Sicht der Spektroskopie, bestimmbaren physikalischen Größen eines Sternes.

Aus fotometrischen Beobachtungen abgeleitete, atmosphärische Parameter dienen als Startpunkt der Untersuchung. Sie wurden im Laufe der Analyse zusammen mit den Elementhäufigkeiten schrittweise bis zur Konvergenz optimiert.

Die Analyse an sich wurde in Form eines iterativen Prozesses, basierend auf Vergleichen mit Modellrechnungen, durchgeführt bei dem von Schritt zu Schritt eine Annäherung an die das Objekt optimal beschreibenden Größen stattgefunden hat.

Aufgrund der hohen Rotationsgeschwindigkeit von HD 8801 konnten keine Äquivalentbreitenmessungen einzelner Spektrallinien durchgeführt werden. Sämtliche Ergebnisse basieren auf Anpassungen synthetischer Linienprofile an beobachtete. Dies stellt aufgrund der zeitaufwendigen Linienprofilvergleiche eine große Herausforderung an den Durchführungsprozess, als auch an die Qualität der Datenreduktion dar. Die Analyse wurde unter Zuhilfenahme von semi-automatischen Routinen durchgeführt, deren Ergebnisse manuell analysiert und während des Iterationsprozesses überwacht wurden. Verschiedene Bestimmungsmethoden wurden angewandt und die Ergebnisse verglichen. Die Einflüsse der Fehler in der Bestimmung der einzelnen Parameter auf die Ergebnisse wurden untersucht.

Die endgültigen Parameter bestätigen die Am-Stern Natur von HD 8801. Das Häufigkeitsprofil zeigt Überhäufigkeiten der seltenen Erden und schwache Unterhäufigkeiten bei, für Am Sterne typischen Elementen wie Sc, Ti und Ca. Bemerkenswert ist die deutliche Abweichung der Werte für die Effektivtemperatur des Sternes, abhängig von der Bestimmungsmethode. Dies ist in diesem Ausmaß ein noch unbekanntes Phänomen und bedarf weiterer Untersuchungen.

Lebenslauf



Richard Neuteufel

Bahnstraße 24/3
2020 Hollabrunn

Geboren am: 15.1.1980
Staatsbürgerschaft: Österreich
Mobil: 0699/19206715
E-Mail: richard.neuteufel@univie.ac.at

Ausbildung

09/1986 – 06/1990	Volksschule, Wien 15
09/1990 – 06/1998	Bundesrealgymnasium, Wien 7
10/2002 – dato	Studium der Astronomie an der Universität Wien
06/2004 – dato	Häufigkeitsanalysen von sonnenähnlichen und Gamma Doradus Sternen
10/2007 – 09/2008	Mitarbeit am Forschungsprojekt „Dynamische Sternatmosphären: Konvektion und Pulsation“

Beruflicher Werdegang

06/2001 – dato	Mitarbeiter bei ABB AG, Abteilung Netzleittechnik Prozessbilderstellung, Softwareentwicklung
----------------	---

Sprachkenntnisse

Englisch in Wort und Schrift

Sonstige Kenntnisse

EDV-Kenntnisse: MS Windows sowie Linux
Programmierkenntnisse: Visual Basic, Java, C#, Fortran